SPECTROTEMPORAL STUDIES OF MAGNETAR BURSTS AND THEIR ORIGIN THROUGH CRUSTAL YIELDING

by
ÖZGE KESKİN

Submitted to the Graduate School of Engineering and Natural Sciences
in partial fulfillment of
the requirements for the degree of Doctor of Philosophy

Sabancı University
June 2025

ABSTRACT

SPECTROTEMPORAL STUDIES OF MAGNETAR BURSTS AND THEIR ORIGIN THROUGH CRUSTAL YIELDING

ÖZGE KESKİN

PHYSICS Ph.D DISSERTATION, JUNE 2025

Dissertation Advisor: Prof. ERSİN GÖĞÜŞ

Dissertation Co-Advisor: Assoc. Prof. YUKI KANEKO

Keywords: High Energy Astrophysics, Neutron Stars, Magnetars, X-ray Bursts

One of the most distinctive features of magnetars − the highly magnetized neutron stars − is their recurring emission of brief yet highly luminous bursts in hard X-rays/soft γ-rays. Once an active episode begins, a few to thousands of such bursts can occur over timescales from days to months. The temporal clustering of these recurrent bursts suggests an underlying mechanism triggering multiple bursts in rapid succession, which is likely crucial for understanding the processes driving magnetar activity. In this thesis, we investigate the "triggering" mechanism of short magnetar bursts by modeling repetitive burst behavior through crustal interactions and employing a cellular automaton model for the magnetar crust. Our simulations, based on physically motivated criteria, successfully reproduce burst clustering. Additionally, the durations and energetics of active episodes in our simulations agree well with observational data. Based on our results, we discuss the potential physical mechanisms underlying burst clusters observed in numerous magnetars, as well as the reactivations of an individual magnetar.

We also investigate how the "triggered" system generates radiation (bursts) and how this radiation evolves within the magnetosphere via time-resolved spectral analysis of 51 bright bursts from the magnetar SGR J1935+2154. Unlike conventional studies in the literature, we follow a two-step approach to probe true spectral evolution. For each burst, we first extract spectral information from overlapping time segments, fit them with three continuum models, and employ a machine-learning-based clustering algorithm to identify time segments that provide the largest spectral variations during each burst. We then extract spectra from those non-overlapping (clustered) time segments and fit them again with the three models: the exponential cutoff power-law model, the sum of two blackbody functions, and the model considering the emission of a modified black body undergoing resonant cyclotron scattering, which is applied systematically at this scale for the first time. Our novel technique allowed us to establish the genuine spectral evolution of magnetar bursts. We discuss the implications of our results and compare their collective behavior with the average burst properties of other magnetars.

ÖZET

MAGNETAR PATLAMALARININ TAYFSAL-ZAMANSAL ÇALIŞMALARI VE KABUK KIRILIMI ARACILIĞIYLA KÖKENLERİ

ÖZGE KESKİN

FİZİK DOKTORA TEZİ, HAZİRAN 2025

Tez Danışmanı: Prof. Dr. ERSİN GÖĞÜŞ
Eş Tez Danışmanı: Doç. Dr. YUKI KANEKO

Anahtar Kelimeler: Magnetarlar, Nötron Yıldızları, Yüksek Enerji Astrofiziği, X-ışını Patlamaları

Yüksek manyetizmaya sahip nötron yıldızları olan magnetarların en belirgin özelliklerinden biri, kısa süreli ancak sert X-ışını/yumuşak γ-ışını enerjilerinde son derece parlak patlamaları tekrar eden şekilde yaymalarıdır. Birkaç günden birkaç aya kadar sürebilen bir aktif evre başladığında, sayıca birkaç adetten binlercesine kadar magnetar patlaması meydana gelebilir. Patlamaların zamansal olarak kümelenmesi, çok sayıda patlamanın kısa bir süre içerisinde tetiklenmesini sağlayan bir mekanizmaya işaret eder, bu nedenle magnetar aktivitesini tetikleyen süreçlerin anlaşılması açısından büyük önem taşımaktadır. Bu tez çalışmasında, magnetar kabuğunu temsil eden bir hücresel otomasyon modeli ile tekrarlayan patlama davranışını kabuk etkileşimleri yoluyla modelleyerek kısa magnetar patlamalarının "tetiklenme" mekanizmasını araştırıyoruz. Fiziksel olarak gerekçelendirilmiş kriterlere dayanan simülasyonlarımız, patlama kümelerini başarıyla yeniden üretmektedir. Ayrıca, simülasyonlarımızdan elde edilen aktif evrelerin süre ve enerji dağılımları gözlemsel verilerle uyuşmaktadır. Bu kapsamda, birçok magnetarda gözlemlenen patlama kümelerinin altında yatan olası fiziksel mekanizmaları ve tek bir magnetarın yineleyen aktifleşme sürecini tartışıyoruz.

Ek olarak, "tetiklenen" sistemin radyasyonu (patlamaları) nasıl ürettiğini ve manyetosfer içinde bu radyasyonun nasıl evrimleştiğini, magnetar SGR J1935+2154'ten gözlemlenen 51 parlak patlamanın zaman çözünürlüklü X-ışını tayf analizleriyle inceliyoruz. Literatürdeki geleneksel çalışmalardan farklı olarak, gerçek tayfsal evrimi ortaya çıkarmak amacıyla iki aşamalı bir yaklaşım izliyoruz. Her bir patlama için, öncelikle örtüşen zaman dilimlerinden tayfsal veri çıkarıyoruz ve bu verilerin üç farklı foton modeli ile uyumlarını sınıyoruz. Buradan elde ettiğimiz sonuçlara, her patlama sırasında en büyük tayfsal değişimleri sağlayan zaman dilimlerini belirlemek amacıyla, makine öğrenmesi tabanlı bir kümeleme algoritması uyguluyoruz. Ardından, bu kümelenmiş ve örtüşmeyen zaman dilimlerinden elde edilen tayfların aynı üç foton modeli ile uyumlarını analiz ediyoruz: yüksek enerjilerde eksponansiyel olarak azalan kuvvet kanunu, iki karacisim ışımasının toplamı ve ilk kez bu ölçekte sistematik olarak uygulanan, rezonant siklotron saçılması geçiren değiştirilmiş karacisim ışımasına dayalı model. Geliştirdiğimiz bu yeni teknik ile, magnetar patlamalarının gerçek tayfsal evrimini ortaya koymayı başardık. Bu kapsamda elde ettiğimiz sonuçların fiziksel çıkarımlarını tartışıyoruz ve bunları diğer magnetarların ortalama patlama özellikleriyle karşılaştırıyoruz.

ACKNOWLEDGEMENTS

I would like to express my sincere gratitude to my advisor, Prof. Ersin Göğüş, for his exceptional guidance, support, and dedication throughout my research. I am also thankful to Dr. Samuel K. Lander for his invaluable mentorship and encouragement.

I would like to extend my appreciation to my esteemed jury members, Prof. Emrah Kalemci, Prof. Tolga Güver, Prof. Ünal Ertan, and Prof. Kazım Yavuz Ekşi, as well as to my co-advisor, Assoc. Prof. Yuki Kaneko, for their time, insights, and contributions to my study.

Most importantly, I am deeply grateful to my family − Metin Keskin, Öznur Keskin, Selin Sude Keskin, Esma Beyza İstek, and Ahmet Erdoğan − for being my greatest supporters. Their unwavering love, care, friendship, and encouragement have been a constant source of strength and joy throughout my journey.

Finally, I acknowledge the support from the Scientific and Technological Research Council of Turkey (TÜBİTAK grant no. 121F266) and the Royal Society (grant no. IES\R3\223220).

To my lovely parents,
with gratitude

TABLE OF CONTENTS

LIST OF TABLES .... **xi**

LIST OF FIGURES .... **xii**

LIST OF ABBREVIATONS .... **xviii**

1. INTRODUCTION **1**
- 1.1. Crustal Magnetic Field Evolution 6
- 1.2. Cellular Automaton Magnetar Simulation 10
- 1.3. What Causes Clustering of Short Magnetar Bursts? 14
- 1.4. Time-integrated and Time-resolved Spectroscopy 16

2. INVESTIGATING THE RECURSIVE SHORT X-RAY BURSTS OF MAGNETARS THROUGH CRUSTAL INTERACTIONS **22**
- 2.1. Model and Simulation 22
- 2.2. Results 24
- 2.3. Discussion 31

3. CONCISE SPECTROTEMPORAL STUDIES OF MAGNETAR SGR J1935+2154 BURSTS **34**
- 3.1. Spectral Data Extraction Process 34
- 3.2. Spectral Analyses & Results 36
  - 3.2.1. Overlapping Time-Resolved Spectroscopy 37
  - 3.2.2. Clustering-Based Time-Resolved Spectroscopy 40
- 3.3. Discussion 45
  - 3.3.1. Spectral Parameters-Flux-Area Correlations 46
  - 3.3.2. Interpretative Elements 51

4. CONCLUDING REMARKS & FUTURE PROSPECTS **53**

BIBLIOGRAPHY **56**

APPENDIX B **65**

APPENDIX A **63**

LIST OF TABLES

2.1. A Sample of Magnetars with Extensive Burst-active Phases 30

3.1. List of 51 SGR J1935+2154 Bursts Included in Our Sample 39
3.2. Number of Nonoverlapping Time Segments per Preferred Photon Model 40
3.3. R^2 vs. kT Fit Parameters (PL Index α and Break Energy) for Various Flux Ranges of BB+BB and MBB-RCS Models as Shown in Figure 3.8 50

LIST OF FIGURES

1.1. Period vs. period derivative diagram of neutron stars. Gray plus signs represent isolated radio pulsars, blue triangles indicate gamma-ray emitting isolated neutron stars, and red squares denote magnetar sources. The dotted lines represent lines of constant characteristic age, while the long dashed lines represent the lines of constant surface magnetic field strength. 2

1.2. Light curves of four example short bursts from the magnetar SGR J0501+4516 recorded by *Fermi*-GBM with 4 ms time resolution in the energy range of 8−200 keV in 2008 August (Lin et al., 2011, used with permission) 3

1.3. Light curve of the burst storm from the magnetar SGR J1550−5418, recorded by *Fermi*-GBM in the 12−293 keV energy range on 2009 January 22. The inset zooms in on the time interval during which an enhanced persistent emission lasting approximately 150 seconds was observed. The dashed line represents the background level. (Kaneko et al., 2010, used with permission) 3

1.4. Basic illustration of the Hall effect (Cumming, Arras, & Zweibel, 2004, used with permission). (a) Standard laboratory configuration where the Hall electric field counteracts the magnetic force acting on electrons in a conductor. (b) When electrical conductivity changes with height, the resulting variation in electron velocity creates a shear in the magnetic field over a characteristic timescale t_{Hall}. 8

1.5. Dominance of plastic flow, Hall effect, and ohmic decay as functions of magnetic field strength and radial distance from the center (Gourgouliatos & Lander, 2021, used with permission). The left edge of the x-axis corresponds to the crust-core boundary, while the right edge marks the neutron drip point. 10

1.6. The magnetar crust as an array of cells (Lander, 2023, used with permission). The magnetic field lines shown on the left are untwisted and embedded in a static cell in its elastic phase, while the lines shown on the right are twisted due to the plastic flow v_{pl} circulating around a cell in its plastic phase. 12

1.7. Light curve of the burst forest from the magnetar SGR 1900+14 recorded by *Swift*-BAT with 1 ms time resolution in the energy range of 15−100 keV on 2006 March 29 (Israel et al., 2008, used with permission) 15

1.8. Spectrum of an example SGR J1550−5418 burst (Lin et al., 2012, used with permission). The top panels present the joint spectral fits using data from both XRT and GBM, while the bottom panels display the spectra extracted from GBM data alone. Spectral fits using the COMPT model are shown in the left column, and those using the BB+BB model are shown in the right column. Residuals corresponding to each fit are displayed in the lower sections of the respective panels. 17

1.9. The distributions of E_{peak} (left-top) and photon index (left-bottom) parameters of the COMPT model, and kT_{Low} (right-top) and kT_{High} (right-bottom) parameters of the BB+BB model for all bursts in the magnetar catalog of Collazzi et al. (2015, used with permission) 18

1.10. Flux-dependent variations between R^2 and kT observed in the spectra of SGR J1550−5418 bursts (Younes et al., 2014, used with permission). [**Left**] Flux color-coded plot of R^2 vs. kT [**Right**] Grouped R^2 and kT data based on flux intervals, from top to bottom as indicated by the legend. Solid lines show the best fits to the data. 19

2.1. The distribution of burst energies obtained by averaging 100 simulations (solid black lines). The red dashed line shows a PL fit to the average distribution. The gray lines display the distributions of individual simulations. 24

2.2. The distribution of Hall (left panel) and plastic (right panel) phase durations. Both trends shown with solid black lines were obtained by averaging the results of 100 iterations. The gray histograms display the distributions of individual simulations. 25

2.3. The distribution of the number of bursts per cell in 1000 yr, obtained as an average of 100 simulations, is shown in black. The gray histograms show the distributions of individual simulations. 26

2.4. The distribution of waiting times between successive bursts from the same cell, considering all crustal cells. The solid dark line is the average of 100 simulations, and the gray lines are the distributions of individual simulations. 27

2.5. Energy of bursts over 1000 yr obtained with the modified cell rule (top panel) and with the original cell rule (bottom panel). Clustering is clearly more pronounced with the modified rule. 28

2.6. [**Left**] The total twist energy of all coronal loops vs. time during the 1000 yr evolution with our modified cellular automaton. [**Right**] Snapshots of stress evolution in units of τ/τ_{el} (colorscale) across the northern hemisphere, just before (top) and after (middle) the emission of a burst cluster with energy 2×10^{42} erg, and at the end of 1000 yr of evolution (bottom), for the same simulation as in the left-hand panel of this figure and the top panel of Figure 2.5. The blue window shown in the top panel represents the highly stressed crustal region that triggered the successive failures. 28

2.7. Plot of the total burst energy vs. duration of each cluster from 100 simulations (gray dots). The black circles show the results of a single simulation (the one shown in the top panel of Figure 2.5). Colored data points represent the same relation for the actual observations of magnetars: SGR $0501+4516$ (green cross), SGR $1550-5418$ (orange square), SGR $1900+14$ (blue diamond), and SGR $1935+2154$ (red stars). 29

3.1. Light curve of an SGR J1935+2154 burst detected at 2021 January 29 10:35:39.918 UTC as seen with the brightest detector (n5). The vertical dashed lines show the Bayesian Block duration start and end times, respectively. The red horizontal lines represent the 22 overlapping time segments, with each subsequent segment having an overlap of 80%. We note that the vertical values corresponding to the red lines are arbitrary, and they have been chosen only for display purposes. . . 35

3.2. Light curve of an SGR J1935+2154 burst detected on 2021 September 10 at 00:45:46.875 UTC as seen with the brightest detector (n8) is shown with gray dotted lines (right axis). Via k-means clustering, 160 overlapping time segments and their corresponding E_{peak} values (the colored data points with asymmetric E_{peak} error bars) yielded 13 spectrally distinctive clusters, each of which is shown with a different color. The black data points show the E_{peak} values with asymmetric error bars that are obtained from the COMPT fit of the data extracted from the time spanned by these 13 clusters in the second stage of spectral analysis. 38
3.3. Blackbody temperature evolution for a burst, throughout which a thermal model is preferred. The light curve is shown with gray dotted lines (right axis; the same event as Figure 3.2). Thick data points show the kT_{Low} and kT_{High} parameters of BB+BB, while thin data points with circles show the kT_{M} of MBB-RCS. The color code represents the preferred model(s) for each time segment based on the ΔBIC. The ΔBIC between BB+BB and the other two models is only slightly above 10 for the first time segment, which is shown with blue color. 41
3.4. (a) The scatter plot of E_{peak} vs. Γ parameters of 279 spectra that can be described well with COMPT. The colors indicate the energy flux values (8−200 keV). (b) The distribution of Γ values with the best-fit model (Linear + Gaussian) curve is shown in red. (c) The distribution of E_{peak} values with the best-fit Gaussian function overlaid in red. . . . 42
3.5. (a) The scatter plot of kT_{Low} vs. kT_{High} parameters of 145 spectra that can be described well with BB+BB. The colors indicate the energy flux values. (b) The distribution of kT_{High} with the best-fit model (two-sided Gaussian) curve is shown in red. (c) The distribution of kT_{Low} values with the best-fit Gaussian function overlaid in red. 43
3.6. The distribution of kT_{M} parameter of 98 spectra that favor MBB-RCS, with the best-fit Gaussian function overlaid in red (left axis). The scatter plot of energy flux vs. kT_{M} is also shown (right axis). The colors indicate the energy flux values. 44

3.7. The scatter plot of E_{peak} vs. flux **(left panel)** and photon index vs. flux **(right panel)** of the COMPT model fits. The color code shows the preferred photon model(s) based on BIC values. The black dots represent the weighted means of consecutive groups, each with 20 data points. The black dashed lines show the BPL fits to the relation between the weighted means of E_{peak} and flux, and between the weighted means of photon index and flux, respectively. The vertical dotted lines in both panels show the flux breaks, which are consistent with each other within their errors. 47

3.8. [**Left**] Flux color-coded plot of R^2 vs. kT for 145 BB+BB spectra. Each data point represents the weighted means of R^2 and kT of three time segments for display purposes only. Solid lines show BPL fits. The dark blue dashed-dotted line indicates PL fit to the lowest-flux group. The lowest-flux group is fitted almost equally well with either a single PL or BPL. The black dashed line indicates $R^2 \propto kT^{-4}$. [**Right**] Flux color-coded scatter plot of R^2 vs. kT for 98 spectra favoring MBB-RCS. Solid lines represent PL fits. The dashed line indicates $R^2 \propto kT^{-4}$. Note that we combined the data points of the two highest-flux groups for MBB-RCS, since only three spectra in the highest-flux group ($F > 10^{-4.5}$ erg cm^{-2} s^{-1}) favor the MBB-RCS model; these three are shown with red diamonds. 49

A.1. The burst energies over a 1000 yr obtained with [**Top**] random initial stress values between $0.7\tau_{el}$ and $1.1\tau_{el}$. [**Middle**] random initial stress values between $0.5\tau_{el}$ and $1.1\tau_{el}$. [**Bottom**] another cell rule (see text for details). 64

A.2. The total burst energy vs. duration of each burst cluster from 100 simulations through 1000 yr evolution (gray dots). The black circles show the results of a single simulation (the ones shown in Figure A.1). Colored data points represent the same relation for the actual observations of magnetars. [**Left**] Initial stress level: $0.7\tau_{el}$ - $1.1\tau_{el}$. [**Middle**] Initial stress level: $0.5\tau_{el}$ - $1.1\tau_{el}$. [**Right**] Another cell rule (see text for details). 64

B.1. Observed count spectrum of a time segment from the burst detected at 488642074.718 (*Fermi* MET), represented by black crosses. The three solid lines are the best-fitting model curves: MBB-RCS in red, COMPT in blue, and BB+BB in green, all of which fit the spectrum equally well. 69

B.2. [**Left**] Blackbody temperature evolution of the burst detected at 652927551.870 (*Fermi* MET; same event as Figures 3.2 and 3.3); this is the same plot as Figure 3.3 but zoomed in on the first 0.6 s. The first seven time segments are numbered on top, and thick crosses show the kT_{Low} and kT_{High} parameters of BB+BB, while thin data points with circles show kT_{M} of MBB-RCS. The color code represents the preferred model(s). [**Right**] The photon flux distribution for each time segment is shown. The color code represents the time segments. For the first time segment, the photon flux distributions shown with the yellow dashed line and yellow solid line were obtained with COMPT ($E_{\text{peak}} = 37.85\,\text{keV}$ and $\Gamma = 0.54$) and MBB-RCS, respectively. For the rest of the time segments, photon flux was obtained with BB+BB. 70

LIST OF ABBREVIATONS

Γ	Photon Index of COMPT Model	18
τ_{el}	Elastic Yield Stress of the Crust	9
Fermi	*Fermi* Gamma-ray Space Telescope	16
Swift	*Neil Gehrels Swift* Observatory	17
E_{peak}	The Average Peak Energy in the νF_{ν} Spectra of COMPT Model	18
kT_{High}	High Blackbody Temperature of BB+BB Model	19
kT_{Low}	Low Blackbody Temperature of BB+BB Model	19
kT_{M}	Blackbody Temperature of MBB-RCS Model	44
AXP	Anomalous X-ray Pulsar	2
BAT	Burst Alert Telescope	19
BB	Blackbody	43
BB+BB	Sum of Two Blackbodies	16
BGO	Bismuth Germanate	34
BIC	Bayesian Information Criterion	36
BPL	Broken Power Law	46
C-stat	Castor Statistics	36
COMPT	Power Law with a High-Energy Exponential Cutoff	16
CTTE	Continuous Time-Tagged Event	34
DRM	Detector Response Matrices	36
FRB	Fast Radio Burst	21

GBM	Gamma-ray Burst Monitor	17
LAT	Large Area Telescope	34
MBB-RCS	Modified Black Body Spectrum that undergoes Resonant Cyclotron Scattering	20
NaI	Sodium Iodide	34
PL	Power Law	46
RP	Radio Pulsar	1
SGR	Soft Gamma Repeater	1
XRT	X-ray Telescope	17

1. INTRODUCTION

Stars with masses around eight times or more than that of the Sun undergo core collapse during their final evolutionary stages, forming extremely compact remnants at their centers while ejecting material from their outer layers into the surrounding space in the form of supernova explosions (S. Woosley & Janka, 2005). The remnant structure at the core may become either a neutron star (T. A. Thompson, Chang, & Quataert, 2004), which is supported by neutron degeneracy pressure, or a black hole (MacFadyen, Woosley, & Heger, 2001; S. E. Woosley, 1993), in which matter is compressed to such an extent that even light cannot escape its gravitational field. If the central compact object remains as a neutron star, it provides a unique environment in which the behavior of the radiating matter can be investigated under extreme density and the influence of the intense magnetic fields.

The vast majority of neutron stars manifest as isolated radio pulsars (RPs), which emit radiation powered by their rotational energy and exhibit pulses at radio wavelengths through synchrotron emission of electron-positron plasma (Chen & Ruderman, 1993). As they lose rotational energy, these isolated neutron stars gradually slow down. This deceleration continues until the voltage generated by the rotating dipolar magnetic field falls below the critical threshold required to produce electron-positron pairs; at this point, the radio pulsations cease. Figure 1.1 presents the spin periods (P) and their rate of change (period derivative; $\dot{P}$) for neutron stars [1]. In this figure, RPs form the densely populated group indicated by gray plus signs.

A small subset stands out among the isolated neutron stars that slow down by emitting radiation as described above. These systems, indicated by red squares in Figure 1.1, possess high periods and high period derivatives, and emit X-rays with energies far exceeding their rotational energy. It can also be inferred that they possess extremely strong surface magnetic field strengths from the relation of $B \propto \sqrt{P\dot{P}}$. These sources, known as Soft Gamma Repeaters (SGRs) and Anomalous

---

[1] The data is taken from the ATFN Pulsar Catalog (`https://heasarc.gsfc.nasa.gov/w3browse/all/atnfpulsar.html`) (Manchester, Hobbs, Teoh, & Hobbs, 2005) and the McGill Magnetar Catalog (`https://www.physics.mcgill.ca/~pulsar/magnetar/main.html`) (Olausen & Kaspi, 2014).

X-ray Pulsars (AXPs), form what are referred to as magnetars – young ($\sim 10^3$ yr) neutron stars that radiate energy due to their intense magnetic fields (Kaspi & Beloborodov, 2017). The inferred surface magnetic fields of these systems are of the order of $10^{14} - 10^{15}$ Gauss (Duncan & Thompson, 1992; Kouveliotou et al., 1998, 1999). Their extremely strong magnetic fields are thought to play a pivotal role in their emission of highly luminous transient events in hard X-rays/soft γ-rays, such as short bursts, outbursts, burst storms/forests, and intermediate and giant flares, as well as their persistent emission.

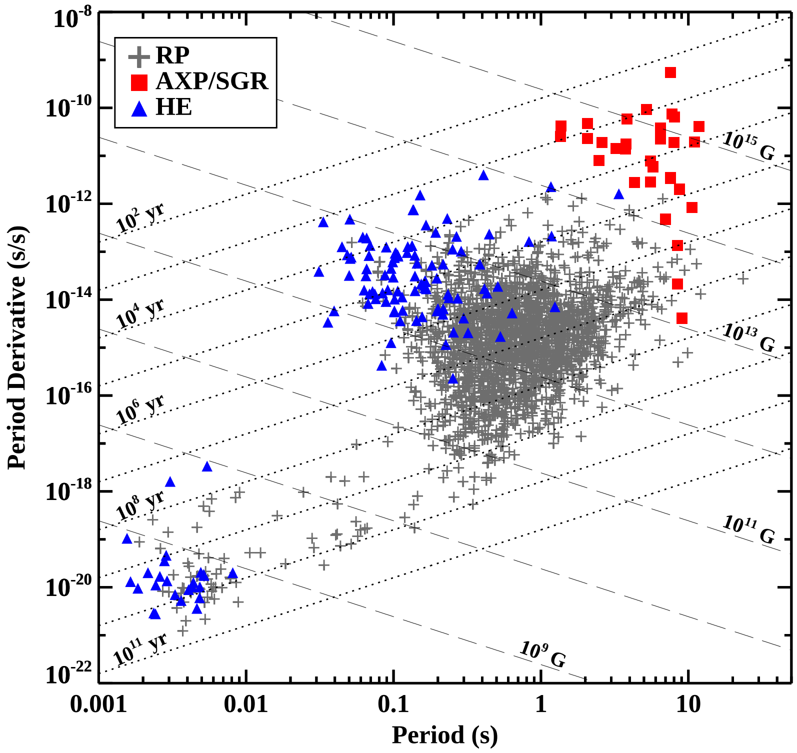

Figure 1.1 Period vs. period derivative diagram of neutron stars. Gray plus signs represent isolated radio pulsars, blue triangles indicate gamma-ray emitting isolated neutron stars, and red squares denote magnetar sources. The dotted lines represent lines of constant characteristic age, while the long dashed lines represent the lines of constant surface magnetic field strength.

The most frequently observed high-energy events are short bursts (see Figure 1.2 for example light curves), with durations ranging from a few milliseconds to a few seconds, peaking at ~ 0.1 s; their energies approach 10^{41} erg (Göğüş et al., 2001). The rarely observed giant flares cover the other end of the magnetar burst properties, with much harder spectra and longer durations. These are the most energetic events, releasing over 10^{44} erg in several minutes (Hurley et al., 1999; Palmer et al., 2005). Apart from their longer durations, they also exhibit a unique morphology: a spectrally hard initial short spike, followed by a longer tail that oscillates at the spin frequency of the parent neutron star.

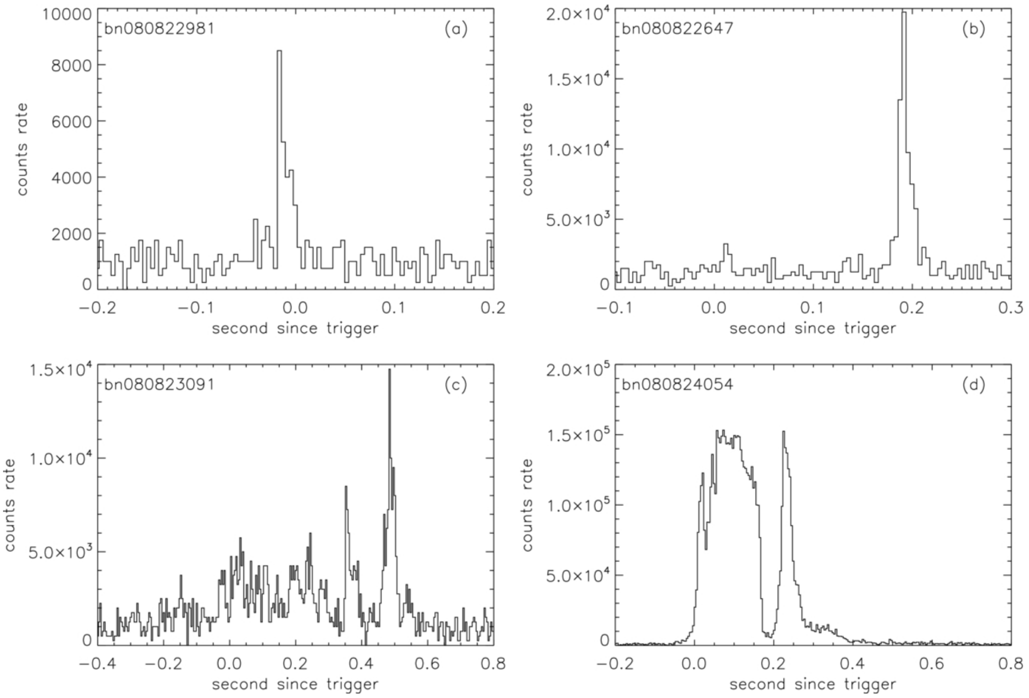

Figure 1.2 Light curves of four example short bursts from the magnetar SGR J0501+4516 recorded by *Fermi*-GBM with 4 ms time resolution in the energy range of 8−200 keV in 2008 August (Lin et al., 2011, used with permission)

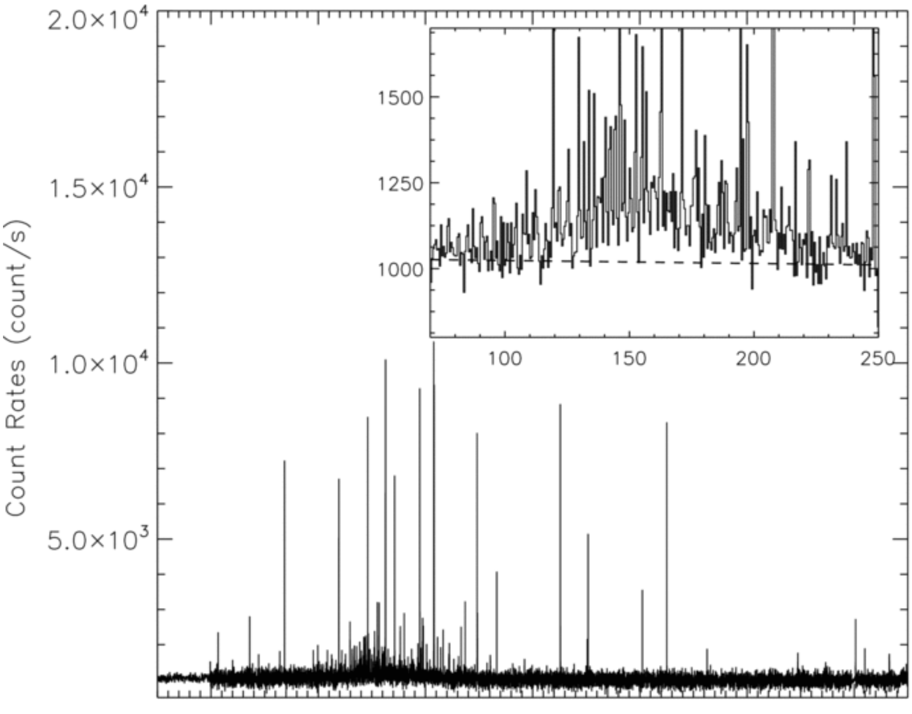

Figure 1.3 Light curve of the burst storm from the magnetar SGR J1550−5418, recorded by *Fermi*-GBM in the 12−293 keV energy range on 2009 January 22. The inset zooms in on the time interval during which an enhanced persistent emission lasting approximately 150 seconds was observed. The dashed line represents the background level. (Kaneko et al., 2010, used with permission)

Being between these two types of high-energy transients in terms of duration and energy, intermediate flares last from a few seconds to tens of seconds, with energies extending up to $\sim 10^{42}$ erg (Ibrahim et al., 2001; Kouveliotou et al., 2001). Additionally, magnetars such as SGR 1900+14 (Israel et al., 2008), SGR 1550-5418 (Kaneko et al., 2010; van der Horst et al., 2012), and SGR 1935+2154 (Kaneko et al., 2021) have shown intense high-energy burst storms/forests (see Figure 1.3 as an example). In some magnetars, the emission of energetic burst(s) accompanies the onset of "magnetar outbursts," which are long-lasting (weeks to many months) enhancements in persistent X-ray emission (Coti Zelati, Rea, Pons, Campana, & Esposito, 2018).

Typical high-energy magnetar events are generally considered to be associated with local or global yielding of the solid neutron star crust through the release of the built-up elastic stress in the crust due to the internal magnetic field evolution (C. Thompson & Duncan, 1995, 2001). In this model, intense magnetic fields induce extreme elastic stress accumulation in the solid neutron star crust. The crust can maintain its structural integrity under the accumulated stress up to a certain threshold. When this critical limit is exceeded, the crust fractures, leading to an event known as a starquake. The resulting crustal failure leads to a sudden displacement of the footpoints of the external magnetic field lines, which injects magnetohydrodynamic (Alfven) waves into the magnetosphere (see Fig. 1(a) of C. Thompson and Duncan 1995). This facilitates the transfer of energy to a fireball made from the plasma of trapped $e^{-}-e^{+}$ pairs and photons within the closed magnetic field lines (see Fig. 1(b) of C. Thompson and Duncan 1995). Cooling of such plasma provides a potential mechanism for magnetar bursts. The statistical properties of magnetar bursts showing similarities to those of earthquakes on Earth lend further support to the starquake model (Cheng, Epstein, Guyer, & Young, 1996; Göğüş et al., 1999; Göğüş et al., 2000).

Another possible mechanism to generate magnetar bursts is the magnetic reconnection, i.e., rapid untwisting of the twisted external magnetic field lines (see Figure 1.6 for examples of twisted and untwisted magnetic field lines). The reconnection model, originally proposed to explain the flaring activities of the Sun, was adapted by Lyutikov (2003) to account for magnetar bursts. According to this model, oppositely oriented magnetic flux tubes break apart as they approach each other and subsequently reconnect, forming a new flux tube with a lower energy state. The difference in energy between the pre-break and post-reconnection states is released as radiation (bursts).

Considering the broad variety of magnetar activities, it is possible that different types of events may have distinct physical origins. These make understanding the underlying physics challenging and hinder the construction of a unified physical model to explain the diverse range of activities. Motivated by this issue, Lander (2023) recently presented a cellular automaton model that aims to explain the wide range of energies released in various magnetar activities through the yielding of the star's crust. In this model, the buildup and release of elastic stress from the crust leads to the braiding of coronal loops, which ultimately induce reconnection events and produce the energy releases we observe. While the local nature of coronal loops allows for the possibility of high-energy short bursts, the model also includes a criterion that causes more widespread yielding – leading to giant flares – and quiescent periods, which are typically decades long.

Our understanding of magnetar activities is still fragmented and incomplete; both the "triggering" mechanism of a magnetar event and how the triggered system generates outgoing and evolving radiation within the magnetosphere are unclear. In this thesis, we aim to better understand the underlying physical mechanisms responsible for the emission of high-energy short magnetar bursts from two aspects:

- The first part of this thesis focuses on the "triggering" mechanism of short magnetar bursts (Chapter 2). One notable feature of these bursts is that they often do not come in isolation: In many cases, we observe clusters of bursts, often separated in time by a second or less (see e.g., Lin, Göğüș, et al., 2020; van der Horst et al., 2012). These burst clusters may be a key to understanding the underlying processes driving magnetar activity, since such temporal concentrations of bursts are highly unlikely to be coincidental, but rather indicate a mechanism that causes the triggering of several bursts in quick succession. Here, we investigate the recursive short X-ray burst behavior of magnetars through crustal interactions by utilizing the magnetar simulation of Lander (2023) and discuss the possible underlying physical scenarios responsible for magnetar burst clusters as seen in many magnetar observations.
- The second part of this thesis focuses on how the "triggered" system generates outgoing and evolving radiation (bursts) within the magnetosphere, explored via time-resolved spectral investigations of magnetar SGR J1935+2154 bursts (Chapter 3). Hard X-ray spectral analyses of magnetar bursts are also crucial steps toward a better understanding of the physical mechanisms responsible for these intriguing phenomena. Studies so far have shown that magnetar bursts can be modeled almost equally well with a thermal model as with the sum of two blackbodies, or a nonthermal model, such as a power law with a high-energy exponential cutoff (Lin et al., 2012; van der Horst et al., 2012).

This poses a puzzle in the understanding of the underlying mechanism of the observed bursts, as follows. According to the crustal fracturing scenario (C. Thompson & Duncan, 1995), a fireball made from the plasma of trapped $e^{-}-e^{+}$ pairs and photons forms in the closed magnetic field lines via Alfven waves released from the crust following the cracking. Therefore, thermal radiation could be expected from such regions in quasi-equilibrium. On the other hand, the observed magnetar synchrotron-like nonthermal radiation spectra might be an indication of particle interactions via magnetic reconnection. Recently, Yamasaki, Lyubarsky, Granot, and Göğüş (2020) studied the spectral modification of extremely energetic magnetar flares by resonant cyclotron scattering, and they showed that the scattering process may alter the emerging radiation from these events. In this model, photons emitted via a mechanism that depends only on the temperature of the fireball near the neutron star surface interact with magnetospheric particles, which results in significant changes in the emission spectrum.

- Finally, we close with concluding remarks and expand future prospects in Chapter 4.

Let us first summarize the relevant studies that have been done so far and introduce the problems and missing points in the literature. In Section 1.1, we summarize crustal magnetic field evolution; in Section 1.2, we provide a brief summary of the relevant details of the cellular automaton model; and in Section 1.3, we provide a physical picture of magnetar burst clusters. Finally, in Section 1.4, we summarize the findings of comprehensive time-integrated and time-resolved spectral studies in the literature, explain the problem in the conventional method of time-resolved analysis, and introduce our novel two-step approach to probe the true spectral evolution of the short magnetar bursts.

1.1 Crustal Magnetic Field Evolution

Much work modeling magnetars has focused on the evolution of the magnetic field within the star's crust. In particular, by assuming the crust is rigid – so that ions are static, and the electrons are the only mobile charged particle – electron magnetohydrodynamics (MHD) may be derived. The crustal magnetic field (**B**) then evolves according to the equation (Goldreich & Reisenegger, 1992)

$$\frac{\partial \mathbf{B}}{\partial t} = -\frac{1}{4\pi}\nabla \times \left(\frac{c}{\rho_e}(\nabla \times \mathbf{B}) \times \mathbf{B} - \frac{c^2}{\sigma}\nabla \times \mathbf{B}\right) \tag{1.1}$$

where c is the speed of light, ρ_e is the charge density and σ is the electrical conductivity. Equation (1.1) represents an interplay between Hall drift (the first term on the right), causing the field to evolve toward more intense high-multipole structures, and ohmic decay (the second term on the right), which dissipates magnetic flux.

The Hall drift refers to the advection of magnetic field lines within the solid crust by free electrons (Cumming et al., 2004). Let us first define a very basic system to observe the Hall effect: A current-carrying conductor is placed in an external magnetic field perpendicular to the current (see panel (a) of Figure 1.4). In this configuration, the conducting electrons, whose velocity is $\mathbf{v}_e = -\mathbf{J}/\rho_e$, are deflected laterally due to the Lorentz force from the magnetic field. This deflection induces a transverse electric field, known as the Hall electric field, given by $\mathbf{E}_H = \mathbf{v}_e \times \mathbf{B}/c$, which counteracts the magnetic force and leads to equilibrium. Now consider a scenario in which the conductivity varies with height (see panel (b) of Figure 1.4). In this case, the current density $\mathbf{J}$, and consequently the electron velocity $\mathbf{v}_e$ and Hall electric field $\mathbf{E}_H$, become height-dependent. This variation generates an electromotive force (EMF), expressed as $\int \mathbf{E}_H \cdot d\mathbf{l}$, which induces a magnetic field component aligned with the current. As a result, the electron flow shears the magnetic field lines. In case of a magnetar, this shear is driven by spatial gradients in $\mathbf{B}$, $\mathbf{J}$, and ρ_e. The Hall timescale, $t_{Hall} = L/v_e$, characterizes the timescale over which this shearing occurs, where L is the characteristic lengthscale.

Ohmic decay is the process by which magnetic fields dissipate in a neutron star's crust due to its finite electrical conductivity. It results from electrons scattering off the ion lattice of the solid crust, which reduces the electric current and converts magnetic energy into heat (Gourgouliatos, De Grandis, & Igoshev, 2022; Lander, Andersson, Antonopoulou, & Watts, 2015). The rate of ohmic decay is inversely proportional to the electrical conductivity and independent of the magnetic field strength (Goldreich & Reisenegger, 1992). Although it is the most familiar mechanism of magnetic field dissipation, ohmic decay is generally too slow to significantly alter magnetic fields of stellar scale by itself.

Unlike Ohmic decay, which dissipates magnetic energy, Hall drift is a non-dissipative process that conserves magnetic energy while redistributing it (Goldreich & Reisenegger, 1992; Lander et al., 2015). It acts through the advection of magnetic flux by free electrons, leading to the formation of strong, small-scale magnetic struc-

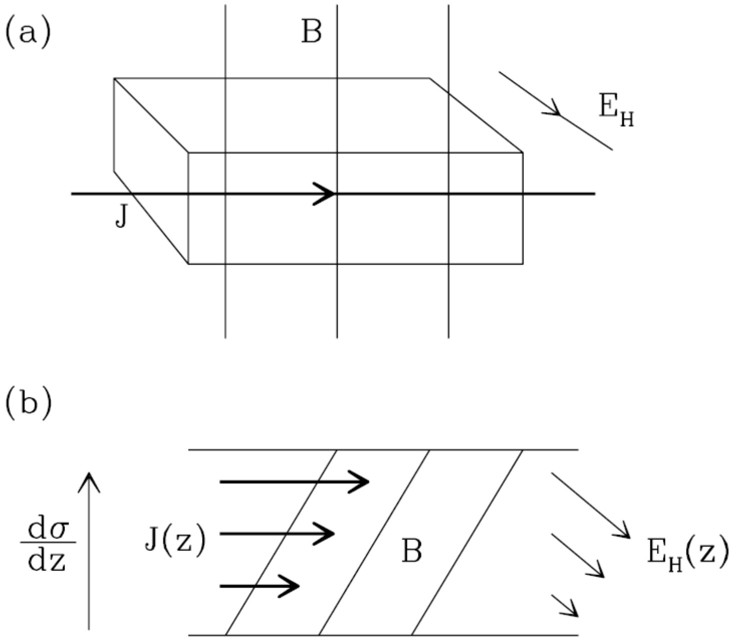

Figure 1.4 Basic illustration of the Hall effect (Cumming et al., 2004, used with permission). (a) Standard laboratory configuration where the Hall electric field counteracts the magnetic force acting on electrons in a conductor. (b) When electrical conductivity changes with height, the resulting variation in electron velocity creates a shear in the magnetic field over a characteristic timescale t_{Hall}.

tures (Gourgouliatos, Wood, & Hollerbach, 2016). Such localized intensification of the magnetic field can produce regions where the field strength exceeds 10^{15} G. Magnetic fields of this magnitude are sufficient to reach the crust's breaking stress and potentially trigger magnetar bursts.

Although Hall drift does not directly reduce magnetic energy, it plays a crucial role in enhancing Ohmic dissipation. It achieves this by transferring magnetic energy from large-scale structures − where Ohmic decay is inefficient − to progressively smaller scales, where the dissipation rate is much higher (Goldreich & Reisenegger, 1992; Lander et al., 2015; Pons & Viganò, 2019). Gourgouliatos et al. (2016) showed these magnetic instabilities in their simulations and argued that enhanced ohmic heating powers the star's persistent emission. The persistent emission may also arise from magnetospheric processes, such as bombardment of the star's surface by accelerated charged particles (Beloborodov, 2009).

Beginning from the early axisymmetric simulations, the study of electron MHD has advanced greatly, including full three-dimensional (3D) nonaxisymmetric simulations and better handling of the numerically challenging Hall term (Ascenzi et al., 2024; De Grandis et al., 2020; Dehman, Viganò, Ascenzi, Pons, & Rea, 2023; Gourgouliatos et al., 2016; Igoshev, Gourgouliatos, Hollerbach, & Wood, 2021; Wood

& Hollerbach, 2015). Furthermore, because ohmic decay causes heating, and the conductivity is temperature dependent, the full electron-MHD system becomes a coupled magnetothermal evolution; see Pons and Viganò (2019) for a review of this progress. The attractive feature of these simulations is that, while numerically challenging, they involve only a small number of well-understood transport properties of the crust.

For a subset of the possible initial conditions and boundary conditions, magnetothermal evolutions lead to the development of intense patches of magnetic field on kiloyear timescales, with Maxwell stress components that are comparable to the crust's elastic yield stress τ_{el} (Chugunov & Horowitz, 2010). This provides persuasive evidence that crustal field evolution drives crustal failure, and so the observed magnetar bursting activity. By resetting the local magnetic field when stresses build beyond some critical value, Perna and Pons (2011) arrived at simulated event rates and waiting times between bursts (see also Dehman et al. 2020), and identified factors that likely result in various occurrence rates of bursts from magnetars.

However, one should be cautious in simulating crustal failure with electron MHD, which itself is built on the assumption that the crust does *not* fail. To be self-consistent, the evolution beyond the failure point should also include a mechanism that describes the motion of the crust, with some velocity $\boldsymbol{v}$, under supra-yield stresses. This in turn causes advection of the field of the form $\nabla \times (\boldsymbol{v} \times \boldsymbol{B})$, which should be added to the right-hand side of Equation (1.1). Due to the intense pressure, voids are unable to form or propagate within the crustal lattice. Instead, the crust may flow plastically (Jones, 2003), allowing the release of stored elastic energy.

Here, we are interested in the case when high stresses can develop and be released through plastic flow, and this process requires ohmic decay to be subdominant. Given the high temperatures of typical young magnetars, this corresponds to field strengths of the order $10^{14}\,$G (Cumming et al., 2004). Generally speaking, ohmic decay dominates for weaker fields ($\lesssim 10^{12}$ G, see Figure 1.5). Neglecting the ohmic decay for simplicity, the resulting field evolution takes the form (Lander, 2016):

$$\frac{\partial \mathbf{B}}{\partial t} = -\frac{1}{4\pi}\nabla \times \left(\frac{c}{\rho_e}(\nabla \times \mathbf{B}) \times \mathbf{B}\right) + \nabla \times (\boldsymbol{v} \times \boldsymbol{B}), \tag{1.2}$$

where $\boldsymbol{v} = \mathbf{0}$ below the yield stress. Unlike electron MHD, this is no longer a system with a limited set of well-constrained parameters. The main line of work studying the evolution of Equation (1.2) to date (Gourgouliatos & Lander, 2021; Kojima, Kisaka, & Fujisawa, 2021; Lander & Gourgouliatos, 2019) has calculated a velocity $\boldsymbol{v}$ under some simplifying but plausible assumptions that reduce it to the dynamics of a viscous and incompressible fluid (Lander, 2016). Even this simplified system, however, has uncertainties relating to the unknown material properties of the crust at high stress and the fact that there is no universal theory of viscoplasticity that can be readily applied.

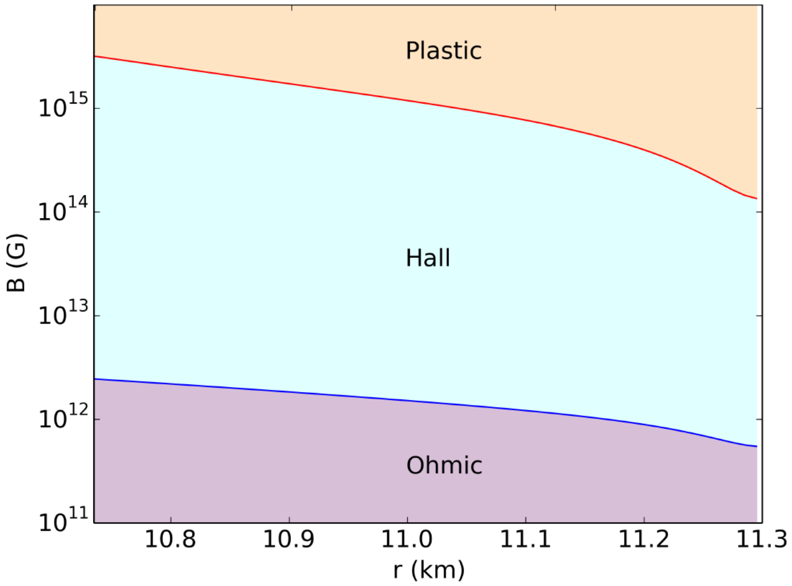

Figure 1.5 Dominance of plastic flow, Hall effect, and ohmic decay as functions of magnetic field strength and radial distance from the center (Gourgouliatos & Lander, 2021, used with permission). The left edge of the x-axis corresponds to the crust-core boundary, while the right edge marks the neutron drip point.

1.2 Cellular Automaton Magnetar Simulation

As discussed above, electron-MHD simulations show that stresses can quickly grow beyond the yield stress (Dehman et al., 2020; Gourgouliatos, 2023; Lander & Gourgouliatos, 2019; Perna & Pons, 2011), after which the simulations become physically unreliable as their inbuilt assumption of a static crust is violated. Furthermore, the standard paradigm for magnetar activity links their sudden bursts with failures of the crust. Crustal failure presents one particular conceptual challenge: While first-principles simulations indicate that the ion lattice fails collectively on a microscopic scale, this cannot extend to the global scale (otherwise, a very localized supra-yield stress could cause the entire crust to fail). With quantitative modeling very far away from being able to attack this problem, one alternative is to take a qualitative description of the evolution of crustal stress locally, and formulate a system where local regions can communicate with one another to produce larger-scale and non-deterministic behavior. This was the goal of an earlier cellular automaton model of the crust (Lander, 2023), whose main features we review next, including where specific choices may reduce the generality of the model.

To simulate the abovementioned approach, Lander (2023) divided the crust into an array of semiautonomous cells. Within each cell, the physical quantities are assumed constant and fixed to their value at the base of the cell. In both the original paper and this thesis, the stellar structure is calculated from the TOV equation using the SLy4 equation of state, the yield stress from the formula of Chugunov and Horowitz (2010), and the viscosity of the crustal matter in its plastic phase ν with the same profile as that of τ_{el}, together with the temperature-dependent prefactor suggested by Lander (2023). Guided by the results of 3D electron-MHD simulations (Gourgouliatos et al., 2016), which show the development of locally intense patches of magnetic field for young magnetars whose angular extent has a characteristic diameter $\sim 0.5-2\,\mathrm{km}$, Lander (2023) fixes the surface area of each cell to 1 km^2.

Because the outer crust cannot sustain high stress and has a lower melting temperature, only the inner crust is modeled. Equally, however, across the whole inner crust of thickness $\sim 0.5\,\mathrm{km}$ the yield stress changes by a factor of a thousand, meaning it is physically unlikely that any small failure would extend down to the crust−core boundary. For this reason, the cell depth is chosen to be smaller than this, 0.2 km, such that the yield stress variation is less than an order of magnitude. The density within a cell ranges from $4.0\times10^{11}\,\mathrm{g\,cm^{-3}}$ at the top, down to $1.5\times10^{13}\,\mathrm{g\,cm^{-3}}$ at the base. While the precise choice of depth is arbitrary, it is a plausible value over which collective failure of an entire cell could be expected (as required for a cellular automaton model).

The magnetoplastic evolution in Equation (1.2) may be reduced, in an approximate way, to an equation for a scalar stress $\tau \equiv B^2/8\pi$ that is assumed to be sourced by the magnetic field alone (see Lander 2023 for derivation):

$$\frac{\partial\tau}{\partial t} = \frac{c\tau^{3/2}}{\pi^{1/2}\rho_e L^2} - \frac{2\tau\,(\tau-\tau_{el})}{\nu} \tag{1.3}$$

where the first term on the right-hand side represents the increase of elastic stress due to the Hall drift, while the second term reflects the stress release due to the plastic flow. Because plastic flow is inactive below the yield stress but dominant over Hall drift above the yield stress, we can approximate the evolution as being due to only one of the two effects at any given time. With this prescription, a cell behaves elastically (see Figure 1.6) and its elastic stress accumulates under the dominant Hall effect if $\tau < 1.1\tau_{el}$, the first term on the right side of Equation (1.3). When the cell reaches a critical value of $\tau = 1.1\tau_{el}$, it fails and behaves plastically (see Figure 1.6). During its plastic phase, it releases the accumulated stress (the second term on the right side of Equation (1.3)); the amount of release is fixed at 10% of τ_{el}. In the end, τ reduces down to $1\tau_{el}$, corresponding to an energy release of $\sim 10^{40}$ erg – similar to an energetic short X-ray burst. The characteristic timescales (t_{Hall} and t_{pl}) for τ evolution under Hall drift and plastic flow then can be estimated as 800 and 9 yr, respectively, using $\rho_e = 1.4 \times 10^{26}$ esu cm^{-3}, $L = 200\,$m, $\tau = 1.1\tau_{el}$, and $\nu = 10^{36}\,$poise. However, typical durations for the Hall and plastic phases in the simulation are ~75 yr and 1 yr, respectively. Since the reduction of τ is only 10% of τ_{el} in the model, phase durations are shorter than the estimated characteristic timescales. Note that although the magnetic field strength does not appear explicitly in the formulation, our ansatz that the Hall phase builds stress in patterns that resemble the cellular lattice, and that ohmic decay is subdominant and may be neglected, both mean that we are implicitly assuming a typical crustal magnetic field strength in the approximate range of $10^{14} - 10^{15}\,$G.

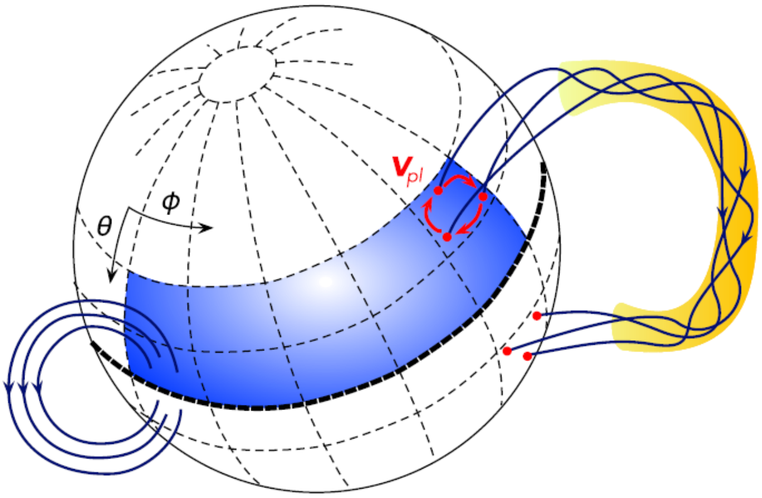

Figure 1.6 The magnetar crust as an array of cells (Lander, 2023, used with permission). The magnetic field lines shown on the left are untwisted and embedded in a static cell in its elastic phase, while the lines shown on the right are twisted due to the plastic flow v_{pl} circulating around a cell in its plastic phase.

Previous studies (Gourgouliatos & Lander, 2021; Lander & Gourgouliatos, 2019) have shown that the elastic stress of a cell may exceed the yield stress by some tens of percent before any significant effect of the plastic failure. Note that this is also required in order to produce a sudden release of energy – otherwise, a cell's evolution would saturate, with the plastic flow and Hall drift counteracting one another, to leave the stress at a constant value equal to the yield stress. Therefore, Lander (2023) model assumes an abovementioned critical value of $\tau = 1.1\tau_{el}$ for the failure of an individual cell. During its failure (plastic phase), its neighboring cells will be affected due to the exerted shearing force created by this plastic cell. To mimic this effect, the model includes a cell rule that allows varying yield stress between 1 and $1.1\tau_{el}$: A cell's yield stress is lowered by $0.025\tau_{el}$ from $1.1\tau_{el}$ for every plastic neighbor, assuming its behavior is only affected by its four neighbors. With this choice, if a cell has the maximum number of neighbors in the plastic phase, i.e., four, it enters the plastic phase as soon as its own stress reaches $1\tau_{el}$. Clearly, changing the precise values involved in the yielding process will result in quantitative differences in typical burst sizes. However, the main feature of the cell rule is robust: That nearby plastic flow expedites a cell's failure, and the simultaneous plastic phase of adjacent cells enables the model to produce high-energy magnetar activities like flares.

A cluster of adjacent plastic cells is considered a single but larger cell with a plastic flow through the entire cluster at an average velocity, $\overline{v}_{pl} \propto (\tau - \tau_{el})/\nu$. This plastic flow within a plastic cluster causes a braiding of external magnetic field lines due to their footpoints embedded in the cells, increasing the average twist (ψ) of the associated coronal loop, $d\psi/dt = \overline{v}_{pl}$. It also represents the rate of energy transfer from the crust to the corona, $E_{clus} = \psi E_{max}$, where E_{max} is the maximum expected energy considering all plastic cells in a cluster. The model simply assumes that when a plastic cluster ceases to exist, its associated energy is emitted as a single burst. Here, it is important to note that the transfer of elastic energy to burst energy released in high-energy photons is a highly complex process that may not be efficient (see, e.g., Beloborodov 2013). Given that Lander (2023) does not touch on this at all, his model is effectively degenerate in how much stress is relieved from the crust in a failure event, and the radiative efficiency of the emission process: An observed burst of energy 10^{40} erg could represent a 100% efficient transfer of 10^{40} erg of elastic energy, or a 10% efficient process following an initial crustal energy release of 10^{41} erg.

At the start of each simulation, the temperature (T) of all cells is set to a minimum "ambient" value of 5×10^8 K. During the plastic phase of a cell T increases due to plastic flow, and then returns to the ambient temperature linearly over 13 yr starting from the end of the plastic phase. At the end of the plastic phase, T reaches a broad peak (for roughly a year) around its peak value, which is at most $2.5 \times 10^9\,\mathrm{K}$. Note that temperatures much higher than this could not be maintained, anyway, since the crust is cooled efficiently by neutrino emission from plasmon decay (see, e.g., Figure 1 of Yakovlev, Kaminker, Gnedin, and Haensel 2001). The viscosity (ν) of the crustal matter is inversely proportional to T, and its possible range during a simulation is between 10^{34} and 10^{36} poise.

Since the newborn magnetar crust is unstressed and hence has no seismic activity, the time $t = 0$ yr represents a highly stressed young magnetar crust at age ∼1000 yr in this study. Therefore, the stress levels of the crust cells are assigned randomly between 0.9 and $1.1\tau_{el}$ at the start of each simulation, and hence they are all in the Hall phase at $t = 0$. Finally, we note that there are $56 \times 14 = 784$ crustal cells covering the active northern hemisphere of the magnetar, where crustal motion drives the increase in coronal twist; modelling half of the surface avoids conceptual issues related to whether an opposing crustal motion in the other hemisphere might annul coronal twist.

1.3 What Causes Clustering of Short Magnetar Bursts?

The basic picture of neutron star crustal energy release is that elastic stresses build up unobserved over the star's lifetime, until the crust's yield stress is reached, at which point stress is relieved through a failure of the crust, probably taking the form of a plastic flow. This flow will cause some localized heating, which could potentially be seen as an outburst: an additional thermal component of the X-ray spectrum that cools over some months. It does not, however, directly power the hard X-ray bursts that are our main focus here. Instead, the flow advects the footpoints of the magnetosphere, which twists up coronal loops. The presence of coronal loops may be seen indirectly by affecting the star's spin-down, or directly when these loops undergo magnetic reconnection, which returns them to a lower-energy and less twisted state; the excess energy is converted to an abrupt emission of high-energy photons together with, in some cases, a localized "trapped fireball" that decays more slowly, as seen most notably following giant flares (C. Thompson & Duncan, 2001).

A one-off burst does not itself provide stringent constraints on this sketch of how the magnetar's crustal energy becomes a photon count we can detect, but interpreting a cluster of bursts reduces the freedom in our modeling. As an example, let us consider the spectacular burst forest of SGR 1900+14 on 2006 March 29, first analysed by Israel et al. (2008). Figure 1.7 shows that over half a minute the magnetar emits several protracted bright bursts with long tails, as well as a number of shorter and less energetic bursts. Israel et al. (2008) refer to the former events, with higher energy and longer duration, as "intermediate flares," but conclude that there is no firm distinction between those and short bursts; we will simply refer to all as “short bursts.” This earlier study only reports the total energy of the burst storm, $\sim (2-3)\times 10^{42}$ erg, but for a physical interpretation of the burst mechanism it is helpful to have individual energies. We estimate that the brightest bursts have energies of $\sim (0.5-1.5)\times 10^{41}$ erg in 10-100 keV by assuming a distance to the source of 10 kpc. The initial rise of a burst − when it can be discerned − is quasi-exponential over $\sim 25-50$ ms, and the longer bursts feature a pseudo-linear decaying tail of duration ~ 1 s. The brightest bursts typically come $\sim 2-4$ s apart.

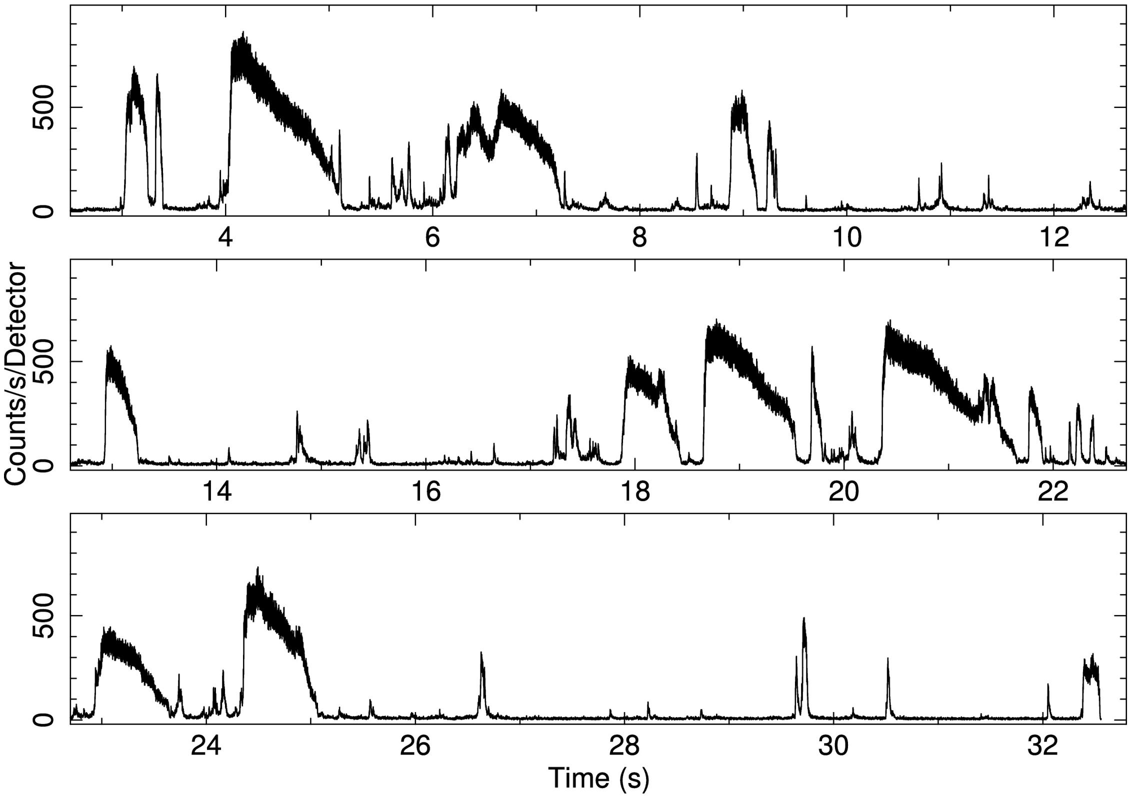

Figure 1.7 Light curve of the burst forest from the magnetar SGR 1900+14 recorded by *Swift*-BAT with 1 ms time resolution in the energy range of 15−100 keV on 2006 March 29 (Israel et al., 2008, used with permission)

We can now interpret the features of the burst forest of SGR 1900+14. The onset of each burst is likely to be the result of magnetic reconnection of a twisted coronal loop, with the protracted nature of the brighter bursts representing a small trapped fireball attached to the star. Each burst represents a local failure, since a large-scale event would both be more energetic and protracted enough in time to show rotational modulation (as seen in the decaying X-ray tails following the giant flares of SGRs 1900+14 and 1806−20). Furthermore, the energy release from the larger bursts $\sim 10^{41}$ erg is comparable to the maximum expected from the failure of a single $1\,\mathrm{km}^2$ crustal cell, so it is not possible to explain the whole ~ 30 s period of activity as a single twisted coronal loop undergoing repeated reconnection events, nor would persistent plastic flow in a single cell be fast enough to “recharge” the coronal loop with energy for a new burst, since the timescale for this process is likely around a month (Younes et al., 2022).

This leaves us with a scenario where several highly stressed local regions of the crust contribute to the burst storm. The first of these localized failures exerts a torque that increases the stress in the surrounding region, and will also send shear waves with speed $\sqrt{\mu/\rho}$ (where μ, ρ are the shear modulus and mass density, respectively) across the star's crust. The latter mechanism could, in principle, trigger distant crustal failures at any highly stressed point in the crust, but these would lead to subsequent events being separated by at most the shear-wave crossing timescale for the crust, $\sim 2\pi R_*/\sqrt{\mu/\rho} \approx 1$ s (where R_* is the stellar radius, which we take as 12 km). Instead, we see somewhat longer and nonregular waiting times between bursts, suggesting that the interaction between plastically failing cells and their surroundings may be driving the clustering. We wish to investigate whether Lander (2023)'s cellular automaton model, which aims to encapsulate magnetar activity with minimal assumptions, is able to explain this burst clustering.

1.4 Time-integrated and Time-resolved Spectroscopy

Hard X-ray spectral analyses of magnetar bursts play a crucial role in elucidating the underlying physical mechanisms driving these energetic events. The X-ray spectra of magnetar bursts are predominantly described using two continuum models: The first one is the sum of two blackbodies (BB+BB), while the second is a power law with a high-energy exponential cutoff (COMPT). These two emission models are fundamentally distinct in their physical characteristics. Blackbody radiation arises from a region in thermodynamic equilibrium and depends on the temperature of the emitting surface, whereas emission described by the exponential cutoff power-law model is typically attributed to synchrotron-like nonthermal processes. Comprehensive time-integrated spectral studies of magnetar bursts conducted to date (Lin et al., 2012, 2011; van der Horst et al., 2012) have demonstrated that both models provide statistically acceptable fits to the observed spectra.

Although studies on the spectral properties of magnetar bursts have been done since the late 1990s, they gained significant momentum with the observations enabled by the *Fermi* Gamma-ray Space Telescope (hereafter *Fermi*), which became operational in July 2008. These observations have enabled comprehensive spectral analyses. As an example, 29 bursts from SGR J0501+4516 during 13 days of activity in 2008 (August 22−September 3) have been observed with Fermi. Lin et al. (2011) found that spectra of all bursts can be modeled with the COMPT model, while the BB+BB model fits a significant portion of the spectra.

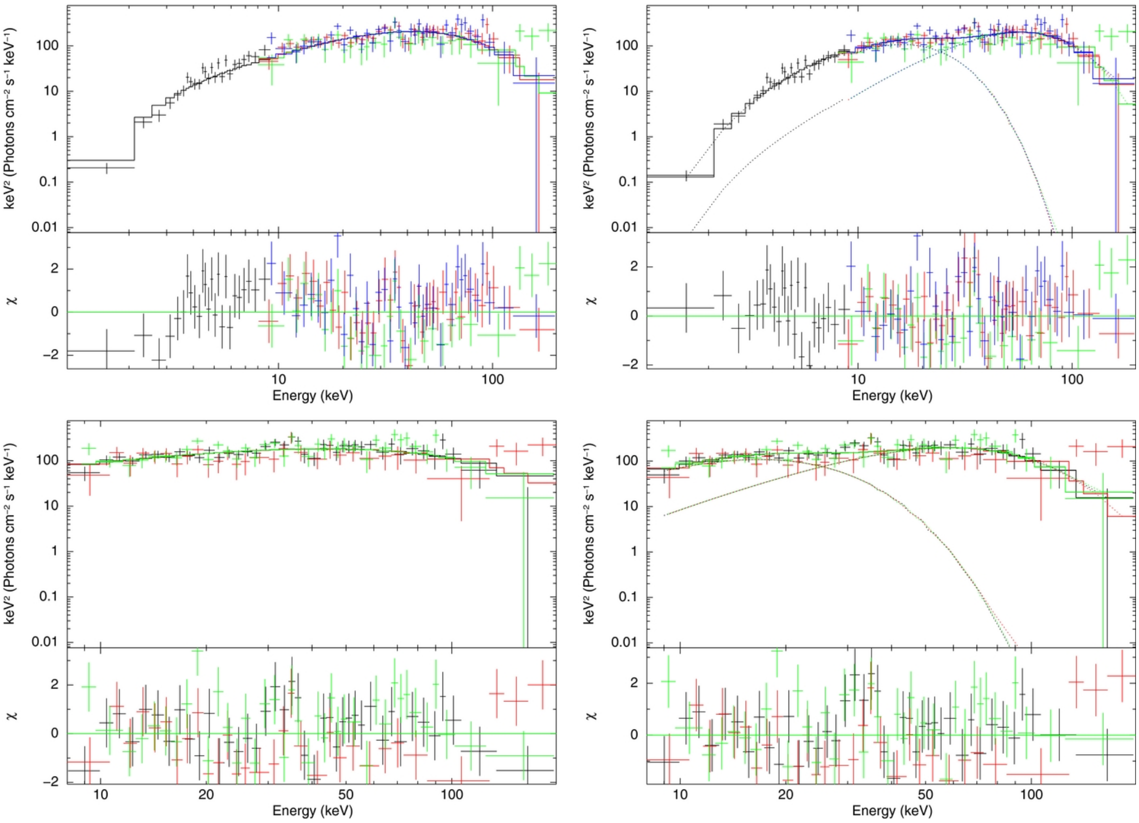

Figure 1.8 Spectrum of an example SGR J1550−5418 burst (Lin et al., 2012, used with permission). The top panels present the joint spectral fits using data from both XRT and GBM, while the bottom panels display the spectra extracted from GBM data alone. Spectral fits using the COMPT model are shown in the left column, and those using the BB+BB model are shown in the right column. Residuals corresponding to each fit are displayed in the lower sections of the respective panels.

van der Horst et al. (2012) conducted a spectral analysis of 286 bursts observed from yet another magnetar, SGR J1550−5418, during the January-February 2009 period using the Gamma-ray Burst Monitor (GBM) on board Fermi. Their study, based on spectra obtained in the 8−200 keV energy range, showed that the magnetar bursts could be equally well described by either the BB+BB or the COMPT model. Some of the bursts from the same magnetar observed with *Fermi*-GBM were also simultaneously detected by the X-ray Telescope (XRT) on board the *Neil Gehrels Swift* Observatory (hereafter *Swift*). Lin et al. (2012) analyzed the spectral properties of 42 bursts from the same magnetar observed simultaneously with both instruments over a broader energy range (0.5−200 keV) and concluded that the BB+BB model provided a relatively better fit to the data. However, as shown in Figure 1.8, the spectrum of an example burst from SGR J1550−5418 is comparably well fit by both the COMPT and BB+BB models.

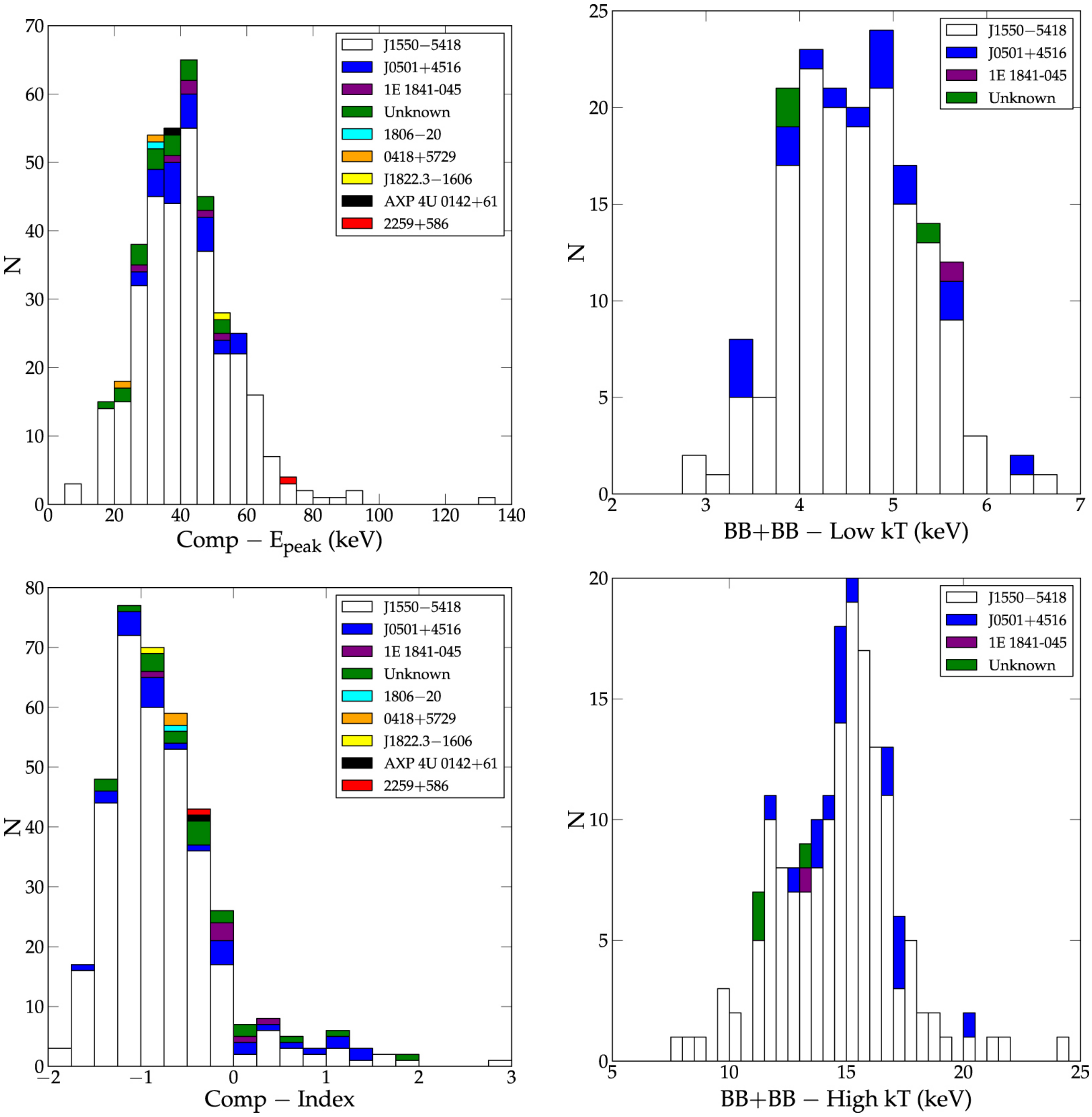

Figure 1.9 The distributions of E_{peak} (left-top) and photon index (left-bottom) parameters of the COMPT model, and kT_{Low} (right-top) and kT_{High} (right-bottom) parameters of the BB+BB model for all bursts in the magnetar catalog of Collazzi et al. (2015, used with permission)

Collazzi et al. (2015) compiled a magnetar burst catalog based on the first five years of observations with *Fermi*-GBM, presenting detailed temporal and spectral analyses of 440 bursts from various magnetars with high temporal and spectral resolution. We note that this dataset mainly consists of the abovementioned activities of the sources SGR J0501+4516 and SGR J1550−5418. In terms of spectral characteristics, considering all events of the catalog, the E_{peak} parameter of the COMPT model has a distribution clustered around ~ 40 keV (see the left-top panel of Figure 1.9). Photon index (Γ), the second parameter of the COMPT model, spans a range from

−2 to 2, peaking approximately at −1 (see the left-bottom panel of Figure 1.9). For the BB+BB model, the temperatures of two blackbody components (kT_{Low} and kT_{High}) are centered at $\sim$ 4.5 keV and 15 keV, respectively (see the right panels of Figure 1.9).

Time-resolved X-ray spectroscopy of magnetar bursts is an important probe to reveal spectral evolution throughout their highly complex emission episodes and helps uncover more dominant underlying physical mechanisms. One of the most comprehensive time-resolved burst spectral studies was performed by Israel et al. (2008) on the SGR 1900+14 bursts observed with the Burst Alert Telescope (BAT) and X-ray Telescope (XRT) on board Swift in 2006 March. Although the BB+BB model was at the forefront of this study including over 700 extracted spectra, a significant number of the spectra were also fitted with nonthermal models. Detailed analyses based on the BB+BB model revealed significant spectral evolution, even during short magnetar bursts. Younes et al. (2014) also performed time-resolved spectral analysis of the 63 brightest bursts from SGR J1550−5418 observed with *Fermi*-GBM and demonstrated flux-dependent variations between temperature (kT) obtained with the BB+BB model and the area (R^2) of the emitting region (see Figure 1.10). The flux-dependent variations of burst spectral properties have the potential to provide insight into the dominant underlying physical mechanism. If phases in which blackbody-like thermal emission is statistically dominant can be identified, flux-dependent variations could become even more pronounced.

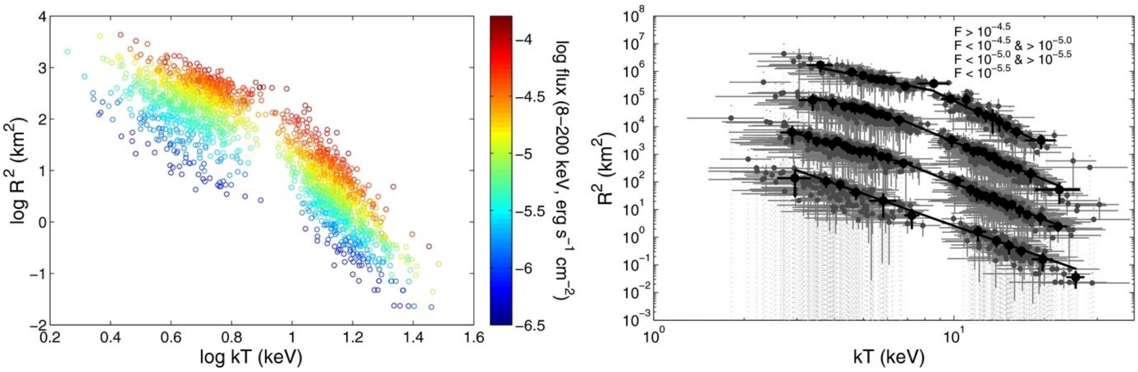

Figure 1.10 Flux-dependent variations between R^2 and kT observed in the spectra of SGR J1550−5418 bursts (Younes et al., 2014, used with permission). **[Left]** Flux color-coded plot of R^2 vs. kT **[Right]** Grouped R^2 and kT data based on flux intervals, from top to bottom as indicated by the legend. Solid lines show the best fits to the data.

In general, time binning for the extraction of spectra in time-resolved spectroscopy of bursts, however, is quite arbitrary. In earlier studies, the subsequent spectra were usually obtained from time intervals determined based upon the signal-to-noise ratio of its light curve. In other words, the time segments are not determined by taking into account the spectral changes in advance; instead, the burst is divided arbitrarily into time segments that contain a certain number of photons in order to ensure acceptable statistics for the spectral analysis. Under such circumstances, it would not be possible to elucidate the true spectral evolution of the observed burst emission.

One possible way to overcome the problem of arbitrariness in time-resolved spectroscopy is to employ sequential spectra extracted from the shortest possible time intervals (in terms of counts) and allow these segments to overlap subsequently. This way, it would naturally be possible to reveal more realistic spectral evolution, which in turn could help uncover more dominant underlying mechanisms. This sliding time window approach is a methodology often used in timing analysis, e.g., searching for time-dependent burst oscillation behaviors (see e.g., Strohmayer, Zhang, Swank, White, & Lapidus, 1998). In the study presented in Chapter 3, we apply a similar approach for the first time in the spectral analysis of SGR bursts; namely, "overlapping time-resolved spectroscopy," using the brightest bursts from SGR J1935+2154. We subsequently apply a machine-learning-based clustering algorithm to form nonoverlapping time intervals with significant spectral variations and perform "clustering-based" time-resolved spectral analysis of these bursts. Hence, the resulting time segments are expected to precisely reveal the burst spectral evolution.

To perform spectral modeling of SGR J1935+2154 bursts, we employ commonly-used BB+BB and COMPT models. In addition, we also employ the model of a modified black body (MBB) spectrum (Lyubarsky, 2002) that undergoes resonant cyclotron scattering (RCS), the combination of which is applied systematically to the SGR burst spectral analysis at this scale for the first time. The MBB-RCS model was developed by Yamasaki et al. (2020) to account for the magnetospheric effects on thermal emission in the context of magnetar flares. Lyubarsky (2002) had previously suggested extreme magnetic fields of magnetars could modify the emerging radiation from its surface, incurring significant deviations from a Planckian that result in a flat photon spectrum at low energies. However, the pure MBB model can underestimate the spectra at high energies by not taking the magnetospheric scatterings into account. The MBB-RCS model (Yamasaki et al., 2020) assumes that the photons emitted from the active burst region escape to infinity after just one resonant scattering by magnetospheric charges, thereby accounting for tails in the observed spectra at high energies. Testing the model with energetic flares of SGR 1900+14 resulted in a good agreement with the spectra of intermediate flares, but not with the giant flare observed in 1998.

SGR J1935+2154 was discovered on 2014 July 5, when a short burst triggered *Swift*/BAT. Follow-up observations with *Chandra* and *XMM-Newton* revealed its spin period ($P \sim 3.24$ s) and spin-down rate ($\dot{P} = 1.43 \times 10^{-11}\,\mathrm{s\,s^{-1}}$), corresponding to a magnetic field strength of $B \sim 2.2 \times 10^{14}$ G, and thus confirming the magnetar nature of the source (Israel et al., 2016). Since its discovery, SGR J1935+2154 has been the most prolific transient magnetar ever observed: it is burst-active almost annually, including multiple (in the range of thousand) short bursts (Lin, Göğüş, et al., 2020; Lin, Göğüș, et al., 2020), an intermediate flare on 2015 April 12 (Kozlova et al., 2016), and a burst forest on 2020 April 27 (Kaneko et al., 2021). Just hours after the burst forest, SGR J1935+2154 emitted an X-ray burst (e.g., Mereghetti et al., 2020) coincident with a Fast Radio Burst (FRB; Bochenek et al., 2020; CHIME/FRB Collaboration et al., 2020), which was the first Galactic detection of these events. This coincidence is the first indicator that magnetars residing in distant galaxies may also be the origin of FRBs (Petroff, Hessels, & Lorimer, 2019, 2021).

2. INVESTIGATING THE RECURSIVE SHORT X-RAY BURSTS OF MAGNETARS THROUGH CRUSTAL INTERACTIONS

This chapter was published in Keskin, Lander, and Göğüş (2025). Some parts were modified to ensure the continuity of this text. In Section 2.1, we explain the improvements and tests that we accomplished to the Lander (2023) model to study burst clusters. The results are presented in Section 2.2 and discussed in Section 2.3.

2.1 Model and Simulation

The model outlined in Lander (2023) allows for magnetar activity across a full range of energies, corresponding to those of short bursts and intermediate and giant flares, all of which are powered by the release of stress from a crust that behaves as a cellular automaton and drives coronal and then bursting activity. The motivation for the original code was to model the energy output from a magnetar on long timescales rather than to resolve short-timescale phenomena specific to any particular magnetar, but the model can readily be extended and adapted to study many magnetar activities. Our study aims to understand the nature of short magnetar bursts by focusing the simulation on high-energy short bursts of magnetars. To do that, we aimed to match the model results with short magnetar burst observations. While doing so, we ensured that all new implementations to the code were physically motivated and meaningful. In the following, we describe the four differences between the present implementation and that of Lander (2023), each detailed in one paragraph.

To study short bursts, we focus on shallow failures of the cells with a depth of 0.2 km (a density range $4.0 \times 10^{11}\,\mathrm{g\,cm^{-3}} < \rho < 1.5 \times 10^{13}\,\mathrm{g\,cm^{-3}}$). This means that a cell does not fail deeply, down to the crust−core boundary. The original version of the simulation also allowed these deeper failures to explain the larger energy activities, such as intermediate and giant flares. This was intended as a way to model whatever additional physics might — in rare instances — cause a larger spreading failure across the crust, in whose wake the magnetar would become significantly less active (as seen in the aftermath of the three giant flares observed locally to date). Clearly, however, the rarity of giant flares indicates that their trigger may only occur once in several decades or more, whereas here we are interested in the far more common small bursts, and their clustering over short timescales. It does not make sense, therefore, to implement the previous deep-failure criterion in this case.

We also changed our assumption about how energy is released from a group of neighboring cells. In Lander (2023), it was assumed that contiguous regions of plastic cells all contributed their energy to a single large-scale coronal loop. This approach was also needed to explain higher-energy flares, since even the deep failure of a single cell does not reach the $\gtrsim 10^{44}$ erg energy range needed to explain a giant flare. Here, we therefore assume that each cell releases energy to the corona individually, which allows the possibility of several successive, distinct bursts occurring in a local region due to cell interactions.

As mentioned in Section 1.2, crustal magnetic field lines that are dragged around in a cell due to its circulating plastic flow exert a shearing force on its neighboring cells, therefore nearby plastic failure quickens a cell failure. While encoding this effect, the motivation for the cell rule in Lander (2023) is to allow simultaneous plastic phases of many adjacent cells in order to model the rarely-observed giant flares. Here, we focus on the far more frequently observed short bursts, and from magnetar observations we know that these do not usually occur in isolation but rather successively. To mimic this behavior of magnetar bursts, we need to make a cell more sensitive to its neighbors' behavior. To achieve this in our simulation, we modified the cell rule: If a cell has one or more (two, three, or four) plastic neighbors, it fails for any stress above τ_{el}; otherwise, it fails at $\tau = 1.1\tau_{el}$. With the modified cell rule, we increase both the number of cell interactions and the number of successive failures of a cell compared to the original version. In general, when a cell fails and enters a plastic phase, it has at least one plastic neighbor and fails successively usually twice, and at most ~5-6 times.

When a cell fails, we do not expect it to release all its stress, but rather a portion of it. In the original model, this portion was a fixed value, namely a 10% reduction. However, an arbitrary amount of stress loss is more likely and physically expected. Note that the amount of stress reduction is directly related to the amount of energy transferred to the corona via braiding of the magnetic field lines due to plastic flow during failure. From the observational point of view, less energetic bursts are more frequently observed, and so are more abundant than the higher-energy ones.

Therefore, when a cell fails, instead of a fixed stress loss (τ_{loss}), we assumed a random τ_{loss} between $0.01\tau_{el}$ and $0.6\tau_{el}$ drawn from a power law (PL) distribution with an index of 1.6. This allows us to cover an energy range of $10^{39} - 10^{41}$ erg, which is the typical energy range of recursive short bursts. More importantly, this approach enables us to obtain a burst energy distribution that follows a PL trend whose index is 1.6, consistent with the burst energy distribution of real magnetar burst observations (Göğüş et al., 1999; Göğüş et al., 2000). Figure 2.1 shows the burst energy distribution of the model star through the 1000 yr evolution of all crust cells. We found that the distribution follows a PL trend whose index is 1.60 ± 0.01 with its 1σ uncertainty.

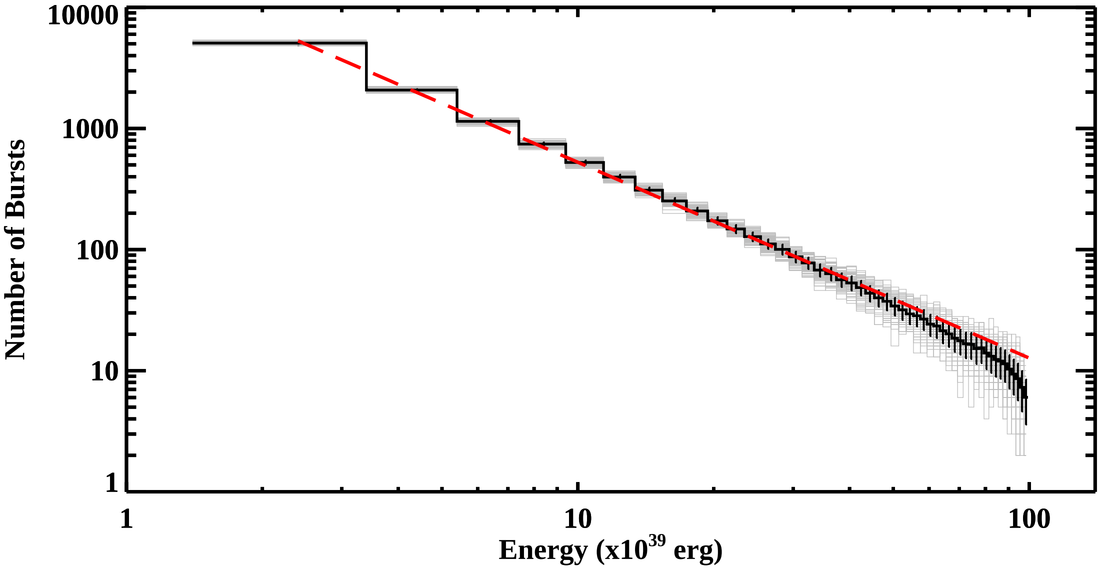

Figure 2.1 The distribution of burst energies obtained by averaging 100 simulations (solid black lines). The red dashed line shows a PL fit to the average distribution. The gray lines display the distributions of individual simulations.

2.2 Results

Including the abovementioned implementations, we simulate short magnetar burst activities for a fiducial simulation duration of 1000 yr. As a reminder, t=0 yr represents a highly stressed young magnetar whose age is ~1000 yr in our simulation. This is enough time to collect reliable statistics for burst clustering that vary little from simulation to simulation. Having experimented with longer simulations, we found these give no additional information, as the cellular automaton behavior saturates in well under 1000 yr, and because there is no additional secular evolution of the system on long timescales. Besides, observationally, burst-prolific magnetars have low characteristic ages, at most a few kiloyears, and our motivation is to investigate these highly stressed young magnetars in their burst-active states.

Figure 2.2 presents the duration distribution of the Hall (left panel) and plastic (right panel) phases of cells. Both Hall and plastic phase durations vary in our simulations due to a random amount of stress release rather than a fixed one (e.g., 10%) during a cell's failure. A Hall phase generally lasts between ∼1 and 1000 yr, with an average of 50 yr. It occasionally lasts less than a year; these cases are due to cells that have lost a small amount of stress, down to just below their yield values. Therefore, their stress levels again reach their yielding values more quickly. The relation between the amount of τ increase during a Hall phase and its duration is simple: The higher the stress increase, the longer the phase duration. On the other hand, there is a rather complex relation between the plastic phase duration and τ_{loss} during a plastic phase. The plastic phase duration depends on the τ values at which the plastic phase begins and ends, and viscosity (hence the temperature of the failing cell). Yet, we have a well-constrained plastic phase duration between one-third of a year and one year (0.3 - 1 yr), with an average of 0.7 yr. Therefore, a second burst from the same cell cannot be observed on shorter timescales than the plastic phase durations, even in the case of successive cell failures.

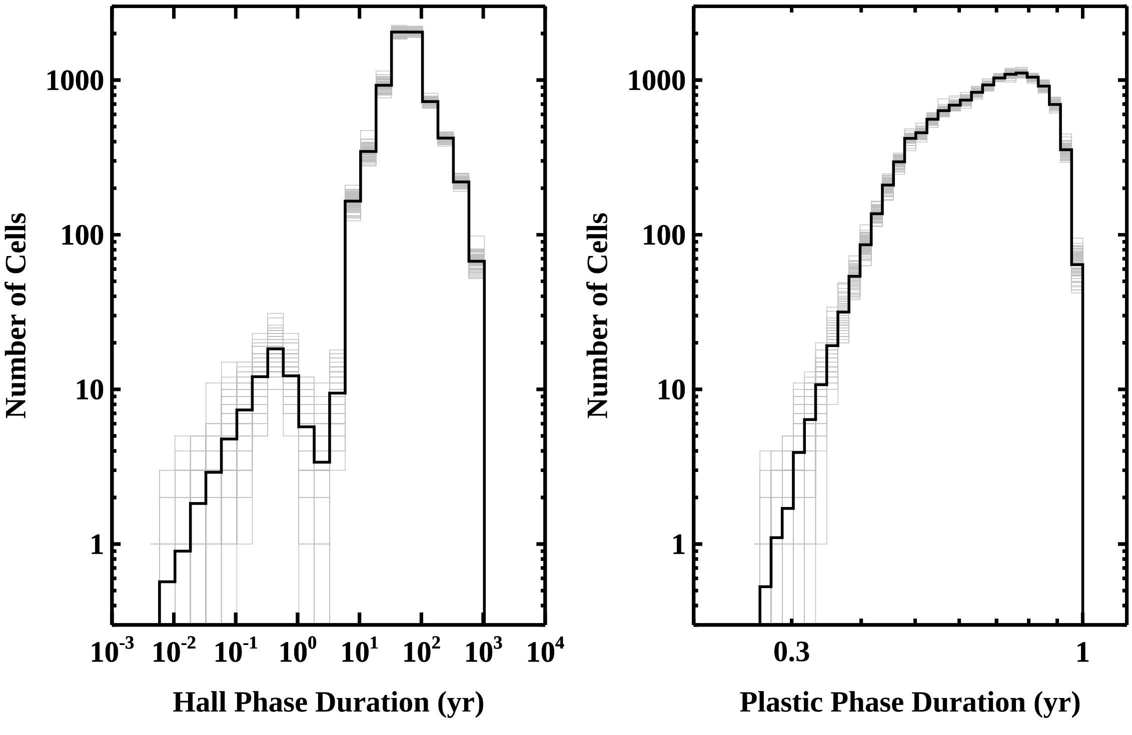

Figure 2.2 The distribution of Hall (left panel) and plastic (right panel) phase durations. Both trends shown with solid black lines were obtained by averaging the results of 100 iterations. The gray histograms display the distributions of individual simulations.

Figure 2.3 shows the distribution of the number of bursts per cell. We find that a cell yields, on average, around 16 events. This is understandable given that the Hall phase lasts about 50 yr on average, therefore, each cell releases energy to the corona ∼20 times over the course of 1000 yr. We also calculated waiting times between successive bursts from the same cell, considering all cells throughout the entire crust. We present this distribution of waiting times in Figure 2.4. The cells fail repetitively due to the cell rule (successive plastic phases of the cells), and since the plastic phase takes ∼ 0.3 - 1 yr, these cases create the data points around the first peak we observe in the figure. Nonsuccessive cell failures create the large region around the second peak in the figure since these cases include a Hall phase in addition to a plastic phase between the two bursts, therefore it requires a longer time for a cell to reburst since a Hall phase is generally much longer than a plastic phase (see Figure 2.2). The small additional overabundance of bursts jutting out from this broad peak at $\sim 70 - 80$ yr corresponds to the numerous cases where a single cell with no plastic neighbors fails on its own at $1.1\tau_{el}$ and loses an average amount of stress from the PL distribution and so drops back to $\sim 1.0\tau_{el}$, similar to the generic single-cell failure from (Lander, 2023). In the most extreme cases, large stress reductions in the plastic phase mean that the subsequent Hall phase takes hundreds of years to bring that particular cell back to the point of failure and, if this is followed by another large plastic failure, it may only produce (say) two bursts over the 1000 yr run of the code.

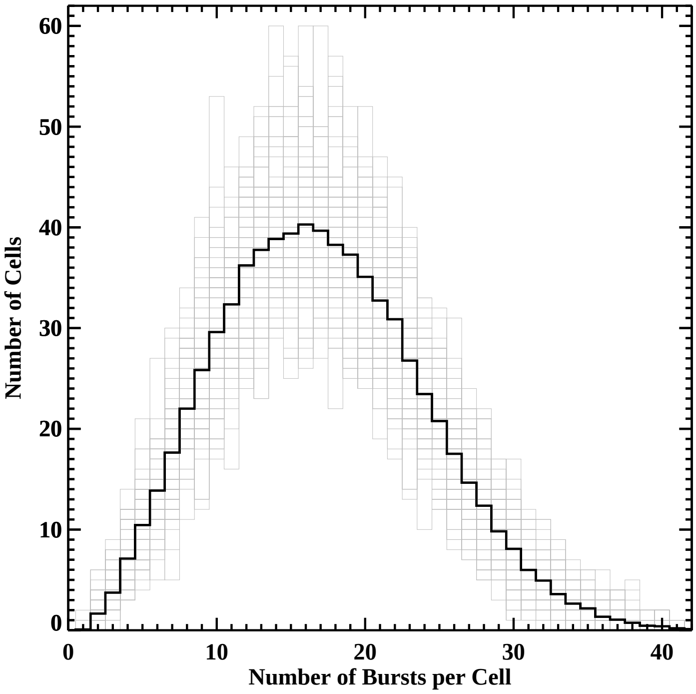

Figure 2.3 The distribution of the number of bursts per cell in 1000 yr, obtained as an average of 100 simulations, is shown in black. The gray histograms show the distributions of individual simulations.

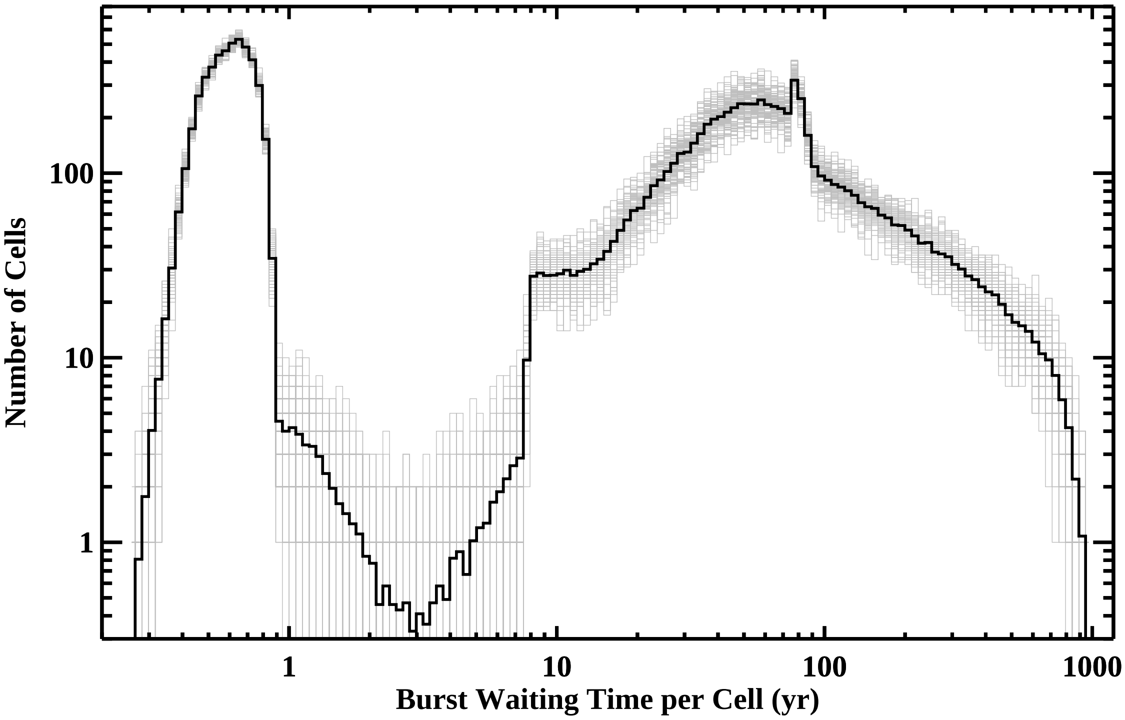

Figure 2.4 The distribution of waiting times between successive bursts from the same cell, considering all crustal cells. The solid dark line is the average of 100 simulations, and the gray lines are the distributions of individual simulations.

As an important outcome of our new approach, we obtain clustered bursting episodes in time and present them in the top panel of Figure 2.5. The bottom panel of Figure 2.5 shows the bursts obtained with the original cell rule to compare the two distinct bursting behaviors. To enable direct comparison between the evolution shown in the top panel of Figure 2.5 and Figures 2 and 3 of Lander (2023), we next look at details of the coronal energy and crustal stress evolution for our modified cellular automaton simulation. In the left-hand panel of Figure 2.6, we plot the total coronal energy as a function of time over 1000 yr for our modified cellular automaton model; the main differences compared with the original approach are the lack of very bright ($\gtrsim 10^{43}\,$erg) events, and the more frequent drops to zero coronal energy, leading to a more jagged-shaped line. In the right-hand panel of Figure 2.6, we show three snapshots of τ/τ_{el}: directly before and after the large burst cluster at time $\sim 38\,$yr, and the final state after 1000 yr. As one of the cells in a highly stressed crustal region (blue window in the top panel) fails, it quickens the failure of its neighbors, shown in the window, and they all fail together and start to affect other neighboring cells. The burst cluster can be seen to result in a large region of relatively low stress (large red patches in the middle panel), but − unlike the original model's deep-failure criterion − this is not permanent, and no trace of it can be seen in the 1000 yr snapshot (bottom panel).

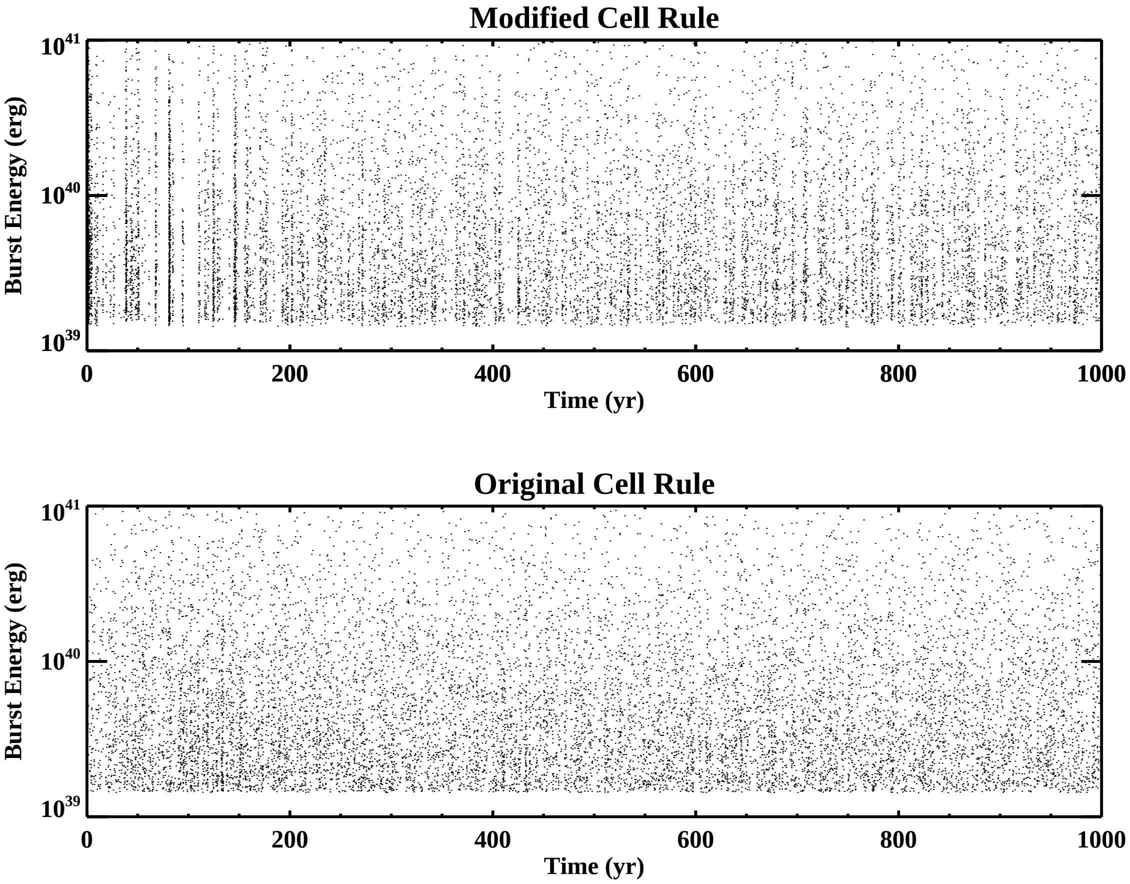

Figure 2.5 Energy of bursts over 1000 yr obtained with the modified cell rule (top panel) and with the original cell rule (bottom panel). Clustering is clearly more pronounced with the modified rule.

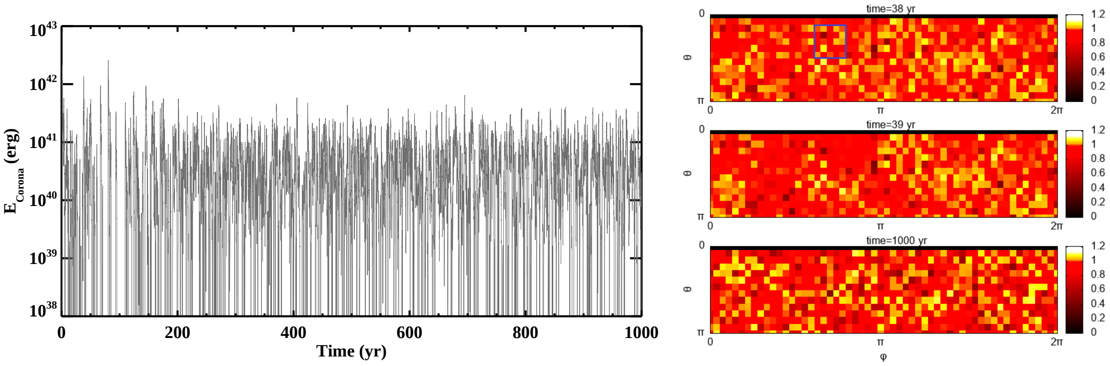

Figure 2.6 [**Left**] The total twist energy of all coronal loops vs. time during the 1000 yr evolution with our modified cellular automaton. [**Right**] Snapshots of stress evolution in units of τ/τ_{el} (colorscale) across the northern hemisphere, just before (top) and after (middle) the emission of a burst cluster with energy $2{\times}10^{42}$ erg, and at the end of 1000 yr of evolution (bottom), for the same simulation as in the left-hand panel of this figure and the top panel of Figure 2.5. The blue window shown in the top panel represents the highly stressed crustal region that triggered the successive failures.

The clustering of bursts in time is a direct indicator of burst-active episodes of magnetars. However, defining the interval of burst clusters within a simulation is not straightforward. In our set of simulation runs, the number of bursts varied between around 12,000 and 13,000, with an average of ~12,500 bursts, of which ~10,000 are single bursts in the days they occurred. The rest of the bursts (~2000) accumulated such that there are 2-10 bursts in a single day. In other words, there was no activity during ~355,000 (97%) days in 1000 yr. To define a burst cluster, we grouped the burst-populated days based on having two or more bursts. Time intervals with at least 100 subsequent days of no activity (two or more bursts) are considered burst-quiescent episodes. Therefore, the duration of a burst cluster is then determined as the time from the activity onset to the beginning of the following burst-quiescent interval. In Figure 2.7, we present the duration of burst clusters versus the total energy of bursts within corresponding clusters. We note that the durations of burst clusters lie on the integer values in the figure since we used a time resolution of 1 day while binning the data.

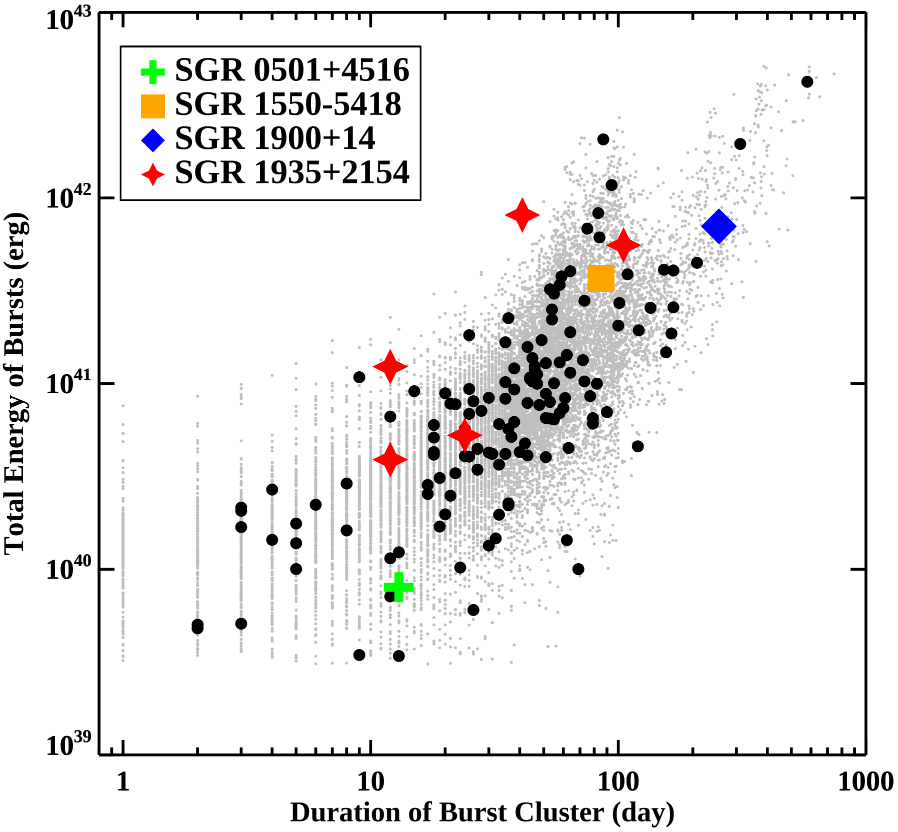

Figure 2.7 Plot of the total burst energy vs. duration of each cluster from 100 simulations (gray dots). The black circles show the results of a single simulation (the one shown in the top panel of Figure 2.5). Colored data points represent the same relation for the actual observations of magnetars: SGR 0501 + 4516 (green cross), SGR 1550 − 5418 (orange square), SGR 1900 + 14 (blue diamond), and SGR 1935 + 2154 (red stars).

To compare the duration and energetics of burst clusters with actual magnetar bursting activities, we utilized time-integrated spectral studies of recursive short magnetar bursts in the literature. Using the abovementioned burst cluster definition, we could identify burst clusters for four magnetars (see Table 2.1). For SGR 0501+4516, SGR 1550-5418, and SGR 1935+2154, we used the burst energy fluence values in 8−200 keV observed with *Fermi*-GBM and calculated the isotropic burst energies assuming distances to the sources provided in the table. Similarly, we obtained the total energy released from the short bursts of SGR 1900+14 by using the burst fluence values in > 25 keV observed with *CGRO*-BATSE and the distance to the source given in the table. Overplotting the durations and energetics of burst clusters from the observed magnetar activities in Figure 2.7 reveals a convincing agreement with our simulation results. To quantify this consistency, we obtained log-normal distributions of the total burst energies from 100 simulations (gray dots), corresponding to the burst cluster durations of actual magnetar bursting activities. We found that most observational data shown in Figure 2.7 remained within about a 2σ level of the associated energetics distributions. We note that only one burst cluster of SGR 1935+2154 (which occurred in April−May 2020) corresponds to the observed energetics that is slightly exceeding the 3σ level.

Finally, we note that we performed more simulations with different initial stress levels and different cell rules, to check whether our results were generic outcomes of the simulation or instead had some strong dependence on the specific choices we made. We still obtained a similar clustered bursting behavior of short bursts, confirming the robustness of our results (see Appendix A.1).

Table 2.1 A Sample of Magnetars with Extensive Burst-active Phases

Source Name	**Activity Period**	**Distance (kpc)**	**Total Energy of Bursts (10^{39} erg)**	**References**
SGR 0501+4516	2008 Aug−Sep	2	8	(1), (2)
SGR J1550−5418	2009 Jan−Apr	5	370	(1), (3)
SGR J1900+14	1998 May−1999 Feb	10	703	(4), (5)
SGR J1935+2154	2015 Feb−Mar	9	39	(6)
	2016 May−Aug		557	(6)
	2019 Nov		123	(7)
	2020 Apr−May		810	(7)
	2021 Jan−Feb		53	(8)

Notes.
References: (1) Collazzi et al. (2015); (2) Xu, Reid, Zheng, and Menten (2006); (3) Tiengo et al. (2010); (4) Göğüş et al. (1999); (5) Israel et al. (2008); (6) Lin, Göğüş, et al. (2020); (7) Lin, Göğüș, et al. (2020); (8) L. Lin et al. 2025, in preparation

2.3 Discussion

Burst clusters are among the most spectacular activities of magnetars, and – unlike the ultrarare giant flares – are relatively common. Despite this, to our knowledge, there has been little attempt to provide a theoretical interpretation of this phenomenon. Li, Levin, and Beloborodov (2016) studied the Hall waves that are emitted during each crustal failure with a 1D model. These waves propagate and trigger the failures of other regions as a potential source for magnetar outbursts, which are long-lasting (weeks to many months) persistent X-ray flux enhancements (Coti Zelati et al., 2018). The bursts in the focus of this study, on the other hand, are of short-duration hard X-ray events. While our model does also include a plastic heating term coinciding with the short bursts which broadly resembles the physics of an outburst, we have not attempted any detailed modeling of this process in detail.

Having experimented with some minor modifications to a previous cellular automaton model for the magnetar crust (Lander, 2023), we have found that we can reproduce the basic features of real magnetar burst clusters. We stress, however, that our success in matching observations is not a result of fine-tuning of many variables; there are only a limited number of adjustable parameters or prescriptions in this model, and the results we obtain are robust to quantitative changes in these parameters (see Appendix A.1 for some tests of this). With the agreement between our model results and real magnetar observations, we can now invert the reasoning to infer details of the physics of the magnetar crust and to consider when our model is applicable.

One change implemented here was to allow the reduction in stress in a cell's plastic phase to be taken randomly from a PL distribution rather than a value fixed by the number of plastic neighbors the cell has. Because cell stress relief directly corresponds to burst energy in our model, this allowed us to produce short bursts over a realistic energy range corresponding to magnetar observations. However, it also provides a very plausible physical picture of the crustal failure process: Local anisotropies due to, for example, seismic history and failure dynamics are indeed likely to lead to variable stress relief in a plastic phase (see also Li et al. 2016).

Within our model, a burst cluster can arise as a result of successive short plastic phases of the same cell or different cells triggering one another. Our model simply assumes that all energy transferred to the corona is emitted at once at the end of a plastic phase, since it does not include emission physics, and so both kinds of "burst" look similar in our simulations. More realistically, this energy would be temporarily stored in twisted coronal loops and then released due to magnetic reconnection in one or more events. Following the reconnection, synchrotron-like nonthermal radiation spectra are expected from these events due to particle interactions in the magnetosphere. Here, it is unknown whether the energy transferred to the corona from a single cell will create a single burst or multiple bursts. However, from the arguments at the start, we do not expect repeated large bursts, since each cell can release a total energy no greater than $\sim 10^{41}$ erg.

As can be seen in Figure 2.7, the duration of a burst cluster from our simulations is mostly in the range of $10-100$ days. We know that the minimum amount of time required to obtain a second burst from the same cell is given by the minimum duration of the plastic phase, which is one-third of a year ($\sim$ 120 days; Figures 2.2 and 2.4). Therefore, bursts in a cluster are mostly due to the failures of different active cells. This can be seen visibly in maps of the crust's stress: Directly after any large burst cluster, a substantial contiguous low-stress region can be discerned (see the right-hand middle panel of Fig. 2.6). We can interpret this as any highly stressed region being able to affect its neighbors quickly, and hence make the magnetar burst-active. Although a single active coronal loop is theoretically possible, we generally do not observe any coronal loop that twists repeatedly within the duration of a burst cluster in our simulations, considering the required time interval for a plastic flow to recreate enough twists for a second reconnection, unless a burst-active episode lasts long enough to create multiple bursts from the same cell (assuming successive and small failures). Therefore, most of the successive events we identify here as "burst clusters" are due to active neighboring cells from an active region(s). Then, successive small failures of a single cell may lead to consecutive clusters of bursts with short quiescent periods. This can be interpreted as the behavior of magnetars that become almost annually active, such as SGR J1935+2154. Since the remaining stress of the cells is still high enough, they can reach their yielding stress quickly and become active repeatedly until they release enough elastic stress to be silent for a longer period.

There is a compelling similarity between our model and observations of burst-energy output. In Figure 2.7, we plotted total burst cluster energy output as a function of duration, finding that both simulated and real data exhibit the same strong correlation. This suggests that although burst clusters represent episodes of significant seismic activity, the luminosity during a cluster is relatively constant (however long it lasts), showing that short-burst events often trigger other short-burst events, but do not cause a runaway effect leading to more violent phenomena. In particular, given that the total elastic energy reservoir in a fully stressed magnetar crust is over $\sim 10^{46}$ erg (Lander, 2023; Lander et al., 2015), even the most protracted burst clusters are unlikely to release more than one-thousandth of the total crustal energy reservoir. This strongly suggests that producing a giant flare requires one distinct additional physical ingredient, beyond those in the model discussed here. Lander (2023) tried to encapsulate this additional physics in a "deep failure" cell rule, but without pinpointing what exactly that would mean physically.

The original model (Lander, 2023) regarded collections of plastic cells neighboring one another as a single entity: a region where the plastic flow circulated around the entire domain, twisting up a geographically large-scale coronal loop whose energy was considerably larger than that associated with the coronal loop of a single cell. This characterization was useful for producing highly energetic "events" in the approximate energy range $10^{43} - 10^{45}\,$erg. However, it also prevents clusters of bursts from occurring due to neighboring cells interacting, since those neighbors would simply join to make a single larger burst $-$ and so we ceased to use that rule here. Instead, the physical picture we have is of a more complex corona, with potentially large numbers of physically distinct, thin coronal loops of a diameter similar to that of the cell they emerged from, $\sim 1\,$km.

With the rarity of giant flares, and our present focus on more typical events on shorter timescales, there was no reason to enable the additional, complicating feature of deep failures from the original model (which were assumed to occur when a critical number of neighboring cells were plastic). Instead, however, we have a greater sensitivity to failure if a cell has just one plastic neighbor. This suggests that even if a magnetar has suffered a giant flare that reduces stress across large patches of its crust, it would still be able to power burst storms even from the small, isolated active regions that remain; this provides a physical picture for the 2006 burst storm of SGR $1900+14$, 7.5 yr after its giant flare (Israel et al., 2008).

3. CONCISE SPECTROTEMPORAL STUDIES OF MAGNETAR SGR J1935+2154 BURSTS

This chapter was published in Keskin et al. (2024). Some parts were modified to ensure the continuity of this text. In Section 3.1, we introduce the instrument, the data, the SGR J1935+2154 bursts that we studied, and their spectral data extraction process. In Section 3.2, we explain the steps in the spectral analysis: first overlapping (3.2.1) and then clustering-based (3.2.2) time-resolved spectroscopy. The results are presented and discussed in Section 3.3.

3.1 Spectral Data Extraction Process

Fermi has been providing an enormous amount of data that allow for studying a wide range of gamma-ray transient events over the last 15 yr. It carries two instruments: the Gamma-ray Burst Monitor (GBM; $\sim$ 8 keV$-$40 MeV) and the Large Area Telescope (LAT; $\sim$ 20 MeV$-$300 GeV). GBM consists of 12 sodium iodide (NaI) detectors ($\sim$ 8 keV$-$1 MeV) and two bismuth germanate (BGO) detectors ($\sim$ 200 keV$-$40 MeV) (Meegan et al., 2009). Since the bulk of emission from magnetar bursts is typically seen in $\lesssim$ 200 keV, we only used the data of NaI detectors for this study. We employed Continuous Time-Tagged Event (CTTE) data from GBM, which provides the finest time (2 μs) and energy (128 channels) resolutions. Our investigations were performed in the 8$-$200 keV energy band with 4 ms minimum time resolution. For each burst, we included data collected with the three brightest NaI detectors[1] with the detector-to-source angle being less than 60$^{\rm o}$. Additionally, we excluded detectors if they are partially or fully blocked by other parts of the spacecraft as obtained using the GBMBLOCK software provided by the GBM team.

---

[1] Detectors with the lowest detector-to-source angle at the time of the event.

We selected 51 SGR J1935+2154 bursts observed with *Fermi*-GBM between 2014 and 2022 for our time-resolved spectral investigations, based on the results of time-integrated analyses (Lin, Göğüş, et al., 2020; Lin, Göğüş, et al., 2020, L. Lin et al. 2025, in preparation). In particular, we chose the bursts that contain at least 2400 background-subtracted counts, to ensure that they have enough statistics for time-resolved spectral analysis (See Appendix B.1). Our investigations are done in two stages for each burst: First, we define the overlapping time segments with which we obtain spectral parameters and use a machine-learning clustering algorithm to obtain "change point" for the parameter evolution. Then, we analyze spectral data extracted from the (non-overlapping) time intervals between these change points to better characterize spectral evolution.

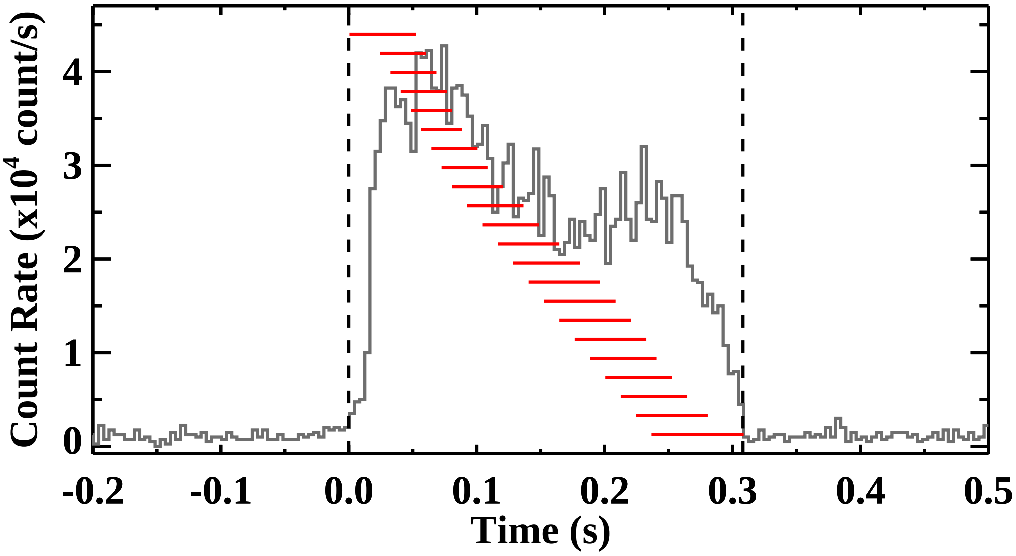

Figure 3.1 Light curve of an SGR J1935+2154 burst detected at 2021 January 29 10:35:39.918 UTC as seen with the brightest detector (n5). The vertical dashed lines show the Bayesian Block duration start and end times, respectively. The red horizontal lines represent the 22 overlapping time segments, with each subsequent segment having an overlap of 80%. We note that the vertical values corresponding to the red lines are arbitrary, and they have been chosen only for display purposes.

In the first stage of our time-resolved spectral studies, we required each time segment to overlap with the previous time segment by 80%. In other words, the subsequent time segment does not start from the end of the previous one, but from the time that is one-fifth of the previous segment (see Figure 3.1 for an example). We also required a minimum of 1200 background-subtracted counts in each time segment (See Appendix B.1). This way, burst spectral parameters are expected to be well-constrained and statistically reliable throughout each burst. We note that, for each burst, we calculated duration[2] via the Bayesian Block method optimized for photon-

---

[2] The details of duration calculation as well as background estimation can be found in Appendix B.1.

counting time series (Scargle, Norris, Jackson, & Chiang, 2013), and we started the first time segment from the beginning of the Bayesian Block duration.

Time segments starting before the peak of a burst are prone to end at the peak – although they are shifted by 20% of the time length of their previous ones, due to the fact that the flux rise timescale in short magnetar bursts is usually shorter than that of decay (Göğüş et al., 2001). This yields an accumulation of time segments at the beginning of the bursts. In those cases, we avoided the accumulation of time segments by reducing the overlap by 5% (75%, 70%, etc.) until the endpoint of the subsequent time segment ends later than the end of the previous one. In the end, we obtained in total 1343 overlapping time segments, hence spectra, from the 51 bursts for the first stage of our spectroscopy investigation.

3.2 Spectral Analyses & Results

We performed our spectral analysis with XSPEC (version 12.12.1) using Castor Statistics (C-stat; Cash, 1979). We also generated Detector Response Matrices (DRM) with the GBM Response Generator[3] released by *Fermi*-GBM team. As mentioned above, we fit the spectrum of each time segment (in 8−200 keV) with three different photon models: an exponential cutoff power law model (COMPT[4]), the sum of two blackbody functions (BB+BB), and a modified blackbody with resonant cyclotron scattering (MBB-RCS[5]).

Based on the C-stat value obtained with each model fit, we employed the Bayesian Information Criterion (BIC; Liddle 2007; Schwarz 1978) to evaluate the improvement of one model compared to the others, as follows:

$$\mathrm{BIC} = \text{C-stat} + m \ln N$$

where m is the number of parameters in the photon model and N is the number of data points. By comparing the BIC values of each of the three photon model fits in pairs, we determined a statistically preferred model that has a significantly

---

[3] `https://fermi.gsfc.nasa.gov/ssc/data/analysis/rmfit/DOCUMENTATION.html`

[4] $f(E) = A \exp[-E(2+\Gamma)/E_{\mathrm{peak}}](E/50\mathrm{keV})^{\Gamma}$

[5] We generated a table model to be used in XSPEC by following the prescription of Yamasaki et al. (2020). The table model covers the energy range from 5 to 300 keV, and the parameter grid of $\mathrm{T_{eff}}$ consists of 79 values between 1 and 40 keV with increments of 0.5 keV (Yamasaki & Gogus, 2024).

lower BIC (ΔBIC > 10, which corresponds to a Bayes factor of $\sim$150, indicating a confidence level >99% for the likelihood ratio; Kass and Raftery 1995). If the difference in BIC values is small, i.e., ΔBIC ≤ 10, then both models are equally preferred.

Following the fits, we also calculated the photon and energy flux of each time segment in the energy range of 8−200 keV based on the fit parameters of each photon model. Note that all errors reported throughout this chapter are at the confidence level of 1σ. We also require model parameters to be well-constrained with their 1σ errors (i.e., model parameter $\pm\, 1\sigma$ errors must be viable values) for the fits to be considered acceptable.

3.2.1 Overlapping Time-Resolved Spectroscopy

Out of the 1343 spectra modeled, we found that 1322 of them (i.e., 98.4% of the sample) are described well with COMPT, meaning that they were deemed preferred based on the BIC values. The thermal models, on the other hand, perform nearly equally in fitting: BB+BB and MBB-RCS models are statistically preferred for 542 (40.4%) and 551 (41%) out of the 1343 time segments, respectively. Here, “preferred” means that the BIC value of a model is either significantly lower than the other two models (ΔBIC > 10, hence the model is the only preferred model) or comparable to the other model(s) (ΔBIC ≤ 10, hence two or all three models are comparably preferred).

As stated before, our aim is to perform a clustering-based time-resolved spectral analysis to clearly reveal spectral evolution throughout short magnetar bursts. Therefore, we identified the significant spectral change points of the bursts using a machine-learning-based clustering algorithm with the results of spectral analysis of overlapping time segments. To do that, we chose the $E_{\rm peak}$ parameter as our reference to determine the spectral change points, since the COMPT model fits more than 98% of the spectra and another parameter in the model (i.e., the power-law index) does not vary significantly within individual events.

For obtaining significant change points in the sequential $E_{\rm peak}$ domain, we employed the k-means clustering method (Pedregosa et al., 2011) using the midpoints of the overlapping time segments and their corresponding $E_{\rm peak}$ values. With the clustering, we were able to combine the consecutive time segments that yielded similar $E_{\rm peak}$ values, considering their errors. Thus, we increased the statistical reliability of the spectral parameters in the second stage of spectroscopy and emphasized the E_{peak} evolution of the burst explicitly by bringing the spectral change points to the fore. In Figure 3.2, we present an example of how overlapping time segments are grouped with k-means clustering for the clustering-based time-resolved spectral analysis, which reveals the spectral evolution throughout the burst, independent of initial time binning. The details of how we applied the k-means clustering to our data can be found in Appendix B.2.

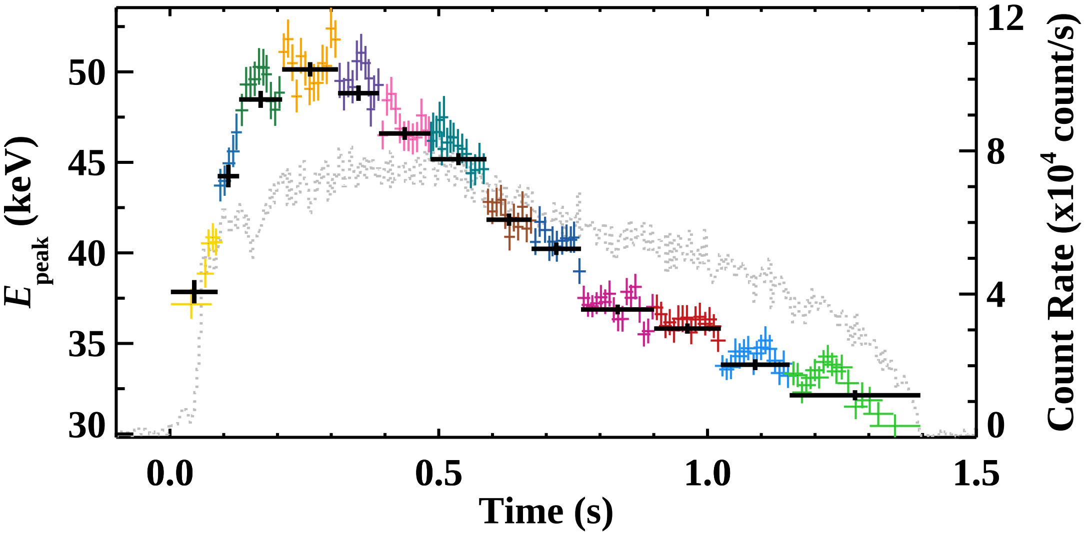

Figure 3.2 Light curve of an SGR J1935+2154 burst detected on 2021 September 10 at 00:45:46.875 UTC as seen with the brightest detector (n8) is shown with gray dotted lines (right axis). Via k-means clustering, 160 overlapping time segments and their corresponding E_{peak} values (the colored data points with asymmetric E_{peak} error bars) yielded 13 spectrally distinctive clusters, each of which is shown with a different color. The black data points show the E_{peak} values with asymmetric error bars that are obtained from the COMPT fit of the data extracted from the time spanned by these 13 clusters in the second stage of spectral analysis.

After the k-means clustering, the grouped time segments still overlap because they are clusters of overlapping time segments (see how the last colored time segment of a cluster overlaps with the first colored time segment of the following cluster in Figure 3.2). Therefore, we defined the end of the cluster time interval to be the time at which half of the counts within the overlapping interval were accumulated (the black data points in Figure 3.2 show the non-overlapping time intervals). After finalizing the cluster time intervals, we checked the total photon counts in each time interval before subjecting them to the second-stage analysis; We found that when there are sharp changes in the spectral parameters, a non-overlapping cluster can only contain 900 (or even less in a few cases) counts. Since we confirmed that this was still statistically sufficient for the second stage of our spectral investigations, we included all spectra of non-overlapping time segments with at least 900 counts in our study. In the few cases where the burst counts remained below this level, we

Table 3.1 List of 51 SGR J1935+2154 Bursts Included in Our Sample

Event Time (UTC)[a]	**Time (*Fermi* MET)**	**Detectors[b]**	**Duration[c]**	**Number of Time Segments**	
(YYMMDD hh:mm:ss)	**(s)**		**(s)**	**Overlapping**	**Nonoverlapping**
160518 09:09:23.800	485255367.890	1,**9**,10	0.161	13	3
160520 05:21:33.483	485414497.487	6,**7**,8	0.108	9	3
160520 21:42:29.322	485473353.323	9,**10**	0.268	7	3
160620 15:16:34.838	488128598.842	6,**7**,8	0.224	21	6
160623 21:20:46.404	488409650.404	6,**7**,9	0.488	32	8
160626 13:54:30.722	488642074.718	**6**,7,9	0.840	90	15
160721 09:36:13.665	490786577.665	6,**7**,8	0.176	17	5
191104 10:44:26.230	594557071.231	0,**1**,2	0.188	9	3
191105 06:11:08.595	594627073.579	3,**4**,8	0.808	29	9
200410 09:43:54.273	608204639.277	**4**	0.168	13	4
200427 18:34:05.700	609705250.708	0,1,**9**	0.404	12	3
200427 18:36:46.007	609705411.006	0,1,**9**	0.363	7	3
200427 19:43:44.537	609709429.537	3,**7**,8	0.436	18	5
200427 20:15:20.582	609711325.581	1,9,**10**	1.287	94	16
200427 21:59:22.527	609717567.528	2,**10**	0.212	7	2
200428 00:24:30.311	609726275.311	4,7,**8**	0.236	13	5
200428 00:41:32.148	609727297.148	3,**6**,7	0.436	5	2
200428 00:44:08.209	609727453.210	3,**6**,7	1.276	28	7
200428 00:46:20.179	609727585.179	**6**,7,9	0.852	19	5
200429 20:47:27.860	609886052.860	4,7,**8**	0.420	17	5
200503 23:25:13.437	610241118.417	**3**,6,7	0.212	6	2
200510 21:51:16.278	610840281.278	**10**,11	0.424	15	4
210129 07:00:00.973	633596405.966	1,2,**5**	0.208	19	6
210129 10:35:39.918	633609344.918	4,**5**	0.308	21	6
210130 17:40:54.743	633721259.652	1,**2**,5	0.256	10	4
210216 22:20:39.572	635206844.573	0,**1**,3	0.344	12	4
210707 00:33:31.632	647310816.633	9,**10**,11	0.144	10	4
210710 20:26:04.407	647641569.407	9,**10**,11	0.220	16	4
210805 00:08:56.006	649814941.006	7,**8**,11	0.448	12	3
210910 00:45:46.874	652927551.875	7,**8**,11	1.396	160	13
210911 05:32:38.611	653031163.611	6,**7**,8	0.308	6	2
210911 13:28:54.950	653059739.951	6,**7**,8	0.180	13	4
210911 15:06:43.187	653065608.188	**6**,7,9	0.404	38	11
210911 15:15:25.373	653066130.373	6,**9**,10	1.176	91	16
210911 15:17:45.288	653066270.288	6,**9**,10	0.944	31	7
210911 17:01:09.675	653072474.675	**9**,10	1.560	84	14
210911 20:22:58.772	653084583.772	9,**10**	1.404	7	2
210912 12:19:20.431	653141965.431	9,**10**	0.492	5	2
210912 20:16:10.382	653170575.381	9,**10**	0.983	26	6
210912 23:19:32.042	653181577.043	9,**10**	0.296	6	2
211008 15:57:46.393	655401471.394	**6**,7,9	0.360	17	5
211224 03:42:34.341	662010159.341	1,3,**5**	1.300	132	16
211229 16:41:26.190	662488891.191	0,**1**,3	0.308	9	3
220111 17:05:55.630	663613560.638	0,1,**3**	0.352	19	5
220112 08:39:25.279	663669570.275	0,**1**,2	1.036	50	10
220112 19:58:04.026	663710289.027	0,1,**3**	0.744	12	3
220114 16:08:43.298	663869328.298	0,**1**,2	0.568	11	3
220115 07:05:44.753	663923149.801	3,**4**,5	0.688	9	2
220115 08:25:56.217	663927961.173	0,**3**,4	0.684	5	2
220115 17:21:59.282	663960124.227	1,2,**5**	0.348	13	4
220116 14:09:38.568	664034983.565	0,**1**,5	0.698	18	6

Notes.

[a] The bursts in 2016, in 2019−2020, and in 2021−2022 are taken from Lin, Göğüş, et al. (2020); Lin, Göğüș, et al. (2020) and L. Lin et al. (2025, in preparation), respectively.

[b] Unblocked NaI detectors used in spectral analysis. The brightest detectors shown in bold are used to determine the start and stop times of time segments for the extraction of spectra.

[c] Bayesian Block Duration. Event times (both UTC and MET) represent the Bayesian Block duration start times of the bursts.

combined the time segments if they were adjacent, and if they were isolated single segments, we combined them with an adjacent segment with a closer E_{peak} value.

In the end, we obtained 287 spectrally distinctive time segments for the clustering-based time-resolved spectral investigations of 51 bursts. In Table 3.1, we list the times of these 51 bursts, along with the detectors used in spectral analysis and event duration, as well as the number of overlapping and non-overlapping time segments.

3.2.2 Clustering-Based Time-Resolved Spectroscopy

We performed a detailed analysis of the 287 spectra accumulated from distinct time segments with the three continuum models (COMPT, BB+BB, and MBB-RCS). Based on these results, we determined the preferred model(s) for each segment using their BIC values. We found that COMPT is a preferred model for 279 spectra (See Table 3.2), out of which COMPT is the only preferred model for 83 spectra, COMPT & BB+BB are equally preferred for 98 spectra, and COMPT & MBB-RCS are equally preferred for 58 spectra. As for the thermal models, the BB+BB model is statistically preferred for 145 (51%) and MBB-RCS model for 98 (34%) out of 286 spectra (one spectrum is excluded due to unacceptable fit statistics; see below for details regarding the goodness-of-fit test). Finally, all three models are equally preferred for 40 spectra (14%). To demonstrate the spectral shapes of these three continuum models, we present an exemplary count spectrum that fits almost equally well with all three models in Appendix B.3 (Figure B.1).

Table 3.2 Number of Nonoverlapping Time Segments per Preferred Photon Model

Preferred Models[a]	**COMPT**	**BB+BB**	**MBB-RCS**	**All**	**Total Number (%)**
COMPT (3)	83	98	58	40	279 (97.6%)
BB+BB (4)	98	7	0		145 (50.7%)
MBB-RCS (2)	58	0	0		98 (34.3%)

Note.

[a] Number of model parameters is indicated in parentheses.

Out of the seven spectra that favor only BB+BB, we found $\Delta\mathrm{BIC} \sim 30 - 40$ for four of them (two segments each from two bursts), meaning that the BB+BB model is definitely preferred over the other two models. Interestingly, the remaining time segments of these two bursts also favor thermal models (i.e., BB+BB and/or MBB-RCS), besides COMPT. In Figure 3.3, we present the spectral evolution of thermal model parameters from one of these two bursts. We also present the time evolution of photon flux distribution for the first seven segments of this event in Appendix B.3 (Figure B.2).

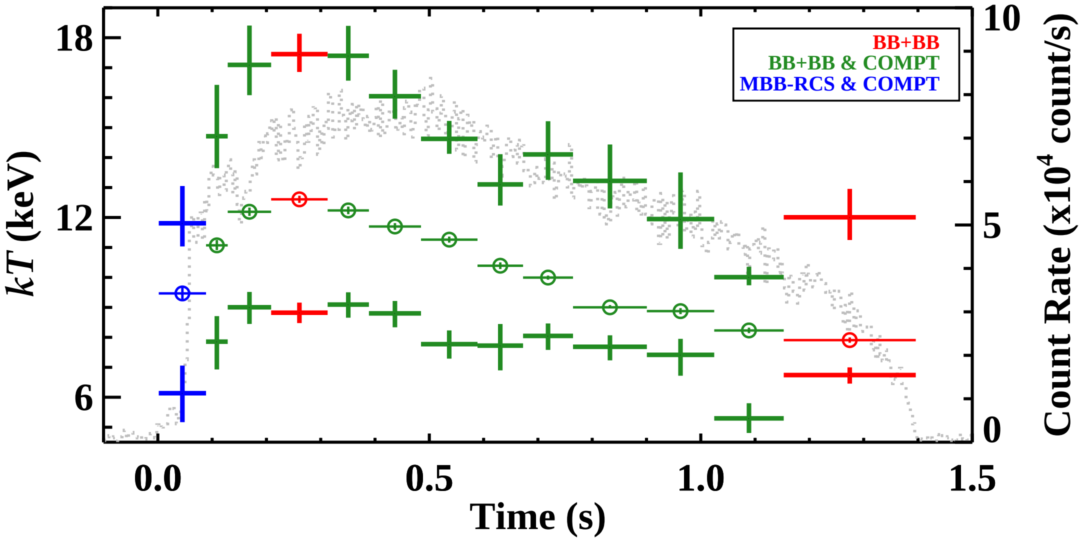

Figure 3.3 Blackbody temperature evolution for a burst, throughout which a thermal model is preferred. The light curve is shown with gray dotted lines (right axis; the same event as Figure 3.2). Thick data points show the $kT_{\rm Low}$ and $kT_{\rm High}$ parameters of BB+BB, while thin data points with circles show the $kT_{\rm M}$ of MBB-RCS. The color code represents the preferred model(s) for each time segment based on the ΔBIC. The ΔBIC between BB+BB and the other two models is only slightly above 10 for the first time segment, which is shown with blue color.

To ensure that these preferred models provide statistically acceptable fits to the spectra, we also evaluated the goodness of fits for the preferred models using C-stat, following Kaastra (2017). In doing so, we used the C-stat values excluding 30−40 keV to avoid the contribution from the iodine K-edge, which could affect the statistics for bright events[6]. To this end, we computed the expected C-stat ($C_{\rm e}$) and its variance ($C_{\rm v}$)[7] based on model predictions and determined whether each model fit remained within the 3σ level[8] of its expected C-stat distribution. We found that for only one spectrum (the second time segment of the burst at 608204639.277 MET) did all three models yield C-stat values with $> 3\sigma$ deviation; this is due to the counts in < 10 keV being lower than what is expected from these three models. Therefore, we excluded this time segment from our analysis and evaluated 286 out of 287 time segments from the 51 bursts in what follows below. Note that the numbers given in Table 3.2 exclude this time segment.

In Figure 3.4 panel (a), we present the scatter plot of the 279 pairs of photon

---

[6] `https://fermi.gsfc.nasa.gov/ssc/data/analysis/GBM_caveats.html`

[7] Using the Python package `https://github.com/abmantz/cstat/blob/python/cashstatistic/cashstatistic.py`

[8] $\sigma = (\text{C-stat} - C_{\rm e})/\sqrt{C_{\rm v}}$

index (Γ) and E_{peak} values of the COMPT model. Note that the plot is color-coded based on the energy flux in 8−200 keV. We find that the distribution of Γ is asymmetric, described best by a Gaussian with an underlying first-order polynomial (see panel (b) of Figure 3.4). Γ values above 0.25 follow a Gaussian with a mean value of 0.65±0.02 and $\sigma = 0.18 \pm 0.02$. However, Γ values below 0.25 form an excess above the Gaussian tail, which can be described with a first-order polynomial of $(7.08 \pm 1.95)\Gamma + (10.13 \pm 1.76)$. It is clear from Figure 3.4 that those Γ values forming the excess are obtained from time segments with the lowest flux in our sample (below 1×10^{-5} erg cm^{-2} s^{-1}). These time segments with low flux values generally correspond to the first or last time segments of the bursts, as expected. On the other hand, time segments with higher flux values yield Γ values mostly larger than 0.25, and those are the values whose distribution is consistent with a Gaussian. It is also important to note that the time segments with the highest flux values (above 4×10^{-5} erg cm^{-2} s^{-1}) yield Γ values in a very narrow range from 0.2 to 0.55.

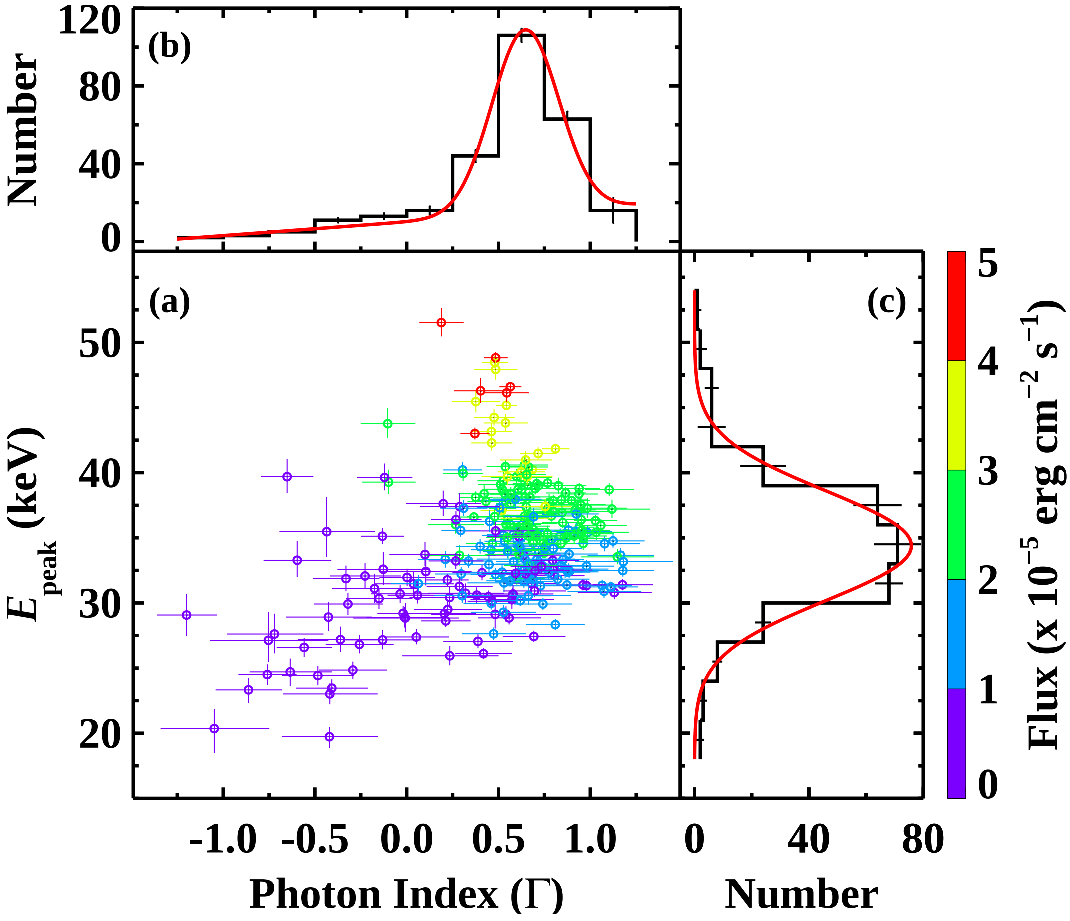

Figure 3.4 (a) The scatter plot of E_{peak} vs. Γ parameters of 279 spectra that can be described well with COMPT. The colors indicate the energy flux values (8−200 keV). (b) The distribution of Γ values with the best-fit model (Linear + Gaussian) curve is shown in red. (c) The distribution of E_{peak} values with the best-fit Gaussian function overlaid in red.

As for the corresponding E_{peak} values, they range from $\sim$20 to $\sim$52 keV, and their distribution follows a Gaussian shape with a mean of 34.39±0.26 keV and a width σ = 4.21±0.20 (see panel (c) of Figure 3.4). Moreover, there appears to be a positive correlation between E_{peak} and flux. To quantify the correlation, we computed Spearman's rank-order correlation coefficients (ρ and chance probability, P) for E_{peak} and flux using a bootstrap method; we generated 10,000 data sets by taking into account the uncertainties of E_{peak} and flux, and calculated the correlation coefficients for each data set. From the distribution of these coefficients, we obtained the mean and 1σ confidence interval of ρ and P. We found $\rho = 0.81 \pm 0.01$ and $P < 10^{-63}$ for E_{peak} and flux, which lends support to the observed positive correlation.

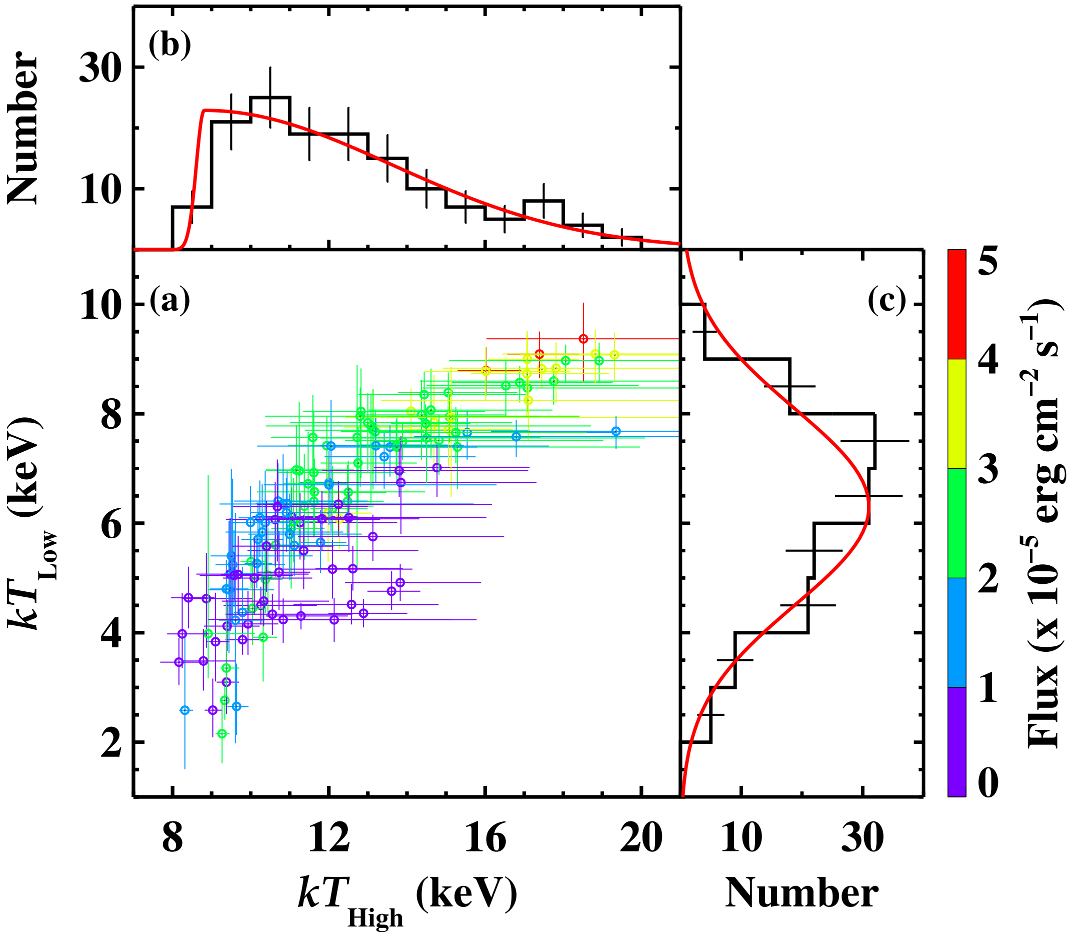

Figure 3.5 (a) The scatter plot of kT_{Low} vs. kT_{High} parameters of 145 spectra that can be described well with BB+BB. The colors indicate the energy flux values. (b) The distribution of kT_{High} with the best-fit model (two-sided Gaussian) curve is shown in red. (c) The distribution of kT_{Low} values with the best-fit Gaussian function overlaid in red.

For the 145 BB+BB-preferred spectra, we present the scatter plot of low BB (kT_{Low}) and high BB (kT_{High}) temperatures in Figure 3.5. It is again color-coded based on the energy flux in the 8−200 keV. We find a positive correlation between the two parameters ($\rho = 0.67 \pm 0.04$ and $P < 10^{-17}$). Overall, lower temperatures are associated with low flux levels (purple and blue data points in panel (a) of Figure 3.5), while higher temperatures correspond to high flux values (red and yellow data points). The intermediate flux values, however, have a much wider BB+BB temperature range. In terms of parameter distributions, we find that a best Gaussian fit to the distribution of $kT_{\rm Low}$ yields a mean of 6.30±0.17 keV with a sigma of 1.80±0.15 (see panel (c) of Figure 3.5). On the other hand, our criterion that the $kT_{\rm High}$ parameter must be larger than the $kT_{\rm Low}$ parameter forces the distribution of $kT_{\rm High}$ to be asymmetrical (see panel (b) of Figure 3.5). Therefore, the best fit to the distribution of $kT_{\rm High}$ results in a two-sided Gaussian fit. The distribution has a mean of 8.81±2.74 keV with $\sigma_{\rm left} = 0.2\pm1.8$ and $\sigma_{\rm right} = 4.83\pm1.4$.

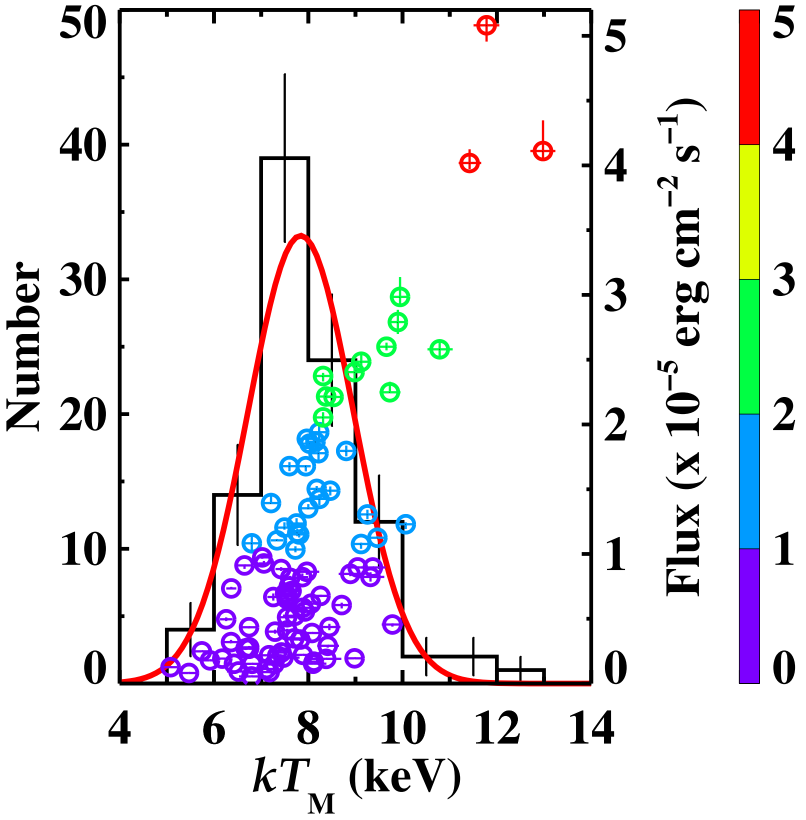

Figure 3.6 The distribution of $kT_{\rm M}$ parameter of 98 spectra that favor MBB-RCS, with the best-fit Gaussian function overlaid in red (left axis). The scatter plot of energy flux vs. $kT_{\rm M}$ is also shown (right axis). The colors indicate the energy flux values.

Finally, for the 98 MBB-RCS-preferred spectra, the distribution of temperature ($kT_{\rm M}$) lies between 5 and 13 keV, which remains in between the $kT_{\rm Low}$ and $kT_{\rm High}$ distributions of the BB+BB model. In Figure 3.6, we present the $kT_{\rm M}$ parameter distribution of the MBB-RCS model. The distribution is described well with the normal distribution, which peaks at 7.84±0.12 keV with $\sigma = 1.12\pm0.1$. As in the BB+BB model, we also observe a positive correlation between energy flux and temperature in this model ($\rho = 0.62 \pm 0.02$ and $P < 10^{-11}$); on average, higher $kT_{\rm M}$ values correspond to higher flux values.

3.3 Discussion

In this study, we applied a novel approach for the first time in magnetar bursts research: a clustering-based time-resolved spectroscopy. We performed highly time-resolved spectral analysis of the brightest SGR J1935+2154 bursts by first dividing them into the sequentially overlapping shortest time intervals to clearly reveal the spectral evolution during the short magnetar bursts. We then identified the significant spectral change points throughout the bursts using the spectral analysis results of these overlapping time segments through a machine-learning-based clustering approach and completed the second round of spectroscopy with the data extracted from the time intervals between these change points. In the end, we obtained 287 nonoverlapping sequential time segments from 51 bursts. Out of 287 spectrally distinguishing time intervals, 207 arise from the brightest half of our burst sample, indicating the existence of a quite significant spectral evolution in the brightest magnetar bursts.

Lin, Göğüş, et al. (2020); Lin, Göğüș, et al. (2020) studied time-integrated spectral properties of 275 SGR J1935+2154 bursts between 2014 and 2020 observed with *Fermi*-GBM. They found that ∼62% and ∼38% could be described well with the BB+BB and COMPT models, respectively. In contrast, our clustering-based time-resolved spectral analysis revealed that only ∼51% can be fit with BB+BB, while nearly all time segments (∼98%) of the brightest bursts could be represented with COMPT. Note the fact that our burst sample selected from these 275 bursts is comprised of the brightest ones, based on our criterion as explained in Section 3.1; therefore, it would be a fairer comparison with our results if we exclude dim bursts from their statistics. In that case, the accepted fit percentages for their samples (178 bursts) increase to ∼96% and ∼58% with the BB+BB and COMPT models, respectively, which still are quite different from our results found here. Besides the difference between time-integrated and time-resolved analysis, such a difference in model preferences of the two studies might arise from the fact that our sample also includes SGR J1935+2154 bursts from the 2021 to 2022 active episodes. However, our statistics remained nearly the same when we excluded these bursts and evaluated only the bursts before 2021, and even when we look at the percentages of statistically acceptable fits (instead of BIC-based preferences), the COMPT model describes them better than BB+BB does. We thus conclude that the time-resolved spectral results are different from those of time-integrated spectral investigations. This is not surprising, given that we observe significant spectral variation throughout each burst, and superposition of spectra with varying $E_{\rm peak}$ values in COMPT could mimic the spectral energy distribution of BB+BB or results in the distribution that deviates from a single-component COMPT model. Besides, the time-integrated spectra naturally have more counts even at higher energies, with which the two-component model parameters are better determined.

3.3.1 Spectral Parameters-Flux-Area Correlations

As for the model parameters of the time-integrated spectroscopy of SGR J1935+2154 bursts between 2014−2016, those that fit well with the COMPT model have $E_{\rm peak}$ values ranging between ∼25 and 40 keV with a Gaussian mean of 30.4±0.2 keV (Lin, Göğüş, et al., 2020). The later 2019−2020 bursts have a wider range of $E_{\rm peak}$ (∼10−40 keV) with a slightly lower mean of 26.4±0.6 keV (Lin, Göğüș, et al., 2020). In comparison, our clustering-based time-resolved spectroscopy yields a slightly higher energy range of ∼20−52 keV and a higher mean $E_{\rm peak}$ of 34.4±0.3 keV. We again note here that our burst sample includes bursts that were detected in the 2021 and 2022 active episodes and met our brightness criterion; when we compare only the bright events between 2016 and 2020, the time-resolved $E_{\rm peak}$ in our sample is still harder.

Previously, time-integrated spectral analysis of SGR J1935+2154 bursts and other prolific magnetar bursts (SGR J1550−5418) showed that $E_{\rm peak}$ is correlated with the energy flux or fluence described by a power law or a broken power law (Lin, Göğüş, et al., 2020; Lin, Göğüș, et al., 2020; van der Horst et al., 2012). We present in Figure 3.7 (left panel), the $E_{\rm peak}$ versus flux plot for our time-resolved results; the correlation was revealed more clearly as a result of our time-resolved spectroscopy (Spearman's rank correlation coefficient, $\rho = 0.81 \pm 0.01$, $P < 10^{-63}$). To better quantify the relation between $E_{\rm peak}$ and flux, we fit the trend as follows: Since flux errors were small ($\Delta F/F \lesssim 0.015$), we grouped the data in the flux domain such that each group would include 20 data points. For each group, we computed the weighted mean flux and $E_{\rm peak}$, as well as 1σ uncertainty of $E_{\rm peak}$. Modeling the grouped trend with a single power law model (PL) yields an unacceptable fit (χ^2/dof = 117.4/12). A fit with a broken power law model (BPL), on the other hand, results in statistically acceptable representation (χ^2/dof = 15.7/10), yielding a break at the flux of (2.00±0.05) $\times 10^{-5}$ erg cm^{-2} s^{-1}, and positive indices of 0.08±0.01 and 0.37±0.03 before and after the break, respectively (see Figure 3.7, left panel).

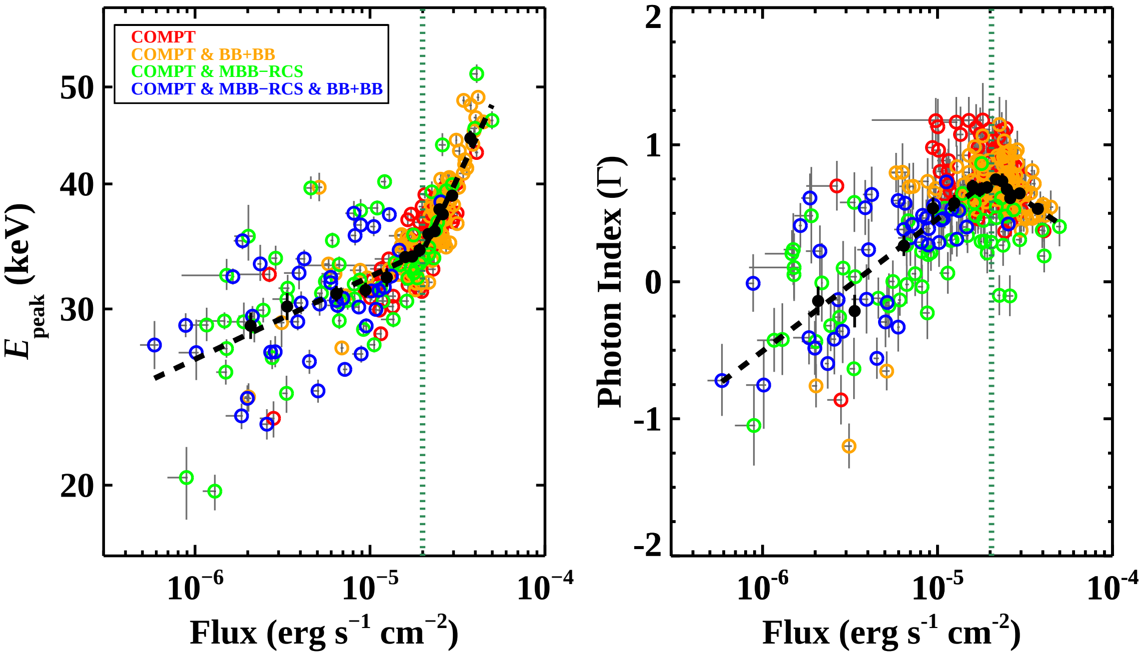

Figure 3.7 The scatter plot of E_{peak} vs. flux **(left panel)** and photon index vs. flux **(right panel)** of the COMPT model fits. The color code shows the preferred photon model(s) based on BIC values. The black dots represent the weighted means of consecutive groups, each with 20 data points. The black dashed lines show the BPL fits to the relation between the weighted means of E_{peak} and flux, and between the weighted means of photon index and flux, respectively. The vertical dotted lines in both panels show the flux breaks, which are consistent with each other within their errors.

On the other hand, we found that the range of the COMPT photon index (Γ) parameter of our time-resolved investigation is consistent with the time-integrated spectroscopy although their distributions are quite different. The Γ distribution of time-integrated spectral analysis runs from −1.5 to 1 and follows a Gaussian with a mean of ∼0 (Lin, Göğüş, et al., 2020; Lin, Göğüș, et al., 2020). In the case of our time-resolved spectroscopy, the distribution has a tail, best described with a Gaussian with an underlying first-order polynomial. The positive Γ values above 0.25 are distributed like a Gaussian with a mean at 0.65±0.02, while Γ values below 0.25 form an excess above the Gaussian tail. We found that these indices ($\Gamma < 0.25$) were obtained from the spectra with the lowest flux values in our sample ($< 1 \times 10^{-5}$ erg cm^{-2} s^{-1}). Moreover, the spectra with the highest flux values in our sample ($> 4 \times 10^{-5}$ erg cm^{-2} s^{-1}) yield Γ values in a very narrow range with a weighted mean of 0.47±0.03. There exists a positive correlation between Γ and flux up to a certain flux level that coincides with the flux break of E_{peak} versus flux (see the right panel of Figure 3.7). The index and flux are anti-correlated after that point. The change in trend between index and flux is also indicated in Figure 3.4: the photon index increases with increasing flux up to about 2×10^{-5} erg cm^{-2} s^{-1} (blue and purple data points in the panel (a) of Figure 3.4). Then, the index starts to decrease with increasing flux. In modeling this trend, we followed a similar approach as in the case of $E_{\rm peak}$ versus flux: We obtained weighted mean Γ values and their 1σ uncertainties for the groups of 20 flux values and used a broken log-linear function to fit, yielding $\chi^2/\mathrm{dof} = 10.1/10$. We found the break at the flux of $(2.04\pm0.09)\times10^{-5}$ erg cm^{-2} s^{-1}, which is consistent with the $E_{\rm peak}$ versus flux case. The slope of 0.97 ± 0.09 before the break changes to -0.86 ± 0.17 afterward (see the right panel of Figure 3.7).

Younes et al. (2014) performed time-resolved spectral investigations of bursts from another prolific magnetar, SGR J1550$-$5418, also observed with *Fermi*-GBM. They also found that the $E_{\rm peak}$ versus flux relation is described better with a BPL rather than a single PL. This break point is at the flux of $\sim 1 \times 10^{-5}$ erg cm^{-2} s^{-1}, which is about half the break value in flux that we found for SGR J1935+2154. Unlike our findings, the $E_{\rm peak}$ versus flux correlation of SGR J1550$-$5418 is negative at low flux values, while it is positive after the flux break. Moreover, Γ remains constant at ~ -0.8 up to the flux break, then follows the same positive trend as seen between $E_{\rm peak}$ and flux. Similar dual relation between the $E_{\rm peak}$ and flux with a break at the flux of $\sim 1 \times 10^{-5}$ erg cm^{-2} s^{-1} was also reported in the time-resolved spectroscopy of five bright bursts from yet another magnetar, SGR J0501+4516 (Lin et al., 2011).

For the BB+BB model, earlier time-integrated spectral studies of SGR J1935+2154 bursts yielded parameters of $\sim$2$-$8 keV for $kT_{\rm Low}$ with a mean of 4.5 keV, and $\sim$8$-$20 keV for $kT_{\rm High}$ with a mean of 11 keV (Lin, Göğüş, et al., 2020; Lin, Göğüș, et al., 2020). Our clustering-based time-resolved spectroscopy using the BB+BB model results in similar parameter range and distribution for $kT_{\rm High}$. However, our $kT_{\rm Low}$ parameter reaches up to 10 keV with a larger mean of 6.3 ± 0.2 keV. Moreover, unlike the time-integrated spectral analysis, our study reveals a positive correlation between $kT_{\rm Low}$ and $kT_{\rm High}$ ($\rho = 0.67 \pm 0.04$, $P < 10^{-17}$; see panel (a) of Figure 3.5).

Based on the BB+BB parameters, we also calculated the size of blackbody emitting areas as $R^2 = (Fd^2)/(\sigma T^4)$ in km^2 where F is the flux, d is the distance to the source (here we use a distance of 9 kpc, consistent with Lin, Göğüş, et al. 2020; Lin, Göğüș, et al. 2020), σ is the Stefan-Boltzmann constant, and T is the temperature in Kelvin. Our study revealed that the relation between T and R^2 varies with the burst flux, similar to the findings of time-resolved spectral analysis of SGR J1550$-$5418 bursts

(Younes et al., 2014). Therefore, following Younes et al. (2014), we divided our 145 spectra that favors BB+BB model into four groups based on energy flux (in erg cm^{-2} s^{-1}): $F < 10^{-5.5}$, $10^{-5.5} < F < 10^{-5.0}$, $10^{-5.0} < F < 10^{-4.5}$, and $F > 10^{-4.5}$. In the left panel of Figure 3.8, we present the plot of R^2 versus kT for the abovementioned flux ranges. We found that the best fit for the R^2 versus kT relation of the three highest-flux data groups is the BPL model. However, for the lowest-flux group, both PL and BPL provide statistically acceptable fits. Despite the difference, we observe that the overall trends in all four groups are the same: The negative correlation (slope) between R^2 and kT becomes steeper after the break of the BPLs. We summarize our flux-dependent R^2 versus kT fit results in Table 3.3. Note that these fit results are obtained with the data from all of the spectra that favor BB+BB, not with the weighted means of the data (which we show in Figure 3.8 only for display purposes).

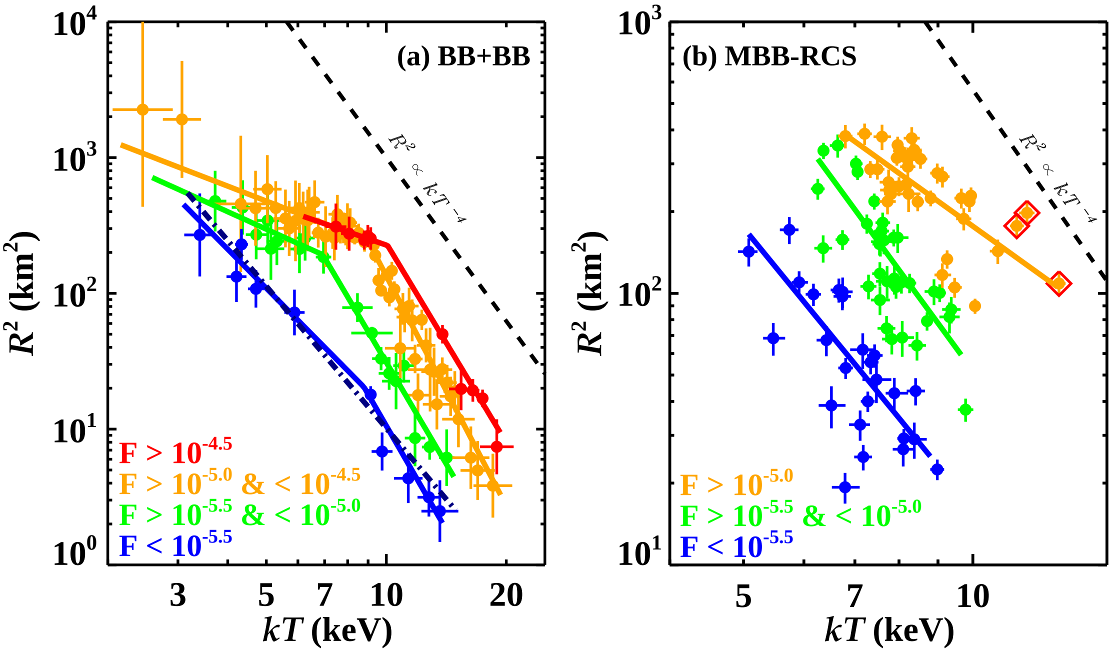

Figure 3.8 [**Left**] Flux color-coded plot of R^2 vs. kT for 145 BB+BB spectra. Each data point represents the weighted means of R^2 and kT of three time segments for display purposes only. Solid lines show BPL fits. The dark blue dashed-dotted line indicates PL fit to the lowest-flux group. The lowest-flux group is fitted almost equally well with either a single PL or BPL. The black dashed line indicates $R^2 \propto kT^{-4}$. [**Right**] Flux color-coded scatter plot of R^2 vs. kT for 98 spectra favoring MBB-RCS. Solid lines represent PL fits. The dashed line indicates $R^2 \propto kT^{-4}$. Note that we combined the data points of the two highest-flux groups for MBB-RCS, since only three spectra in the highest-flux group ($F > 10^{-4.5}$ erg cm^{-2} s^{-1}) favor the MBB-RCS model; these three are shown with red diamonds.

We observe that the kT ranges of SGR J1935+2154 and SGR J1550−5418 bursts are similar while the values of R^2 for SGR J1935+2154 bursts do not go down below 1 km^2 unlike those of the SGR J1550−5418 bursts. Still, the relation between

R^2 and kT has the same trend for both sources: R^2 decreases more slowly for kT_{Low} compared to kT_{High} across all flux ranges. We found that the slope between R^2 and kT_{Low} (α-kT_{Low}) and the slope between R^2 and kT_{High} (α-kT_{High}) for all flux groups in both studies are consistent with one another within at most 3σ errors. Also, kT_{break} values are consistent with one another within errors (∼7−9 keV for SGR J1550−5418; Younes et al. 2014). Moreover, we observed a similar relation between R^2 and kT_{Low} : α-kT_{Low} becomes steeper as flux decreases. However, our investigations do not yield a decreasing trend in α-kT_{High} with decreasing flux. Furthermore, similar to SGR J1550−5418 bursts, a single PL model yields a statistically acceptable R^2 and kT fit in the lowest-flux group.

Table 3.3 R^2 vs. kT Fit Parameters (PL Index α and Break Energy) for Various Flux Ranges of BB+BB and MBB-RCS Models as Shown in Figure 3.8

	BB+BB			**MBB-RCS**
Flux Range (erg cm^{-2} s^{-1})	α-kT_{Low}	α-kT_{High}	kT_{break} (keV)	α-kT_{M}
$F > 10^{-4.5}$	-1.02 ± 1.64	-4.88 ± 0.79	10.08 ± 1.12	-2.01 ± 0.10^{a}
$10^{-5.0} < F < 10^{-4.5}$	-1.14 ± 0.35	-5.62 ± 0.24	8.98 ± 1.02	-2.01 ± 0.10^{a}
$10^{-5.5} < F < 10^{-5.0}$	-1.36 ± 0.81	-4.99 ± 0.47	6.96 ± 1.09	-3.83 ± 0.15
$F < 10^{-5.5}$	-3.01 ± 0.64 -3.47 ± 0.23^{b}	-5.05 ± 0.88 ...	8.79 ± 1.24 ...	-3.43 ± 0.16

Notes.

[a] Slopes of the data points from the highest two flux groups for the MBB-RCS model are the same since they are combined due to the deficiency of time segments (only three) that favor MBB-RCS in the highest flux regime.

[b] A single PL fit to the data.

Finally, for the other thermal model, namely the modified blackbody whose emission undergoes resonant cyclotron scattering (MBB-RCS), we observe a correlation between temperature and flux (see Figure 3.6, $\rho = 0.62 \pm 0.02$ and $P < 10^{-11}$). Also, for the 98 MBB-RCS-preferred spectra, we calculated the corresponding emitting region (R^2) based on their temperature (kT_{M}). In the right panel of Figure 3.8, we present the scatter plot of R^2 versus kT_{M} with color coding based on the same flux ranges used for BB+BB − except that we combined the highest two flux groups for the MBB-RCS model, due to the deficiency of time segments (only three) in the highest-flux regime described well by MBB-RCS. We find that, for R^2 versus kT_{M}, the best fit across all flux ranges is a PL, which is also presented in Table 3.3. We also find that PL indices (α-kT_{M}) for the lowest two flux regimes are consistent with −4 (i.e., as expected from $F \propto \sigma T^4$). More importantly, the α-kT_{M} obtained from the highest-flux spectra ($F > 10^{-5}$ erg cm^{-2} s^{-1}, corresponding to an isotropic luminosity of 10^{41} erg s^{-1}) is significantly different, -2.01 ± 0.10, than that of the lower-flux spectra.

3.3.2 Interpretative Elements

We now elaborate on the interpretation of some of our results. Large Thomson opacities are expected for magnetars in outburst, quickly discernible using nonmagnetic estimates that were identified by Baring and Harding (2007). Let us first set $\mathcal{E}_e \gtrsim L_\gamma/(4\pi R^2 c)$ as the representative kinetic energy density in radiating electrons. Then, if they possess a typical Lorentz factor $\langle\gamma_e\rangle \sim 1$, one quickly arrives at an electron number density $n_e \sim \mathcal{E}_e/(m_e c^2)$, such that the nonmagnetic Thomson optical depth is $\tau_t = n_e \sigma_T R \gtrsim L_\gamma \sigma_T/(4\pi R m_e c^3)$; this is the familiar compactness parameter. For $R \sim 10^7$cm, this yields $\tau_t \sim 10^4$ (i.e., $n_e \gtrsim 10^{21}\text{cm}^{-3}$) for SGR bursts of typical isotropic luminosities $L_\gamma \sim 10^{40} erg\, s^{-1}$, indicating optically thick, super-Eddington conditions (e.g. C. Thompson & Duncan, 1996) that drive plasma flow along the field lines.

In Figure 3.8 (left), we observe a significant deviation from the Stefan-Boltzmann (S-B) law for an isotropic radiation field ($R^2 \propto kT^{-4}$): We find $R^2 \propto kT^{-\alpha}$, where $\alpha \sim 1 - 1.4$ for $kT \lesssim 7-10$ keV above the flux level of $\sim 10^{-5.5}$ erg cm^{-2} s^{-1}. Note that this flux corresponds to an isotropic luminosity of 3×10^{40} erg s^{-1} at a source distance of 9 kpc. The resulting broken power-law $R^2 - kT$ correlations can be interpreted as a signature of the spatial extension of the active emission region, which can be presumed to be a broad, flaring flux tube. If this tube has a transverse dimension of $R_t \sim 2-10$km for its cross section at the highest altitudes, one can infer a tube length of $R_l \sim 4R^2/R_t \sim 100-500$km for the largest R^2 values. The highly optically thick gas in the emission region will naturally cool adiabatically when moving between smaller, hotter regions near the flux tube footpoints at the stellar surface and the high-altitude, large-area regions near the equatorial tube apex. This yields the spectral extension we see. If the radiating gas is locally quasi-thermal, then near the footpoints the magnetic field is high, and photospheric/atmospheric simulations (see Fig. 2 of Hu, Baring, Barchas, & Younes, 2022) of radiative transfer in this sub-cyclotronic frequency domain ($\omega \ll \omega_B = eB/\hbar c$) indicate that the radiation is quasi-isotropic. In contrast, since the magnetic field is much lower (likely 3-4 orders of magnitude) near the tube apex, the Compton scattering radiative transfer in the local region samples the cyclotronic domain where $\omega \sim \omega_B$. This domain evinces significantly anisotropic emergent radiation fields (see the right column of Fig. 2 of Hu et al., 2022), with a decrement of intensity over a wide range of directions that are oriented closer to the outer surface of the magnetic flux tube/photosphere; this tube surface is aligned with the local field direction that guides plasma motion and associated adiabatic cooling. Such a decrement alters the S-B law from its isotropic "$R^2(kT)^4 =$ constant" form, and lowers the perceived area in lower-kT regions at higher altitudes[9]. The reduced values of $R^2(kT)^4$ naturally generate the breaks apparent in Figure 3.8. In particular, the actual flux tube areas would rise above those the S-B estimate obtains. Concomitantly, this decrement yields the break in the flux-$E_{\rm peak}$ correlation depicted in Figure 3.7 (left).

The extended spatial emission zone scenario suggests that a multi-blackbody fit would be preferable to just a BB+BB one. This may be the reason why the MBB-RCS model provides a good spectral fit for a significant portion of the sample studied here, in which for the first time the MBB-RCS model has been applied to a substantial sample size. Clearly, the scattering component of the MBB-RCS picture applies outside the highly optically thick primary burst emission zone. If the plasma density becomes high enough, as may be more likely for the highly energetic events ($L \gtrsim 10^{41}$ erg s^{-1}), multiple scatterings of photons by the magnetospheric charges would arise, and this likely would harden the emerging spectrum. The required plasma densities would be considerably higher than those needed in resonant inverse Compton emission models (Baring & Harding, 2007; Fernández & Thompson, 2007; Wadiasingh, Baring, Gonthier, & Harding, 2018) of the persistent hard X-ray tail emission of luminosities $L \sim 10^{35}$erg s^{-1} (den Hartog et al., 2008; Götz, Mereghetti, Tiengo, & Esposito, 2006; Kuiper, Hermsen, & Mendez, 2004) from various magnetars. In such domains, the MBB-RCS model would need to be expanded (Yamasaki et al., 2020).

---

[9] As a side effect, depending on the magnetar's spin phase, the star itself may obscure a segment of the plasma tube (in particular, the footpoint where radiation becomes isotropic) even during the burst. This could introduce additional anisotropy to the emerging radiation and perceived surface area.

4. CONCLUDING REMARKS & FUTURE PROSPECTS

In this study, we aimed to gain a deeper understanding of the underlying physical mechanisms responsible for the emission of high-energy short magnetar bursts. First, we focused on the triggering mechanism of short magnetar burst clusters as seen in many magnetar observations. We took a step toward a firmer model of the mechanism driving magnetar activity, focusing on how different regions of a highly stressed crust may communicate with one another to produce clusters of failure events. The model remains qualitative in nature, with some details of the physics necessarily glossed over in the use of cells and interactions between them. However, regardless of the specifics of our model, our study suggests that any viable mechanism for producing both single bursts and burst clusters must allow for local regions of the crust to be semiautonomous most of the time − resulting in localized failures and single bursts − but to interact with other parts of the crust under certain conditions, thus driving the more energetic burst cluster events. Here, we modeled clustering as being related to direct communication between nearby parts of the crust. Other, potentially more complicated, possibilities might be interaction via the corona (Younes et al., 2022) or the core (C. Thompson, Yang, & Ortiz, 2017). Some logical next steps for our work would be to try to put the cell interactions on a sounder theoretical footing through first-principles simulations of crustal failure in a strong magnetic field, as well as detailed consideration of the coronal dynamics, including reconnection. Nonetheless, the broad agreement between the model and observations so far suggests that this is a good foundation on which to build.

In some magnetars, the emission of energetic burst(s) also marks the onset of magnetar outbursts, which are the enhanced persistent X-ray emission episodes lasting from weeks to years. Coti Zelati et al. (2018) reported that young magnetars are more likely to exhibit energetic outbursts than older ones. They attributed this behavior to magnetic field decay, which limits the available energy budget as a magnetar ages. Similarly, when looking at typical short-burst emission, magnetars with low characteristic ages are burst prolific (see e.g., Lin, Göğüş, et al., 2020; van der Horst et al., 2012) and often exhibit clusters of bursts with high energies (Kaneko et al., 2021, 2010). In contrast, older magnetars emit few bursts with lower energies. This relation can help us understand the evolving stress pattern in a magnetar's crust. It may be interpreted as a result of reducing high-stress volume of the crust in an aging magnetar; previous giant flares cause relaxation of large regions of its crust and inhibit burst clustering, while the reducing burst energy reflects the progressively shallower region of the crust where Hall drift can build stresses effectively as the field decays through the range $\sim 10^{12} - 10^{13}\,\mathrm{G}$.

The motivation of our study was to investigate highly stressed young magnetars (whose ages are at most a few kiloyears) in their burst-active states. Therefore, we were interested in the case when high stresses can develop and be released through plastic flow, and this process requires ohmic decay to be subdominant. Given the high temperatures of typical young magnetars, this corresponds to field strengths of the order $10^{14}\,\mathrm{G}$ (Cumming et al., 2004), but ohmic decay dominates for weaker fields. Therefore, we neglected the effect of ohmic decay in our model for simplicity. For a more complete long-term evolution of short magnetar bursts, we plan to explore the implications of the interplay of Hall drift and ohmic decay for our burst model in a follow-up study (Keskin et al., in preparation).

In this study, we also examined how the "triggered" system generates bursts and their evolution in the magnetosphere via time-resolved spectroscopic studies. We found a quite significant spectral evolution in the brightest short bursts of magnetar SGR J1935+2154, and our two-step approach in spectroscopy enabled us to better determine the evolution. Thanks to this innovative approach, we were able to perform a detailed analysis of the spectra accumulated from spectrally distinctive time segments of bursts with the three continuum models (COMPT, BB+BB, and MBB-RCS) and uncover more dominant underlying physical mechanisms. In this context, we discussed the physical implications of our results in Section 3.3.2.

Accordingly, strong motivations exist for a future detailed study accounting for the altitudinal dependence of the anisotropy of the flux tube radiation field, in combination with RCS modeling in neighboring magnetospheric regions. The RCS process would have to address both single and multiple scattering domains. This level of sophistication is desirable for more precisely interpreting area-color ($R^2 - kT$) correlations at different luminosity levels. In particular, if the energies $kT \sim 7 - 10\,\mathrm{keV}$ of the breaks (obtained from the results of BB+BB model, see Figure 3.8) are interpreted as a loose measure of the $\hbar\omega_B$ value (when the anisotropy becomes substantial) somewhat near the tube apex, it may prove possible to constrain the active flux tube dimensions and magnetospheric locale using the area-color correlations. Thus, our results not only encourage further employment of the MBB-RCS physical model in diverse burst samples from various sources but also highlight the need for more comprehensive modeling approaches in understanding the behavior of highly energetic magnetar flares.

BIBLIOGRAPHY

Ascenzi, S., Viganò, D., Dehman, C., Pons, J. A., Rea, N., & Perna, R. (2024, September). 3D code for MAgneto-Thermal evolution in Isolated Neutron Stars, MATINS: thermal evolution and light curves. *Monthly Notices of the Royal Astronomical Society*, *533*(1), 201-224. doi: 10.1093/mnras/stae1749

Baring, M. G., & Harding, A. K. (2007, April). Resonant Compton upscattering in anomalous X-ray pulsars. *Astrophysics and Space Science*, *308*, 109-118. doi: 10.1007/s10509-007-9326-x

Beloborodov, A. M. (2009, September). Untwisting Magnetospheres of Neutron Stars. *Astrophysical Journal*, *703*(1), 1044-1060. doi: 10.1088/0004-637X/703/1/1044

Beloborodov, A. M. (2013, January). On the Mechanism of Hard X-Ray Emission from Magnetars. *Astrophysical Journal*, *762*(1), 13. doi: 10.1088/0004-637X/762/1/13

Bochenek, C. D., Ravi, V., Belov, K. V., Hallinan, G., Kocz, J., Kulkarni, S. R., & McKenna, D. L. (2020, November). A fast radio burst associated with a Galactic magnetar. *Nature*, *587*(7832), 59-62. doi: 10.1038/s41586-020-2872-x

Cash, W. (1979, March). Parameter estimation in astronomy through application of the likelihood ratio. *Astrophysical Journal*, *228*, 939-947. doi: 10.1086/156922

Chen, K., & Ruderman, M. (1993, January). Pulsar Death Lines and Death Valley. *Astrophysical Journal*, *402*, 264. doi: 10.1086/172129

Cheng, B., Epstein, R. I., Guyer, R. A., & Young, A. C. (1996, August). Earthquake-like behaviour of soft γ-ray repeaters. *Nature*, *382*(6591), 518-520. doi: 10.1038/382518a0

CHIME/FRB Collaboration, Andersen, B. C., Bandura, K. M., Bhardwaj, M., Bij, A., Boyce, M. M., … Zwaniga, A. V. (2020, November). A bright millisecond-duration radio burst from a Galactic magnetar. *Nature*, *587*(7832), 54-58. doi: 10.1038/s41586-020-2863-y

Chugunov, A. I., & Horowitz, C. J. (2010, September). Breaking stress of neutron star crust. *Monthly Notices of the Royal Astronomical Society*, *407*(1), L54-L58. doi: 10.1111/j.1745-3933.2010.00903.x

Collazzi, A. C., Kouveliotou, C., van der Horst, A. J., Younes, G. A., Kaneko, Y., Göğüş, E., … Wijers, R. A. M. J. (2015, May). The Five Year Fermi/GBM Magnetar Burst Catalog. *Astrophysical Journal, Supplement*, *218*(1), 11. doi: 10.1088/0067-0049/218/1/11

Coti Zelati, F., Rea, N., Pons, J. A., Campana, S., & Esposito, P. (2018, February). Systematic study of magnetar outbursts. *Monthly Notices of the Royal Astronomical Society*, *474*(1), 961-1017. doi: 10.1093/mnras/stx2679

Cumming, A., Arras, P., & Zweibel, E. (2004, July). Magnetic Field Evolution in Neutron Star Crusts Due to the Hall Effect and Ohmic Decay. *Astrophysical Journal*, *609*(2), 999-1017. doi: 10.1086/421324

De Grandis, D., Turolla, R., Wood, T. S., Zane, S., Taverna, R., & Gourgouliatos, K. N. (2020, November). Three-dimensional Modeling of the Magnetothermal

Evolution of Neutron Stars: Method and Test Cases. *Astrophysical Journal*, *903*(1), 40. doi: 10.3847/1538-4357/abb6f9

Dehman, C., Viganò, D., Ascenzi, S., Pons, J. A., & Rea, N. (2023, August). 3D evolution of neutron star magnetic fields from a realistic core-collapse turbulent topology. *Monthly Notices of the Royal Astronomical Society*, *523*(4), 5198-5206. doi: 10.1093/mnras/stad1773

Dehman, C., Viganò, D., Rea, N., Pons, J. A., Perna, R., & Garcia-Garcia, A. (2020, October). On the Rate of Crustal Failures in Young Magnetars. *Astrophysical Journal, Letters*, *902*(2), L32. doi: 10.3847/2041-8213/abbda9

den Hartog, P. R., Kuiper, L., Hermsen, W., Kaspi, V. M., Dib, R., Knödlseder, J., & Gavriil, F. P. (2008, October). Detailed high-energy characteristics of AXP 4U 0142+61. Multi-year observations with INTEGRAL, RXTE, XMM-Newton, and ASCA. *Astronomy and Astrophysics*, *489*, 245-261. doi: 10.1051/0004-6361:200809390

Duncan, R. C., & Thompson, C. (1992, June). Formation of Very Strongly Magnetized Neutron Stars: Implications for Gamma-Ray Bursts. *Astrophysical Journal, Letters*, *392*, L9. doi: 10.1086/186413

Fernández, R., & Thompson, C. (2007, May). Resonant Cyclotron Scattering in Three Dimensions and the Quiescent Nonthermal X-ray Emission of Magnetars. *Astrophysical Journal*, *660*(1), 615-640. doi: 10.1086/511810

Goldreich, P., & Reisenegger, A. (1992, August). Magnetic Field Decay in Isolated Neutron Stars. *Astrophysical Journal*, *395*, 250. doi: 10.1086/171646

Götz, D., Mereghetti, S., Tiengo, A., & Esposito, P. (2006, April). Magnetars as persistent hard X-ray sources: INTEGRAL discovery of a hard tail in SGR 1900+14. *Astronomy and Astrophysics*, *449*, L31-L34. doi: 10.1051/0004-6361:20064870

Gourgouliatos, K. N. (2023, January). Magnetic Field Evolution in the Crust of Neutron Stars: Crust Failure and Plastic Flow. In E. Troja & M. G. Baring (Eds.), *Neutron star astrophysics at the crossroads: Magnetars and the multimessenger revolution* (Vol. 363, p. 162-172). doi: 10.1017/S1743921322000485

Gourgouliatos, K. N., De Grandis, D., & Igoshev, A. (2022, January). Magnetic Field Evolution in Neutron Star Crusts: Beyond the Hall Effect. *Symmetry*, *14*(1), 130. doi: 10.3390/sym14010130

Gourgouliatos, K. N., & Lander, S. K. (2021, September). Axisymmetric magneto-plastic evolution of neutron-star crusts. *Monthly Notices of the Royal Astronomical Society*, *506*(3), 3578-3587. doi: 10.1093/mnras/stab1869

Gourgouliatos, K. N., Wood, T. S., & Hollerbach, R. (2016, April). Magnetic field evolution in magnetar crusts through three-dimensional simulations. *Proceedings of the National Academy of Science*, *113*(15), 3944-3949. doi: 10.1073/pnas.1522363113

Göğüş , E., Woods, P. M., Kouveliotou, C., van Paradijs, J., Briggs, M. S., Duncan, R. C., & Thompson, C. (1999, December). Statistical Properties of SGR 1900+14 Bursts. *Astrophysical Journal, Letters*, *526*(2), L93-L96. doi: 10.1086/312380

Göğüş, E., Kouveliotou, C., Woods, P. M., Thompson, C., Duncan, R. C., & Briggs, M. S. (2001, September). Temporal and Spectral Characteristics of Short Bursts from the Soft Gamma Repeaters 1806-20 and 1900+14. *Astrophysical Journal*, *558*(1), 228-236. doi: 10.1086/322463

Göğüş, E., Woods, P. M., Kouveliotou, C., van Paradijs, J., Briggs, M. S., Duncan, R. C., & Thompson, C. (2000, April). Statistical Properties of SGR 1806-20 Bursts. *Astrophysical Journal, Letters*, *532*(2), L121-L124. doi: 10.1086/312583

Hu, K., Baring, M. G., Barchas, J. A., & Younes, G. (2022, March). Intensity and Polarization Characteristics of Extended Neutron Star Surface Regions. *Astrophysical Journal*, *928*(1), 82. doi: 10.3847/1538-4357/ac4ae8

Hurley, K., Cline, T., Mazets, E., Barthelmy, S., Butterworth, P., Marshall, F., … Trombka, J. (1999, January). A giant periodic flare from the soft γ-ray repeater SGR1900+14. *Nature*, *397*(6714), 41-43. doi: 10.1038/16199

Ibrahim, A. I., Strohmayer, T. E., Woods, P. M., Kouveliotou, C., Thompson, C., Duncan, R. C., … Finger, M. (2001, September). An Unusual Burst from Soft Gamma Repeater SGR 1900+14: Comparisons with Giant Flares and Implications for the Magnetar Model. *Astrophysical Journal*, *558*(1), 237-252. doi: 10.1086/322248

Igoshev, A. P., Gourgouliatos, K. N., Hollerbach, R., & Wood, T. S. (2021, March). 3D Magnetothermal Simulations of Tangled Crustal Magnetic Field in Central Compact Objects. *Astrophysical Journal*, *909*(2), 101. doi: 10.3847/1538-4357/abde3e

Israel, G. L., Esposito, P., Rea, N., Coti Zelati, F., Tiengo, A., Campana, S., … Pons, J. (2016, April). The discovery, monitoring and environment of SGR J1935+2154. *Monthly Notices of the Royal Astronomical Society*, *457*(4), 3448-3456. doi: 10.1093/mnras/stw008

Israel, G. L., Romano, P., Mangano, V., Dall'Osso, S., Chincarini, G., Stella, L., … Krimm, H. A. (2008, October). A Swift Gaze into the 2006 March 29 Burst Forest of SGR 1900+14. *Astrophysical Journal*, *685*(2), 1114-1128. doi: 10.1086/590486

Jones, P. B. (2003, September). Nature of Fault Planes in Solid Neutron Star Matter. *Astrophysical Journal*, *595*(1), 342-345. doi: 10.1086/377351

Kaastra, J. S. (2017, September). On the use of C-stat in testing models for X-ray spectra. *Astronomy and Astrophysics*, *605*, A51. doi: 10.1051/0004-6361/201629319

Kaneko, Y., Göğüş, E., Baring, M. G., Kouveliotou, C., Lin, L., Roberts, O. J., … Çoban, Ö. F. (2021, July). Fermi/GBM Observations of the SGRJ1935+2154 Burst Forest. *Astrophysical Journal, Letters*, *916*(1), L7. doi: 10.3847/2041-8213/ac0fe7

Kaneko, Y., Göğüş, E., Kouveliotou, C., Granot, J., Ramirez-Ruiz, E., van der Horst, A. J., … Woods, P. M. (2010, February). Magnetar Twists: Fermi/Gamma-Ray Burst Monitor Detection of SGR J1550-5418. *Astrophysical Journal*, *710*(2), 1335-1342. doi: 10.1088/0004-637X/710/2/1335

Kaspi, V. M., & Beloborodov, A. M. (2017, August). Magnetars. *Annual Review of Astron and Astrophysis*, *55*(1), 261-301. doi: 10.1146/annurev-astro-081915-023329

Kass, R. E., & Raftery, A. E. (1995). Bayes factors. *Journal of the American Statistical Association*, *90*(430), 773-795. Retrieved from `https://www.tandfonline.com/doi/abs/10.1080/01621459.1995.10476572` doi: 10.1080/01621459.1995.10476572

Keskin, Ö., Göğüş, E., Kaneko, Y., Demirer, M., Yamasaki, S., Baring, M. G., …

Kouveliotou, C. (2024, April). Concise Spectrotemporal Studies of Magnetar SGR J1935+2154 Bursts. *Astrophysical Journal*, *965*(2), 130. doi: 10.3847/1538-4357/ad2fce

Keskin, Ö., Lander, S. K., & Göğüş, E. (2025, May). Investigating the Recursive Short X-Ray Burst Behavior of Magnetars through Crustal Interactions. *Astrophysical Journal*, *985*(1), 45. doi: 10.3847/1538-4357/adc915

Kojima, Y., Kisaka, S., & Fujisawa, K. (2021, April). Evolution of magnetic deformation in neutron star crust. *Monthly Notices of the Royal Astronomical Society*, *502*(2), 2097-2104. doi: 10.1093/mnras/staa3489

Kouveliotou, C., Dieters, S., Strohmayer, T., van Paradijs, J., Fishman, G. J., Meegan, C. A., … Murakami, T. (1998, May). An X-ray pulsar with a superstrong magnetic field in the soft γ-ray repeater SGR1806 - 20. *Nature*, *393*(6682), 235-237. doi: 10.1038/30410

Kouveliotou, C., Strohmayer, T., Hurley, K., van Paradijs, J., Finger, M. H., Dieters, S., … Duncan, R. C. (1999, January). Discovery of a Magnetar Associated with the Soft Gamma Repeater SGR 1900+14. *Astrophysical Journal, Letters*, *510*(2), L115-L118. doi: 10.1086/311813

Kouveliotou, C., Tennant, A., Woods, P. M., Weisskopf, M. C., Hurley, K., Fender, R. P., … Göğüş, E. (2001, September). Multiwavelength Observations of the Soft Gamma Repeater SGR 1900+14 during Its 2001 April Activation. *Astrophysical Journal, Letters*, *558*(1), L47-L50. doi: 10.1086/323496

Kozlova, A. V., Israel, G. L., Svinkin, D. S., Frederiks, D. D., Pal'shin, V. D., Tsvetkova, A. E., … Zhang, X. L. (2016, August). The first observation of an intermediate flare from SGR 1935+2154. *Monthly Notices of the Royal Astronomical Society*, *460*(2), 2008-2014. doi: 10.1093/mnras/stw1109

Kuiper, L., Hermsen, W., & Mendez, M. (2004, October). Discovery of Hard Nonthermal Pulsed X-Ray Emission from the Anomalous X-Ray Pulsar 1E 1841-045. *Astrophysical Journal*, *613*, 1173-1178. doi: 10.1086/423129

Lander, S. K. (2016, June). Magnetar Field Evolution and Crustal Plasticity. *Astrophysical Journal, Letters*, *824*(2), L21. doi: 10.3847/2041-8205/824/2/L21

Lander, S. K. (2023, April). The Game of Life on a Magnetar Crust: From Gamma-Ray Flares to FRBs. *Astrophysical Journal, Letters*, *947*(1), L16. doi: 10.3847/2041-8213/acca1f

Lander, S. K., Andersson, N., Antonopoulou, D., & Watts, A. L. (2015, May). Magnetically driven crustquakes in neutron stars. *Monthly Notices of the Royal Astronomical Society*, *449*(2), 2047-2058. doi: 10.1093/mnras/stv432

Lander, S. K., & Gourgouliatos, K. N. (2019, July). Magnetic-field evolution in a plastically failing neutron-star crust. *Monthly Notices of the Royal Astronomical Society*, *486*(3), 4130-4143. doi: 10.1093/mnras/stz1042

Li, X., Levin, Y., & Beloborodov, A. M. (2016, December). Magnetar Outbursts from Avalanches of Hall Waves and Crustal Failures. *Astrophysical Journal*, *833*(2), 189. doi: 10.3847/1538-4357/833/2/189

Liddle, A. R. (2007, May). Information criteria for astrophysical model selection. *Monthly Notices of the Royal Astronomical Society*, *377*(1), L74-L78. doi: 10.1111/j.1745-3933.2007.00306.x

Lin, L., Göğüş, E., Roberts, O. J., Kouveliotou, C., Kaneko, Y., van der Horst, A. J., & Younes, G. (2020, April). Burst Properties of the Most Recurring

Transient Magnetar SGR J1935+2154. *Astrophysical Journal*, *893*(2), 156. doi: 10.3847/1538-4357/ab818f

Lin, L., Göğüș, E., Roberts, O. J., Baring, M. G., Kouveliotou, C., Kaneko, Y., . . . Younes, G. (2020, October). Fermi/GBM View of the 2019 and 2020 Burst Active Episodes of SGR J1935+2154. *Astrophysical Journal, Letters*, *902*(2), L43. doi: 10.3847/2041-8213/abbefe

Lin, L., Göğüş, E., Baring, M. G., Granot, J., Kouveliotou, C., Kaneko, Y., . . . Gehrels, N. (2012, September). Broadband Spectral Investigations of SGR J1550-5418 Bursts. *Astrophysical Journal*, *756*(1), 54. doi: 10.1088/0004-637X/756/1/54

Lin, L., Göğüş, E., Kaneko, Y., & Kouveliotou, C. (2013, December). Detailed Investigations of the Dimmest Bursts from Two Magnetars, SGR J0501+4516 and SGR J1550-5418. *Astrophysical Journal*, *778*(2), 105. doi: 10.1088/0004-637X/778/2/105

Lin, L., Kouveliotou, C., Baring, M. G., van der Horst, A. J., Guiriec, S., Woods, P. M., . . . Wilson-Hodge, C. (2011, October). Fermi/Gamma-Ray Burst Monitor Observations of SGR J0501+4516 Bursts. *Astrophysical Journal*, *739*(2), 87. doi: 10.1088/0004-637X/739/2/87

Lloyd, S. (1982). Least squares quantization in pcm. *IEEE Transactions on Information Theory*, *28*(2), 129–137. doi: 10.1109/tit.1982.1056489

Lyubarsky, Y. E. (2002). On the x-ray spectra of soft gamma repeaters. *Monthly Notices of the Royal Astronomical Society*, *332*(1), 199–204. doi: 10.1046/j.1365-8711.2002.05290.x

Lyutikov, M. (2003, December). Explosive reconnection in magnetars. *Monthly Notices of the Royal Astronomical Society*, *346*(2), 540-554. doi: 10.1046/j.1365-2966.2003.07110.x

MacFadyen, A. I., Woosley, S. E., & Heger, A. (2001, March). Supernovae, Jets, and Collapsars. *Astrophysical Journal*, *550*(1), 410-425. doi: 10.1086/319698

Manchester, R. N., Hobbs, G. B., Teoh, A., & Hobbs, M. (2005, April). The Australia Telescope National Facility Pulsar Catalogue. *Astronomical Journal*, *129*(4), 1993-2006. doi: 10.1086/428488

Meegan, C., Lichti, G., Bhat, P. N., Bissaldi, E., Briggs, M. S., Connaughton, V., . . . Wilson-Hodge, C. (2009, September). The Fermi Gamma-ray Burst Monitor. *Astrophysical Journal*, *702*(1), 791-804. doi: 10.1088/0004-637X/702/1/791

Mereghetti, S., Savchenko, V., Ferrigno, C., Götz, D., Rigoselli, M., Tiengo, A., . . . Ubertini, P. (2020, August). INTEGRAL Discovery of a Burst with Associated Radio Emission from the Magnetar SGR 1935+2154. *Astrophysical Journal, Letters*, *898*(2), L29. doi: 10.3847/2041-8213/aba2cf

Olausen, S. A., & Kaspi, V. M. (2014, May). The McGill Magnetar Catalog. *Astrophysical Journal, Supplement*, *212*(1), 6. doi: 10.1088/0067-0049/212/1/6

Palmer, D. M., Barthelmy, S., Gehrels, N., Kippen, R. M., Cayton, T., Kouveliotou, C., . . . Tueller, J. (2005, April). A giant γ-ray flare from the magnetar SGR 1806 - 20. *Nature*, *434*(7037), 1107-1109. doi: 10.1038/nature03525

Pedregosa, F., Varoquaux, G., Gramfort, A., Michel, V., Thirion, B., Grisel, O., . . . Édouard Duchesnay (2011). Scikit-learn: Machine learning in python. *Journal of Machine Learning Research*, *12*(85), 2825-2830. Retrieved from `http://jmlr.org/papers/v12/pedregosa11a.html`

Perna, R., & Pons, J. A. (2011, February). A Unified Model of the Magnetar and Radio Pulsar Bursting Phenomenology. *Astrophysical Journal, Letters*, *727*(2), L51. doi: 10.1088/2041-8205/727/2/L51

Petroff, E., Hessels, J. W. T., & Lorimer, D. R. (2019, May). Fast radio bursts. *Astronomy and Astrophysics Reviews*, *27*(1), 4. doi: 10.1007/s00159-019-0116-6

Petroff, E., Hessels, J. W. T., & Lorimer, D. R. (2021, July). Fast radio bursts at the dawn of the 2020s. *arXiv e-prints*, arXiv:2107.10113.

Pons, J. A., & Viganò, D. (2019, December). Magnetic, thermal and rotational evolution of isolated neutron stars. *Living Reviews in Computational Astrophysics*, *5*(1), 3. doi: 10.1007/s41115-019-0006-7

Scargle, J. D., Norris, J. P., Jackson, B., & Chiang, J. (2013, February). Studies in Astronomical Time Series Analysis. VI. Bayesian Block Representations. *Astrophysical Journal*, *764*(2), 167. doi: 10.1088/0004-637X/764/2/167

Schwarz, G. (1978, mar). Estimating the dimension of a model. *The Annals of Statistics*, *6*(2), 461-464.

Strohmayer, T. E., Zhang, W., Swank, J. H., White, N. E., & Lapidus, I. (1998, May). On the Amplitude of Burst Oscillations in 4U 1636-54: Evidence for Nuclear-powered Pulsars. *Astrophysical Journal, Letters*, *498*(2), L135-L139. doi: 10.1086/311322

Thompson, C., & Duncan, R. C. (1995, July). The soft gamma repeaters as very strongly magnetized neutron stars - I. Radiative mechanism for outbursts. *Monthly Notices of the Royal Astronomical Society*, *275*(2), 255-300. doi: 10.1093/mnras/275.2.255

Thompson, C., & Duncan, R. C. (1996, December). The Soft Gamma Repeaters as Very Strongly Magnetized Neutron Stars. II. Quiescent Neutrino, X-Ray, and Alfven Wave Emission. *Astrophysical Journal*, *473*, 322. doi: 10.1086/178147

Thompson, C., & Duncan, R. C. (2001, November). The Giant Flare of 1998 August 27 from SGR 1900+14. II. Radiative Mechanism and Physical Constraints on the Source. *Astrophysical Journal*, *561*(2), 980-1005. doi: 10.1086/323256

Thompson, C., Yang, H., & Ortiz, N. (2017, May). Global Crustal Dynamics of Magnetars in Relation to Their Bright X-Ray Outbursts. *Astrophysical Journal*, *841*(1), 54. doi: 10.3847/1538-4357/aa6c30

Thompson, T. A., Chang, P., & Quataert, E. (2004, August). Magnetar Spin-Down, Hyperenergetic Supernovae, and Gamma-Ray Bursts. *Astrophysical Journal*, *611*(1), 380-393. doi: 10.1086/421969

Tiengo, A., Vianello, G., Esposito, P., Mereghetti, S., Giuliani, A., Costantini, E., … Gehrels, N. (2010, February). The Dust-scattering X-ray Rings of the Anomalous X-ray Pulsar 1E 1547.0-5408. *Astrophysical Journal*, *710*(1), 227-235. doi: 10.1088/0004-637X/710/1/227

van der Horst, A. J., Kouveliotou, C., Gorgone, N. M., Kaneko, Y., Baring, M. G., Guiriec, S., … Wijers, R. A. M. J. (2012, April). SGR J1550-5418 Bursts Detected with the Fermi Gamma-Ray Burst Monitor during its Most Prolific Activity. *Astrophysical Journal*, *749*(2), 122. doi: 10.1088/0004-637X/749/2/122

Wadiasingh, Z., Baring, M. G., Gonthier, P. L., & Harding, A. K. (2018, Feb). Resonant Inverse Compton Scattering Spectra from Highly Magnetized Neutron Stars. *Astrophysical Journal*, *854*(2), 98. doi: 10.3847/1538-4357/aaa460

Wood, T. S., & Hollerbach, R. (2015, May). Three Dimensional Simulation of the Magnetic Stress in a Neutron Star Crust. *Physical Review Letters*, *114*(19), 191101. doi: 10.1103/PhysRevLett.114.191101

Woosley, S., & Janka, T. (2005, December). The physics of core-collapse supernovae. *Nature Physics*, *1*(3), 147-154. doi: 10.1038/nphys172

Woosley, S. E. (1993, March). Gamma-Ray Bursts from Stellar Mass Accretion Disks around Black Holes. *Astrophysical Journal*, *405*, 273. doi: 10.1086/172359

Xu, Y., Reid, M. J., Zheng, X. W., & Menten, K. M. (2006, January). The Distance to the Perseus Spiral Arm in the Milky Way. *Science*, *311*(5757), 54-57. doi: 10.1126/science.1120914

Yakovlev, D. G., Kaminker, A. D., Gnedin, O. Y., & Haensel, P. (2001, November). Neutrino emission from neutron stars. *Phys. Rep.*, *354*(1-2), 1-155. doi: 10.1016/S0370-1573(00)00131-9

Yamasaki, S., & Gogus, E. (2024, January). *Mbb-rcs: Modified black body with resonant cyclotron scattering - a magnetar flare spectral model.* Zenodo. Retrieved from `https://doi.org/10.5281/zenodo.10485159` doi: 10.5281/zenodo.10485159

Yamasaki, S., Lyubarsky, Y., Granot, J., & Göğüş, E. (2020, October). Spectral modification of magnetar flares by resonant cyclotron scattering. *Monthly Notices of the Royal Astronomical Society*, *498*(1), 484-494. doi: 10.1093/mnras/staa2223

Younes, G., Kouveliotou, C., van der Horst, A. J., Baring, M. G., Granot, J., Watts, A. L., … Wijers, R. A. M. J. (2014, April). Time Resolved Spectroscopy of SGR J1550-5418 Bursts Detected with Fermi/Gamma-Ray Burst Monitor. *Astrophysical Journal*, *785*(1), 52. doi: 10.1088/0004-637X/785/1/52

Younes, G., Lander, S. K., Baring, M. G., Enoto, T., Kouveliotou, C., Wadiasingh, Z., … Strohmayer, T. E. (2022, January). Pulse Peak Migration during the Outburst Decay of the Magnetar SGR 1830-0645: Crustal Motion and Magnetospheric Untwisting. *Astrophysical Journal, Letters*, *924*(2), L27. doi: 10.3847/2041-8213/ac4700

APPENDIX A

A.1 Robustness Tests of the Simulation Results

We performed more simulations with different initial stress levels and cell rules to test whether we would always obtain a similar clustered bursting behavior of short bursts. During the 1000 yr evolution of a magnetar, our simulations recorded ∼12,500 bursts; in only 1000 of them did cells fail and enter a plastic phase alone (no plastic neighbor), while most have at least one plastic neighbor (simultaneous plastic phases). Therefore bursts are prone to occur successively. This accumulation of bursts seems clearer (with a narrower time window around the years 40, 80, and 150; see Figure 2.5) when the magnetar is young. This is due to a highly stressed crust at the beginning of the simulation: the τ values of the cells are between $0.9\tau_{el}$ and $1.1\tau_{el}$. If we randomly set the initial stress level between $0.7\tau_{el}$ and $1.1\tau_{el}$, the simulation results in a similar total number of bursts, cell interactions, and the number of successive failures compared to the original case. The difference is that we do not observe excessive burst accumulation when the magnetar is young (see the top panel of Figure A.1). As can be seen in the figure, we still observe burst clustering behavior; the only difference is that the number of bursts in a burst cluster when the magnetar is young ($t < 200$ yr) is similar to the burst clusters observed in later years. Therefore, burst clusters do not have energies above 10^{42} erg in the corresponding burst cluster energy versus duration relation in the left panel of Figure A.2. If we randomly set the initial τ values within an even larger range between $0.5\tau_{el}$ and $1.1\tau_{el}$, then the number of bursts decreases to ∼10,000, with fewer bursts observed when the magnetar is young compared to older age due to cells trying to reach their yield stress during their long Hall phases. Yet we still observe burst clusters (see the middle panels of Figures A.1 and A.2).

We also tried another cell rule as follows: If a cell has two or more (three or four) plastic neighbors, it fails above τ_{el}; if it has one plastic neighbor, it fails at a τ value of $1.05\tau_{el}$; otherwise, it fails at $\tau = 1.1\tau_{el}$. This is effectively a slightly less nuanced version of the rule from Lander (2023). In this case, the number of bursts is still ∼12,500, but the number of interactions is decreased; the number of cells entering a plastic phase alone (without a plastic neighbor) is doubled. Again, we still observe burst clustering behavior, albeit less obvious in this case (see the bottom panel of Figure A.1). The right panel of Figure A.2 represents the corresponding cluster energy versus duration obtained with this cell rule.

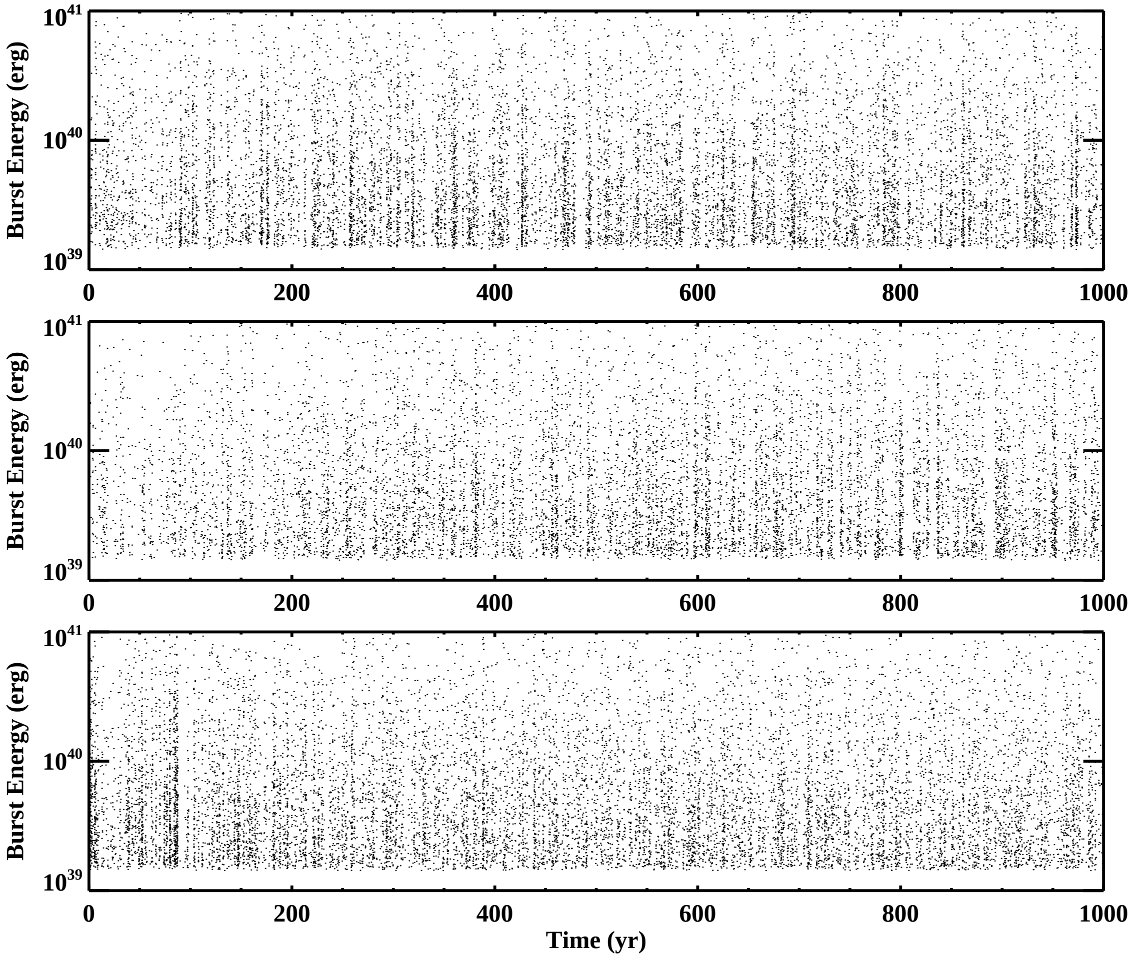

Figure A.1 The burst energies over a 1000 yr obtained with [**Top**] random initial stress values between $0.7\tau_{el}$ and $1.1\tau_{el}$. [**Middle**] random initial stress values between $0.5\tau_{el}$ and $1.1\tau_{el}$. [**Bottom**] another cell rule (see text for details).

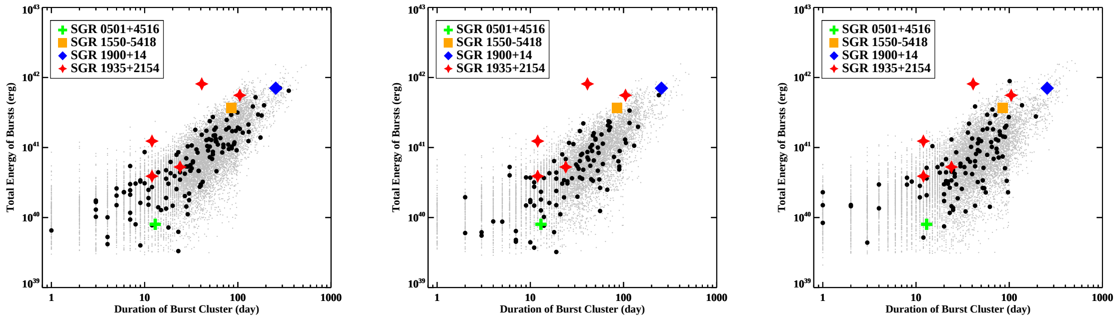

Figure A.2 The total burst energy vs. duration of each burst cluster from 100 simulations through 1000 yr evolution (gray dots). The black circles show the results of a single simulation (the ones shown in Figure A.1). Colored data points represent the same relation for the actual observations of magnetars. [**Left**] Initial stress level: $0.7\tau_{el}$ - $1.1\tau_{el}$. [**Middle**] Initial stress level: $0.5\tau_{el}$ - $1.1\tau_{el}$. [**Right**] Another cell rule (see text for details).

APPENDIX B

B.1 Spectral Data Extraction

For each event, we calculated the burst duration (i.e., the duration over which burst spectral extraction is to be performed) using the data collected with the brightest NaI detector, which is the detector with the smallest zenith angle to the sky position of the source. In particular, we first constructed a light curve with 4 ms time resolution for the time interval of −10 s to 10 s with respect to the burst start time published in Lin, Göğüş, et al. (2020); Lin, Göğüș, et al. (2020), using time-tagged photon data in the 8−200 keV energy band. We then generated the Bayesian Block representation of the light curve. Blocks longer than 4 s were considered background blocks, and the background level was calculated by averaging the count rates of these background blocks. The blocks shorter than 4 s and with higher rates than the background level are taken as burst blocks, and the duration is calculated as the time interval from the start of the first burst block to the end of the last one (Lin, Göğüş, Kaneko, & Kouveliotou, 2013).

To define the sequentially overlapping time segments of each burst, we first determined the background level as the average of the pre-burst time interval between −50 s and −1 s by taking the start time of Bayesian Block duration as the reference point. Then, we obtained a background-subtracted light curve with 4 ms time resolution in the energy range of 8−200 keV and determined the beginning and end points of time segments for the spectral data extraction, each of which contains at least 1200 background-subtracted counts and overlaps 80% in time with the previous one. As stated in Section 3.1, in the case of accumulation of time segments at the peak of a burst, we reduced the overlap by increments of 5%, until the endpoint of the subsequent time segment ended later than the end of the previous one.

We aim to investigate each burst by dividing it into as many short time intervals as possible. At the same time, we also aim for these intervals to have sufficient statistics (i.e., burst counts) for reliable spectral analysis. Therefore, setting a threshold background-subtracted counts to be included in each time segment is required. To this end, we selected a small set of bursts and extracted spectra of the time segments for each of these bursts, again with 80% overlap, but with a set of different numbers of background-subtracted counts, namely 600, 800, 1000, 1200, 1500, 1800, and 2000. We then fit these spectra with the three models that we used in this study and checked whether the resulting model parameters are constrained within at least a 2σ level. Based on this analysis, we concluded that a threshold of 1200 background-subtracted counts was needed to ensure reliable spectral analysis results with constrained model parameters for each time segment. With this requirement of 1200 burst counts in each time segment, the minimum number of counts throughout a burst should be larger than about 2400 in order for a burst to consist of at least two non-overlapping time segments, therefore, spectral evolution could be defined.

We also checked the potential count saturation in the data, from which very bright bursts may suffer. The GBM TTE data are affected by 2.6 μs deadtime as a result of the fixed data-packet processing speed of 375 kHz on the spacecraft (Meegan et al., 2009). Therefore, when the combined count rates of all GBM detectors surpass this limit, data saturation occurs. We did not find saturation in the data during any of the 51 bursts in our chosen sample.

B.2 Machine-learning Approach for Spectral Clustering

K-means clustering is a commonly used algorithm in data analysis that groups data points based on specific features, which in our case are the midpoints of time segments and corresponding E_{peak} values for each burst. Its primary objective is to cluster data points in a way that maximizes the similarity within clusters and minimizes the similarity between different clusters (Lloyd, 1982).

In this study, Python programming language (version 3.6.9) and Scikit-learn (version 1.2.1) were used for k-means clustering. The algorithm requires a predetermined number of clusters (k). Firstly, it initializes centroids by randomly selecting k samples from the data set. After initialization, the algorithm iterates between the remaining two steps: It first assigns each sample to the nearest centroid, then it creates new centroids by computing the mean value of all the samples assigned to each of the previous centroids. The algorithm repeats these last two steps until the squared difference between the old and new centroids is less than a predefined threshold, indicating that the centroids have become stable, and the clustering is complete.

For each burst, first, the data was scaled to prevent the effect of one variable from overriding the other because the ranges of time and E_{peak} axes vary significantly. Next, the k-means algorithm was implemented for all possible k values, ranging from one to $(N-1)$, where N is the number of time segments, and the corresponding inertia (i.e., the sum of the squared distances of the samples to their closest cluster center) for each k was recorded. Note that the reciprocal of E_{peak} errors was given as a weight for the inertia calculation. By the definition of inertia, its value decreases as the number of clusters (k) increases. However, increasing k does not significantly reduce inertia after a certain number of k, and the inertia versus k graph becomes flat after this point, encompassing a minimum of about $20-25\%$ of the high-k values in our sample. After studying a sample of events, we found that this point corresponds to the optimal number of clusters for finding the largest spectral variations during each burst. Therefore, instead of heuristic techniques that are commonly used to find the optimal k in k-means clustering, e.g., the "elbow" method, we developed our method as follows: First, we calculated the average of inertia values that corresponds to the highest 25% of the k values in the inertia versus k graph. We then added 1% of the maximum inertia value to the average inertia of the highest 25% of the k values. The nearest integer k value corresponding to the resulting inertia is then used for the optimal number of clusters.

Finally, we note that, in addition to k-means clustering, we also tested other machine-learning-based clustering algorithms; namely, density-based spatial clustering, agglomerative clustering, and Gaussian mixture model. They all require a number of clusters to be specified, and their results are consistent with those of k-means. Therefore, we consider k-means a robust method for our purpose.

B.3 Continuum Model Comparisons

To demonstrate how different photon models represent observed burst spectra, we present in Figure B.1 the spectrum extracted from a time segment of the burst that occurred at 488642074.718 (*Fermi* MET; 160626 13:54:30.722 UTC). All three models employed in this investigation yield equally good fits to this particular segment of burst data in our energy passband: MBB-RCS with kT of 9.46 keV (red curve in Figure B.1), COMPT with $\Gamma = 0.56$ and $E_{\rm peak} = 39.07$ keV (blue curve), and BB+BB with $kT_{\rm Low} = 7.4$ and $kT_{\rm High} = 15.31$ keV (green curve). Slight differences among the models are observed at the low-energy end and at the high-energy end, which are statistically indistinguishable.

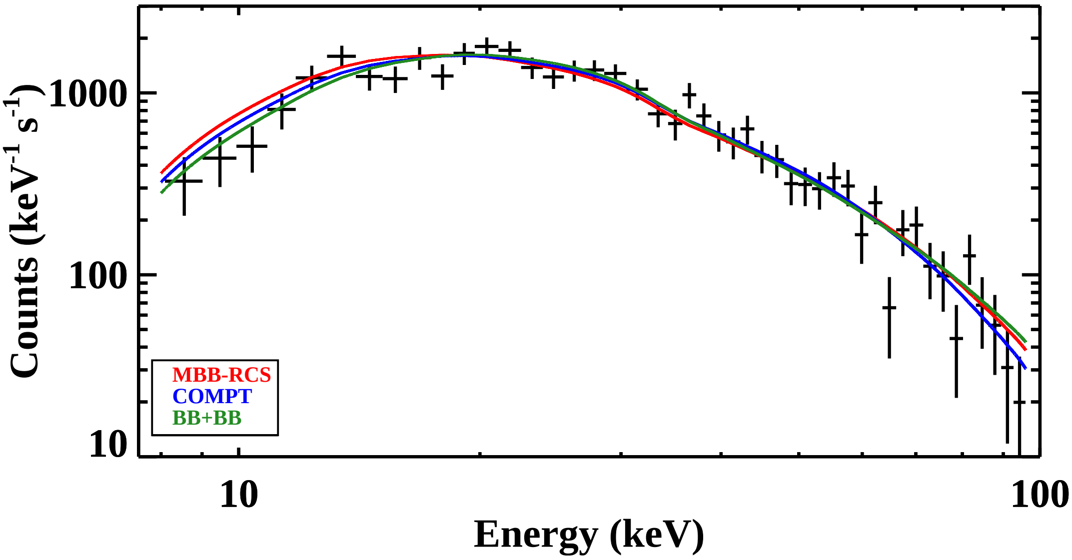

Figure B.1 Observed count spectrum of a time segment from the burst detected at 488642074.718 (*Fermi* MET), represented by black crosses. The three solid lines are the best-fitting model curves: MBB-RCS in red, COMPT in blue, and BB+BB in green, all of which fit the spectrum equally well.

We also present the evolution of spectral parameters of another example burst detected at 652927551.870 (*Fermi* MET; the same event also shown in Figures 3.2 and 3.3) in Figure B.2. This is an example event, throughout which a thermal model is preferred. In the left panel, we present the kT parameters of the thermal models (i.e., BB+BB and MBB-RCS) for the first 7 time segments. In the right panel, we present the evolution of photon flux distribution with time (from yellow to red) using the BB+BB model for segments 2 through 7. Note that both COMPT and MBB-RCS model curves are displayed for the first time segment. Since photon flux distributions of segments 2−7 are similar at high energies (above 60 keV), we zoomed in on the energy range of $8 - 60$ keV to clearly exhibit model differences at low energies.

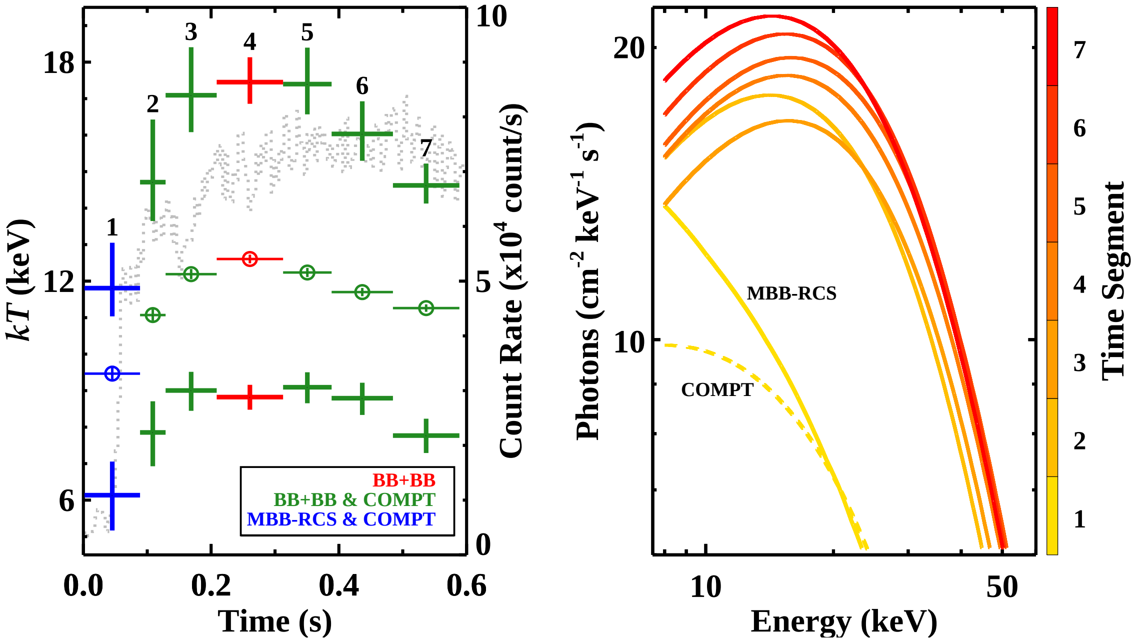

Figure B.2 **[Left]** Blackbody temperature evolution of the burst detected at 652927551.870 (*Fermi* MET; same event as Figures 3.2 and 3.3); this is the same plot as Figure 3.3 but zoomed in on the first 0.6 s. The first seven time segments are numbered on top, and thick crosses show the kT_{Low} and kT_{High} parameters of BB+BB, while thin data points with circles show kT_{M} of MBB-RCS. The color code represents the preferred model(s). **[Right]** The photon flux distribution for each time segment is shown. The color code represents the time segments. For the first time segment, the photon flux distributions shown with the yellow dashed line and yellow solid line were obtained with COMPT ($E_{\mathrm{peak}} = 37.85\,\mathrm{keV}$ and $\Gamma = 0.54$) and MBB-RCS, respectively. For the rest of the time segments, photon flux was obtained with BB+BB.